PB82-102435

# Impact of Topographic Circulations on the Transport and Dispersion of Air Pollutants

Virginia Univ.
Charlottesville

Prepared for

Environmental Sciences Research Lab.
Research Triangle Park, NC

Aug 81

U.S. Department of Commerce
National Technical Information Service
NTIS

PB82-102435

EPA-600/4-81-068
August 1981

# IMPACT OF TOPOGRAPHIC CIRCULATIONS ON THE TRANSPORT AND DISPERSION OF AIR POLLUTANTS

by

Roger A. Pielke and Richard T. McNider
Department of Environmental Sciences
University of Virginia
Charlottesville, Virginia 22903

Grant No. R806207

Project Officer

George C. Holzworth
Meteorology and Assessment Division
Environmental Sciences Research Laboratory
Research Triangle Park, North Carolina 27711

ENVIRONMENTAL SCIENCES RESEARCH LABORATORY
OFFICE OF RESEARCH AND DEVELOPMENT
U.S. ENVIRONMENTAL PROTECTION AGENCY
RESEARCH TRIANGLE PARK, NORTH CAROLINA 27711

REPRODUCED BY
NATIONAL TECHNICAL
INFORMATION SERVICE
U.S. DEPARTMENT OF COMMERCE
SPRINGFIELD, VA 22161

## TECHNICAL REPORT DATA
*(Please read Instructions on the reverse before completing)*

**1. REPORT NO.**
EPA-600/4-81-068

**2.**

**3. RECIPIENT'S ACCESSION NO.**
PB82 102435

**4. TITLE AND SUBTITLE**
IMPACT OF TOPOGRAPHIC CIRCULATIONS ON THE TRANSPORT AND DISPERSION OF AIR POLLUTANTS

**5. REPORT DATE**
August 1981

**6. PERFORMING ORGANIZATION CODE**

**7. AUTHOR(S)**
Roger A. Pielke and Richard T. McNider

**8. PERFORMING ORGANIZATION REPORT NO.**

**9. PERFORMING ORGANIZATION NAME AND ADDRESS**
University of Virginia
Charlottesville, Virginia 22903

**10. PROGRAM ELEMENT NO.**
CDTA1D/05-0263 (FY-81)

**11. CONTRACT/GRANT NO.**
R806207

**12. SPONSORING AGENCY NAME AND ADDRESS**
Environmental Sciences Research Laboratory - RTP, NC
Office of Research and Development
U.S. Environmental Protection Agency
Research Triangle Park, North Carolina 27711

**13. TYPE OF REPORT AND PERIOD COVERED**
Final 10/78-4/81

**14. SPONSORING AGENCY CODE**
EPA/600/09

**15. SUPPLEMENTARY NOTES**

**16. ABSTRACT**

A numerical mesoscale model is utilized to examine slope flows and the classic mountain-plain circulation for idealized topography. Special emphasis is given to turbulent parameterization in the stable boundary layer and the unique characteristics of turbulent mixing in the slope flows. The numerical simulations for idealized valley-plain configurations produced results consistent with observations such as shallow sidewall flows, the pooling of cool air in the valley, and a deep mountain flow out of the valley. A Lagrangian particle model, operating in the terrain following coordinate system of the mesoscale model, was developed to examine pollutant transport in the modeled circulations while a Markov statistical process was used to evaluate turbulent dispersion. Higher order turbulence parameters needed for the statistical model were directly computed from the numerical model. Results of dispersion tests in the modeled slope flows showed enhanced vertical dispersion in the slope flows compared to flow over a flat boundary, and, importantly, that normal surface scaling parameters for pollutant dispersion such as friction velocity were inappropriate for the slope flows.

**17. KEY WORDS AND DOCUMENT ANALYSIS**

| a. DESCRIPTORS | b. IDENTIFIERS/OPEN ENDED TERMS | c. COSATI Field/Group |
|---|---|---|
| | | |

**18. DISTRIBUTION STATEMENT**
RELEASE TO PUBLIC

**19. SECURITY CLASS** *(This Report)*
UNCLASSIFIED

**20. SECURITY CLASS** *(This page)*
UNCLASSIFIED

**21. NO. OF PAGES**
227

**22. PRICE**

EPA Form 2220-1 (9-73)

## DISCLAIMER

This report has been reviewed by the Environmental Sciences Research Laboratory, U.S. Environmental Protection Agency, and approved for publication. Approval does not signify that the contents necessarily reflect the views and policies of the U.S. Environmental Protection Agency, nor does mention of trade names or commercial products constitute endorsement or recommendation for use.

## TECHNICAL REVIEW

This research report was accepted as a Ph D thesis and thus has been technically reviewed by academic peers.

# ABSTRACT

A numerical mesoscale model is utilized to examine slope flows and the classic mountain-plain circulation described by early investigators. Special emphasis is given to turbulent parameterization in the stable boundary layer and the unique characteristics of turbulent mixing in the slope flows. Tests of the first order turbulent parameterization used in the numerical model verified against data from the Wangara experiment showed a simpler parameterization can simulate the mean boundary layer structure as well as more complex higher order schemes. Additional tests for the Great Plains indicated terrain and boundary layer processes are sufficient to reproduce the strong low level jets observed in the area.

Simplified subsets of the equations for uniform slopes were solved analytically to elucidate the role of stratification in reducing slope flow strength and to examine oscillatory behavior of the slope flows. The numerical simulations for idealized valley-plain configurations produced results consistent with observations such as shallow sidewall flows, the pooling of cool air in the valley, and a deep mountain flow out of the valley.

A Lagrangian particle model, operating in the terrain following coordinate system of the mesoscale model, was developed to examine pollutant transport in the modeled circulations. To evaluate turbulent dispersion, a Markov statistical process dependent upon higher order turbulence parameters was used. Higher order turbulence parameters needed for the statistical model were directly computed from the numerical model. Results of dispersion tests in the modeled slope flows showed enhanced vertical dispersion in the slope flows compared to flow over a flat boundary and, importantly, that normal surface scaling parameters for pollutant dispersion such as friction velocity were inappropriate for the slope flows.

# TABLE OF CONTENTS

ABSTRACT........................................................ iii

LIST OF ILLUSTRATIONS........................................... xii

ACKNOWLEDGEMENTS................................................ xiv

CHAPTER

I. INTRODUCTION................................................ 1

II. MESOSCALE MODEL DESCRIPTION................................ 6

Numerical Aspects.............................................. 8

Boundary Conditions............................................ 8

III. BOUNDARY LAYER AND RADIATIVE FORMULATION.................. 10

Turbulent Parameterization..................................... 11

Radiative and Surface Forcing.................................. 16

Simulation of an Idealized Nocturnal Boundary Layer...... 21

Simulation of Wangara Days 33-34............................... 24

Simulation of the Sloping Terrain of the Great Plains.... 47

Summary of Boundary Layer Formulations......................... 79

IV. HISTORICAL OVERVIEW OF MOUNTAIN-VALLEY CIRCULATIONS......... 84

Descriptive Models............................................. 84

Analytical Models.............................................. 85

Numerical Models............................................... 86

Laboratory Models.............................................. 87

Field Observations............................................. 88

V. SIMPLE SLOPE FLOWS.......................................... 90

Simplified Analytical Framework................................ 90

Analytical Solution Neglecting Friction........................ 93

**Preceding page blank**

TABLE OF CONTENTS (CONT'D)

Analytical Solution Including Friction.................. 96

Comparison of Analytical Solution with Mesoscale Model Solution........................................ 99

VI. NUMERICAL TWO DIMENSIONAL SLOPE FLOWS........................ 109

Sidewall Slope Flows.................................... 109

Valley Inversion........................................ 113

Time Dependence of the Slope Flows...................... 118

Turbulent Structure..................................... 125

Surges in the Downslope Flow............................ 128

VII. NUMERICAL THREE-DIMENSIONAL SLOPE AND MOUNTAIN FLOWS......... 130

Case Study A............................................ 130

Case Study B............................................ 135

VIII. POLLUTANT TRANSPORT........................................ 151

IX. POLLUTANT DISPERSION....................................... 158

Statistical Model....................................... 159

Higher Order Turbulent Statistics....................... 161

Dispersion Tests........................................ 173

X. TRANSPORT AND DISPERSION IN THE MODELED SLOPE AND MOUNTAIN FLOWS.............................................. 182

Streaklines and Trajectories............................ 182

Turbulent Dispersion.................................... 182

XI. SUMMARY AND CONCLUSIONS..................................... 199

BIBLIOGRAPHY................................................... 202

## LIST OF FIGURES

Figure III-1 Radiative warming rates using Wangara Day 34 0300 LST temperature and humidity sounding. Dashed line is based on the complete calculation of equation III-7. Solid line is based on the isothermal approximation of equation III-6.

Figure III-2 Profiles of exchange coefficients from the current model (X) for the idealized nocturnal boundary layer compared to those produced by more complex models for equivalent stability given by $|u_* / fL| = 65$. (from Rao and Snodgrass, 1979.)

Figure III-3 Time plot of model predicted surface and screen level temperatures compared with observed screen temperatures and Deardorff's diagnosed surface temperatures for Wangara Day 33-34.

Figure III-4 Profiles of model predicted exchange coefficient, $K_H$, during the evolution of the boundary layer for Wangara Day 33-34.

Figure III-5 Model predicted and observed u and v components along with geostrophic components used in the simulation for 1200 LST Day 33 Wangara experiment.

Figure III-6 Same as 5. except for 2100 LST Day 33.

Figure III-7 Same as 5. except for 0300 LST Day 34.

Figure III-8 Profile of model predicted Richardson Number for 0300 LST Day 34. For comparison the critical Richardson Number from equation (3) is plotted.

Figure III-9 Model predicted atmospheric temperature and soil temperature profiles for Day 33-34. (For clarity the soil temperature for 1800 LST is not shown.)

Figure III-10 Profiles of the partitioning of the turbulent and radiative contributions to local warming for 1200 LST, 2100 LST, and 0300 LST Day 33-34. Warming rates are one-hour averaged rates ending at the specified hour.

Figure III-11 Time plot of model predicted local warming rate (radiative and turbulent) and temperature at 5 meters above ground.

Figure III-12 Contours of northerly (v) velocity component over sloping terrain as reported by Hoecker (1963) from a special pibal network between Amarillo, Texas, and Little Rock, Arkansas. Contour interval is 5 m/s.

Figure III-13 Terrain configuration used in the model and the specified initial potential temperature field for Case 1. Contour interval is $1^{\circ}$K.

Figure III-14 Composite V-component (solid) and potential temperature (dashed) contours at 1500 LST showing the development of the convective boundary layer and baroclinic zone over the sloping terrain for Case 1. Contour intervals are 1 m/s and $1^{\circ}$K.

Figure III-15 Profiles of model predicted u and v components at 0930 LST along with profiles of the total geostrophic component $V_{gt}$ over the center of the sloping terrain for Case 1.

Figure III-16 Same as Figure III-15 except for 1530 LST. (Case 1)

Figure III-17 Same as Figure III-15 except for 2330 LST. (Case 1)

Figure III-18 Time variation of actual vector velocity at 300 m and surface geostrophic vector velocity for Case 1. Times are given to the side of the velocities.

Figure III-19 Contours of (a) northerly (v) component and (b) potential temperature ($\theta$) over the sloping terrain at 2230 LST for Case 1. Contour intervals are 2 m/s and $1^{o}$K.

Figure III-20 Profiles of model predicted u and v components at 1530 LST along with profiles of the total geostrophic component $V_{gt}$ for Case 2 in which terrain slope is double that of Case 1.

Figure III-21 Same as Figure III-20 except for 2330 LST. (Case 2)

Figure III-22 Same as Figure III-20 except for 0330 LST. (Case 2)

Figure III-23 Profiles of model predicted u and v components at 1530 LST along with profiles of the total geostrophic component $V_{gt}$ for Case 3.

Figure III-24 Same as Figure 21 except for 0130 LST. (Case 3)

Figure V-1 Time series of downslope velocity component produced by the non-linear numerical model for three stratifications.

Figure V-2 Time series of downslope velocity component from the analytical solution (V-21) for three stratifications.

Figure V-3 Advective warming in degrees per hour for the $8^{o}$ km$^{-1}$ stratification from the solution given in Figure V-1.

Figure VI-1 Downslope component (solid line) and potential temperature (dashed) profiles over the western sidewall of the two-dimensional valley at 0230 LST.

Figure VI-2 Contours of potential temperature in the two-dimensional valley. a) Contours for 2030 LST, b) Contours for 0230 LST. Contour interval is $1^{o}$ K. Asterisk gives location for profiles and time series in Figures VI-1 and VI-4.

Figure VI-3 Profiles of potential temperature over the center of the two-dimensional valley for the indicated times.

Figure VI-4 Time series plot of a) downslope component at two meters (dashed) and 50 meters (solid) above the western side wall and b) V component above the middle of the valley floor. Velocities plotted are three minute averages.

Figure VI-5 Time series of local warming (solid) and advective warming (dashed) over the western side wall. Warming rates are three minute averages.

Figure VI-6 Schematic of the deformation of the potential temperature field due to downslope and return upslope flow and resulting destabilization. a) initial field, b) after deformation by slope flow.

Figure VI-7 Turbulent exchange coefficient (solid) over the western valley wall showing pronounced maximum near the top of the slope flow. This profile can be compared to the profile given in Figure III-2 over a flat boundary. The dashed line gives the local gradient Richardson Number showing the unstable layer aloft created by the deformation illustrated in Figure VI-6.

Figure VII-1 Three-dimensional perspective of the topographic configuration used in Case A. Ridge height is 2 km; valley width is 19 km. (Note that the vertical scale is exaggerated.)

Figure VII-2 a) Times series of u component at 2 meters and 50 meters over the middle of the western sidewall (x = 15, y = 23).
b) Times series of v component at 2 meters and 50 meters at the center of the valley (x = 18, y = 23).

| | |
|---|---|
| Figure VII-3 | a) Contours of potential temperature at 2330 LST (y = 23). Contour interval is $1^{\circ}$K. b) Contours of the mountain wind (v-component) for the same time and location for Case A. Contour interval is 1 m/s. |
| Figure VII-4 | Plan view of velocity field for Case A at 2330 LST. a) at $z^*$ level of 8 meters. b) at $z^*$ level of 100 meters. |
| Figure VII-5 | Three-dimensional perspective of the topographic configuration used in Case B. Ridge height is 1.25 km; valley width is 11 km. |
| Figure VII-6 | Plan view of velocity field for Case B at 2330 LST. a) at $z^*$ level of 8 meters. b) at $z^*$ level of 100 meters. |
| Figure VII-7 | a) Contours of potential temperature at 2330 LST (y = 23) for Case B. Contour interval is $1^{\circ}$K. b) Contours of mountain component (v-component) for the same time and location. Contour interval is 1 m/s. |
| Figure VII-8 | a) Time series of u-component at 2 meters and 50 meters over the middle of the east facing western sidewall (x = 15, y = 23). b) Time series of v-component at 2 meters and 50 meters at the center of the valley (y = 18, y = 23). |
| Figure VIII-1 | Particle streaklines at 1900 EST from 50 meter release heights. (A) Plan view showing x - y distributions of particles. (B) Vertical view, looking northward, showing x - z distributions of particles. Particles were released at 10-minute intervals beginning at sunrise. |
| Figure VIII-2 | Same as Figure VIII-1 except for 300 meter release height. |
| Figure IX-1 | Plot of $A = K_m/\sigma_w\lambda_m$ as a function of Z/L as computed from standard formulas for $K_m$, $\sigma_w$ and $\lambda_m$ in the atmospheric surface layer. |

| | |
|---|---|
| Figure IX-2 | Plot of $\sigma_w/u^*$ extracted from the mesoscale model compared to the observational best fit by Panofsky et al. (1977). |
| Figure IX-3 | Plot of model extracted scaled $\sigma_w$ in the planetary boundary layer compared to observational composites and the numerical study by Deardorff (1974b). The dashed line was extracted from an unpublished study by F. B. Smith of the British Meteorological Service. ($w_*$ is the convective velocity scale given by $w_* = u_* (-h/kL)^{1/3}$ ) |
| Figure IX-4 | Plot of $\sigma_w/u^*$ in the stable boundary layer. (H is estimated height of the nocturnal boundary layer, defined as the height to which turbulence is evident.) |
| Figure IX-5 | Plot of root-mean-square vertical dispersion as predicted by the current conditioned particle scheme. See Willis and Deardorff (1978) for an explanation of the non-dimensional scaling. |
| Figure IX-6 | Same as figure IX-5 except for the lateral dispersion. |
| Figure X-1 | Time series of snapshots of streaklines for particles emitted into the mountain flow of Case A Chapter VII. Figures top to bottom give snapshots respectively at 1, 3, and 5 hours after sunset. Vertical depictions are on the left; horizontal depictions on the right. Terrain is not illustrated since it would mask the particle locations. |
| Figure X-2 | Trajectories of particles released an hour apart from a height of 2 meters. Final heights in kilometers are given to the side of the end of the trajectory. |
| Figure X-3 | Vertical dispersion for the three cases described in the text. Root-mean-square spread is scaled by the boundary layer height. 0 - Flat boundary no wind. ● - Slope case no wind. X - Slope case with wind. |

Figure X-4 Lateral (Y) dispersion for the three cases described in the text. 0 - Flat boundary no wind. ● - Slope case no wind. X - Slope case with wind.

Figure X-5 Along-the-wind (X) dispersion for the three cases described in the text. 0 - Flat boundary no wind. ● - Slope case no wind. X - Slope case with wind.

Figure X-6 Snapshots of particle spread over the sloping boundary with no wind. Each figure is 4 km in cross-section. Top figure gives dispersion 400 seconds after release; middle figure 800 seconds after release; bottom figure 2400 seconds after release.

Figure X-7 Snapshots of particle spread over the sloping boundary with wind. Figure 8 km is cross-section. Top figure gives dispersion after 200 seconds; middle figure after 600 seconds; bottom figure after 1000 seconds.

# ACKNOWLEDGEMENTS

I wish to thank Dr. Roger Pielke, my major advisor, for his help and support of this research. Dr. Pielke and the mesoscale modeling group at UVA provided the basic mesoscale model code without which this research would have been impractical. I especially appreciate the timely review of draft material by Dr. Pielke and the enthusiam he demonstrated for the research. My committee members, Drs. Joanne Simpson, Michael Garstang, Wallace Reed and John Scott are also thanked for their help in focusing this research and their guidance.

I also want to thank my friends and colleagues Bob Kessler, Mike McCumber, Moti Segal, Ken Anderson, Arthur Mizzi, Bill Snow and Charlie Martin for their many helpful discussions. I owe a special debt of appreciation to Mike McCumber who helped tremendously in orienting me to the mesoscale model code.

Dr. Steve Hanna was of immense help in directing me toward pertinent literature on turbulence observations and for his helpful discussions on particle dispersion. I also want to thank Dr. Robert Lamb for his conversations on skewed turbulent distributions.

Drs. Paul Long and Wilson Schaffer are thanked for their initial discussions of the low-level jet phenomena. I appreciate also Dr. Dave Emmitt's generosity in allowing me to borrow his extensive literature on the mountain-valley studies in South Africa.

Mrs. Darlene Gregory did an excellent job of typing the manuscript and her cheerfulness and dedication to its timely completion is appreciated. Mr. Don Moss is thanked for his help and suggestions in establishing computer telecommunications links. I owe special thanks to Mr. James Cooper, Director of the Alabama Air Pollution Control Commission, for

allowing me to pursue this research endeavor. I am also appreciative of the Planning and Development Section of the Commission for their patience and support.

Finally, I owe the greatest debt of gratitude to my wife, Martha and daughters, Amy and Sheri, for their understanding and support in this endeavor in spite of the disruption and inconvenience it caused in their own lives.

Direct support for this research was provided by the U.S. Environmental Protection Agency and the Alabama Air Pollution Control Commission. Computer time was supplied by the National Center for Atmospheric Research, which is supported by the National Science Foundation.

## I. INTRODUCTION

In recent years because of growing environmental concern and regulatory requirements, increased attention has been given to assessing and predicting the transport and dispersion of pollutants and radioactive material in the atmosphere. Presently available operational methods for predicting concentrations of material are primarily steady-state, analytical models based upon the dispersion of the material in a Gaussian manner. The basic assumptions behind the Gaussian models - a steady, uniform wind field - are clearly violated along sea coasts or in complex terrain where sea-breeze and mountain-valley circulations produce highly sheared flows and time-dependent recirculations. Also, because of the local circulations, the most fundamental variable for pollutant exposure predictions - wind direction - cannot be deduced from one or two observation points.

This lack of adequate models and transport description is critical, since many large urban areas, pollution sources and nuclear reactors are located or will locate in valleys and in coastal areas because of land suitability, water and transportation requirements. The importance of topographic circulations is further emphasized by the fact that such mountain-valley flows are most evident during the type synoptic conditions associated with air stagnation episodes, i.e. light synoptic winds and clear skies. Thus, during such stagnations the local mesoscale circulations provide the primary dilution and transport mechanism for pollutants within a valley.

In attempting to assess transport and dispersion in complex terrain, the first step is to understand and model the mountain-valley wind systems. In the 1930-1960 period considerable interest (at least as evidenced in the literature) was directed toward the observation and description of mountain-valley circulations. Recent air pollution concerns have revived interest in mountain-valley circulations, but in the intervening years little theoretical or observational work was undertaken except for some observational studies in South Africa (Tyson (1966)). The primary reason for this lull in activity is the fact that the descriptive studies in the early period (e.g. Wagner (1938), Defant (1951)) indicated that mountain-valley circulations are a non-linear, three-dimensional phenomenon with the along-the-valley-axis circulations[1] intimately related to the side-wall slope flows and dependent on radiative and turbulent exchange processes. Such complexity effectively precluded the application of the analytic mathematical tools available at the time. Only in recent years have computer capacity and numerical modeling techniques progressed to the point where full three-dimensional treatment of the problem is possible.

The investigation which follows has two major components: 1) the numerical study of three dimensional thermally driven mountain-valley flows and, 2) the examination of pollutant transport and dispersion in the mountain-valley flows.

## Mountain-Valley Circulations

In this investigation the University of Virginia Mesoscale model (UVMM) originally developed by Pielke (1974) is used to study thermally driven two-dimensional slope flows and three-dimensional mountain-valley circulations for idealized topography. Except for an incomplete[2] numerical study by Thyer (1962), a full investigation of three-dimensional mountain-valley circulations has not appeared in the literature.

---

[1] In this investigation, following Defant, _mountain_ wind refers to the along-the-valley axis component flowing out of the valley and _valley_ wind refers to flow up the valley.

[2] See Chapter IV for a description of Thyer's study.

The idealized topography used in the present study is constructed to examine the essential physics that led early investigators to their descriptive models of mountain-valley flows. For this reason the basic valley configurations have a high height-to-width ratio opening onto a flat plain. It should be emphasized that the purpose of this study is to compare the numerical model results and the physics producing these results to the physical concepts behind the descriptive models and not to simulate a single set of observations. It is felt that most available observations in valleys are either too sparse or in areas too complex to simulate without first examining the simple conceptual situations.

Since the turbulent transfer of heat and momentum is critical to the development of slope and mountain-valley circulations a detailed description of boundary layer and turbulent exchange processes are described in Chapter III. Particular emphasis is placed upon modeling the stable nocturnal boundary layer. The stable boundary layer is modeled using a scheme proposed by Blackadar (1979) in which turbulent exchange coefficients are dependent upon the local Richardson number and an imposed mixing length. The new boundary layer formulation is tested against field data from the Wangara and Great Plains field experiments.

Chapter IV provides an overview outlining the observed characteristics of slope and mountain flows and the historical development of models describing the flows. Observational studies of mountain winds have indicated pulses or surges in the winds. Although no definite mechanism has been established, Fleagle (1950), in an analytical study, attributed the surges to adiabatic warming of the downslope flow occurring faster than the radiative cooling, thus leading to alternating accelerations in the flow.

In Chapter V, these surges are examined using a simplified analytical model and the full numerical model. Chapters VI and VII describe the results of the numerical simulation of slope and mountain flows for idealized two and three-dimensional valleys and qualitatively compares these results to observations.

## Pollutant Transport and Diffusion

Modeling the transport and diffusion of pollutants, especially from point sources presents many theoretical as well as numerical problems. For short travel times, gradient transfer theory for diffusion is not generally applicable to point sources, since the scale of the turbulent eddies are large compared to the size of the plume being dispersed (Pasquill (1974)). Even for longer travel times when the plume exceeds the turbulent scale, the grid resolution generally available in a mesoscale model is not adequate to correctly define the concentration gradient. For example, under stable conditions and for a horizontal grid resolution of 4 km, a plume could travel up to 15-20 km before even being defined by two model grid points. Moreover, in representing pollutant advection the numerical damping of short wavelengths (inherent in the schemes) is disastrous, since the plumes and puffs are short wavelength phenomenon.

Chapters VIII and IX describe a Lagrangian particle scheme for assessing pollutant transport and dispersion which avoids the above mentioned problems. Transport is handled in a direct Lagrangian manner using the wind field produced by the mesoscale model, while turbulent dispersion is accomplished using a Markov statistical process (Hanna (1979)). The statistical model requires an estimate of higher order turbulent statistics which are extracted from the mesoscale model boundary layer.

The generality and flexibility of the Lagrangian particle scheme allows useful insight into the transport and dispersion in the complex flow fields of the mountain-valley circulations. Pollutant transport is shown to be highly dependent upon the release position within the flow field while the turbulence field produced in the highly sheared slope-mountain circulations dramatically affects the turbulent dispersion of material.

## II. MESOSCALE MODEL DESCRIPTION

The basic structure of the mesoscale model used in the present investigation was originally developed by Pielke (1974) for the study of South Floride sea breezes. At the University of Virginia additional improvements of the model have been made (e.g. Pielke and Mahrer (1975)), Mahrer and Pielke (1977), McCumber (1980)) and the model is denoted generically as the University of Virginia Mesoscale Model (UVMM).

The basic model equations for hydrostatic incompressible flow in terrain following coordinates as given by Mahrer and Pielke (1977) or McCumber (1980) are given below:

$$\frac{du}{dt} = fv - fV_g - \theta\frac{\partial\tilde{\pi}}{\partial x} + g\,\frac{z^* - \bar{s}}{\bar{s}}\,\frac{\partial z_G}{\partial x} - g\,\frac{z^*}{\bar{s}}\,\frac{\partial s}{\partial x} + \left(\frac{\bar{s}}{s - z_g}\right)^2 \frac{\partial}{\partial z^*}\,K_m\,\frac{\partial u}{\partial z^*} + \mathrm{Fil}\,(u)\ , \tag{II-1}$$

$$\frac{dv}{dt} = -\,fu + fU_g - \theta\frac{\partial\tilde{\pi}}{\partial y} + g\,\frac{z^* - \bar{s}}{\bar{s}}\,\frac{\partial z_G}{\partial y} - g\,\frac{z^*}{\bar{s}}\,\frac{\partial s}{\partial x} + \left(\frac{\bar{s}}{s - z_G}\right)^2 \frac{\partial}{\partial z^*}\,K_m\,\frac{\partial v}{\partial z^*} + \mathrm{Fil}\,(v)\ , \tag{II-2}$$

$$\frac{d\tilde{\theta}}{dt} = \left(\frac{\bar{s}}{s - z_G}\right)^2 \frac{\partial}{\partial z^*}\,K_h\,\frac{\partial\tilde{\theta}}{\partial z^*} + \mathrm{Fil}\,(\theta) + F_\theta\ , \tag{II-3}$$

$$\frac{dq}{dt} = \left(\frac{\bar{s}}{s - z_G}\right)^2 \frac{\partial}{\partial z^*}\,K_h\,\frac{\partial q}{\partial z^*} + \mathrm{Fil}\,(q) + F_q\ , \tag{II-4}$$

$$\frac{\partial}{\partial t}(s - z_G) + \frac{\partial}{\partial x}\,u(s - z_G) + \frac{\partial}{\partial y}\,v(s - z_G) + \frac{\partial}{\partial z^*}\,w^*(s - z_G) = 0, \tag{II-5}$$

$$\frac{\partial \tilde{\pi}}{\partial z^*} = - \frac{s - z_G}{\bar{s}} \frac{g}{\tilde{\theta}} , \qquad \text{II-6}$$

where

$$\tilde{\pi} = c_p \left( \frac{\tilde{p}}{p_{oo}} \right)^{R/c_p} ,$$

$$w^* = \frac{\bar{s}}{s - z_G} w - \frac{z^*}{s - z_G} \left( \frac{\partial s}{\partial t} + u \frac{\partial s}{\partial x} + v \frac{\partial s}{\partial y} \right) + \frac{z^* - s}{s - z_G} \left( u \frac{\partial z_G}{\partial x} + v \frac{\partial z_G}{\partial y} \right) ,$$

$$\frac{d}{dt} = \frac{\partial}{\partial t} + u \frac{\partial}{\partial x} + v \frac{\partial}{\partial y} + w^* \frac{\partial}{\partial z^*}$$

and Fil denotes a horizontal filter in place of horizontal diffusion with $Fq$ and $F\theta$ representing source/sink terms for $\theta$ and $q$ (e.g. radiational flux divergence). A derivation of the pressure terms in these equations is given in Appendix A.

For the nocturnal slope and mountain flows considered in this investigation a rigid top ($s = \bar{s}$) was imposed with fixed boundary conditions at the top. It is felt that this simple boundary condition with the top model level near the stratosphere is adequate for simulating shallow nocturnal drainage flows. Model tests in two-dimensions using both a fixed top and floating material surface at a height of 9 km produced virtually identical slope flow solutions.

As evident in II-1 through II-4 the model employs first order closure for the turbulent parameterization. Chapter III gives a detailed explanation of the procedures used to determine the turbulent exchange coefficients.

## Numerical Aspects

Aside from the use of the terrain following coordinate which allows inclusion of topography in a general manner, several unique numerical techniques are utilized in the model. Perhaps the most important is a quasi-Lagrangian spline technique for numerical evaluation of the non-linear advection terms. This technique, described by Mahrer and Pielke (1978), is highly accurate and reduces substantially the numerical damping associated with some numerical schemes and retains a highly accurate representation of phase speed. A second important technique is the use of an implicit numerical scheme (Paegle et al. (1976)) for evaluation of the vertical diffusion terms. This scheme is thought to be especially important for the use of the local exchange coefficients described in Chapter III. An implicit filter (Paul Long, personal communication; see Mahrer and Pielke (1978)) is used in place of explicit horizontal diffusion and has the advantage of selectively damping unwanted small wavelength features, thereby controlling aliasing.

A surface energy budget employing multiple soil layers (Mahrer and Pielke (1977)) is used to force the model. Surface turbulent fluxes are parameterized using the similarity formulas of Businger (1973).

## Lateral Boundary Conditions

Specification of proper boundary conditions is always difficult in limited scale modeling. First is the problem of spurious accelerations across the model domain due to erroneous differential specification of boundary values (Anthes and Warner (1978)). The second, which has received more attention, is wave reflection from the boundaries resulting in amplification and destruction of wave forms. Because of the low initial wind values which will be imposed in studying the valley flow problem and the fact that the thermally induced circulations will gradually spin up, the initial impulsive imbalance and resulting amplitude of the mass adjusting gravity waves and inertial oscillations should be relatively small. [Small in comparison to the size of initial imbalances expected in high speed forced flows over terrain.] For this reason it is felt that the first type boundary problem, where spurious domain accelerations could dominate the solution, is potentially the most serious problem in the correct simulation of the valley flows.

In the present investigation, zero gradient boundary conditions were utilized at all lateral boundaries. The model grid lattice was stretched near the boundary to remove the boundary as far as possible from the region of interest. In addition a buffer zone near the boundaries of at least 8 grid points of zero gradient topography was incorporated. Two-dimensional tests indicated interior solutions were not affected substantially by further expansion of the model domain.

These simple boundary conditions cannot of course adequately handle pronounced flow reversal at the boundaries nor completely remove the erroneous domain accelerations described above. It is felt, however, that they are adequate for this first attempt to model idealized valley situations.

## III. BOUNDARY LAYER AND RADIATIVE FORMULATION

Turbulent exchange processes are critical to the development of nocturnal drainage flows and mountain winds. Not only does turbulent transfer through surface drag and interfacial entrainment govern the speed and depth of the drainage flow; but, the turbulent transport of heat essentially defines the depth of the temperature perturbation which directly drives the drainage flow.

While stable boundary layer structure over flat land is complex in its own right; the turbulent structure and behavior is even more complicated in slope drainage flows. For example, in drainage flows, because the accelerations appear at the surface, the turbulent momentum transfer is upward in the shear zone between the slope flow and the ambient flow. This is contrary to the conventional downward transport over a flat stationary boundary. Also, as will be shown in Chapter VI, the complex downslope and return flows can produce thermal instabilities aloft causing convective instability even though the surface is stable.

Because turbulent mixing properties in drainage flows are not soley related to surface frictional or stability effects a turbulent parameterization based upon local conditions was chosen for use in the slope and mountain-wind model experiments. A description of the turbulent parameterization in the context of the present model structure is given in the next section. Since relatively little mesoscale modeling of the stable boundary layer has taken place, several model tests were made for comparison with higher order closure models and actual data. The tests include: (1) an idealized nocturnal boundary layer with constant cooling; (2) a detailed comparison of the models performance over flat land for a full diurnal cycle for Day 33-34 of the Wangara Experiment; and (3) an investigation of the model behavior over extensive sloping terrain for comparison with observations over the Great Plains of the U.S. In the latter test, particular attention is given to the development of a diurnal pressure gradient oscillation over the sloping terrain and development of nocturnal low-level jets in response to this oscillation. Also as part of the Wangara experiments, simplifications of the radiative transfer problem are examined for their application to the nocturnal boundary layer.

## Turbulent Parameterization

Turbulent exchange processes in the model for the growing convective boundary employ a cubic polynomial profile formulation specifying the turbulent exchange coefficients (O'Brien (1970)). Boundary conditions for the cubic polynomial are provided at the surface by the similarity functions proposed by Businger (1973) and at the top by a prognostic equation for the planetary boundary layer depth proposed by Deardorff (1974). Pielke and Mahrer (1975) previously showed that this simplified parameterization realistically simulated the growing convective boundary layer for Wangara Day 33.

In the present investigation, the model is generalized to represent the stable boundary layer using a local exchange coefficient scheme suggested by Blackadar (1979). Using second order closure as a guide to approximations, Blackadar suggested that model exchange coefficients for the stable boundary layer above the surface could be related to the local gradient Richardson Number, Ri, by a simple expression of the form

$$\begin{aligned} K_m = K_H &= 1.1(Ri_c - Ri)l^2 s/Ri_c & Ri &< Ri_c \\ &= 0 & Ri &> R_i \end{aligned} \qquad \text{III-1}$$

where $Ri_c$ is a critical Richardson Number, l is a mixing length, and s is the local shear. As suggested by Blackadar (1978), Brost and Wyngaard (1978), and Delage (1974), the mixing length under strong stabilities (except very near the surface) is not dependent upon height, and perhaps scales with the local Monin-Obukov length. In the present investigation, the mixing length is simply taken as a linear function of z near the surface and a constant of 70 meters (Blackadar (1979)) elsewhere, i.e.,

$$l = .35\,Z \qquad z < 205\text{m}$$

$$l = 70\text{m} \qquad z \geq 205\text{m}. \qquad \text{III-2}$$

Specification of a proper critical Richardson Number, $Ri_c$, in a coarse resolution model is difficult. Although theoretical considerations indicate a critical Richardson Number of near .25, observations (which have limitations due to contamination by turbulent transport and coarse observing arrays) only provide general guidelines on a bracket below which turbulence is likely to exist and above which turbulence is likely to be suppressed. Shir and Bornstien (1977) in a review discuss this problem in length. The review notes that some authors have concluded $Ri_c$ is itself a function of stability while others have pointed out that determination of $Ri_c$ is dependent on the resolution of the observations. In a mesoscale model, the model grid points only define grid volume averaged parameters and thus only reflect grid averaged accelerations. In reality, accelerations may occur on much finer scales leading to Richardson Number type instabilities and accompanying mixing which would not be resolved in a coarse grid model. For these reasons, we have chosen to make $Ri_c$ a weak function of the model grid spacing of the form

$$Ri_c = A \;\; \Delta Z^{\,B} \qquad \text{III-3}$$

where $\Delta Z$ is the model grid spacing in cm, and in the present study A = .115 and B = .175. The result of this functional relationship is that for the fine vertical grid resolution near the surface (from 2 to 20m) the critical

Richardson Number is near the theoretical value of .25 while away from the surface where the grid resolution is 500-1000m, $Ri_c$ approaches 1.0. This latter value is consistent with critical Richardson Numbers used to predict the onset of clear air turbulence based on standard rawinsonde observations.

The diffusion terms are evaluated numerically using a forward weighted scheme suggested by Paegle et al. (1976). It is felt that the excellent accuracy of this scheme makes it ideally suited to represent the local exchange coefficient formulation in which exchange coefficients can vary dramatically between adjacent grid points. In the numerical formulation, the Richardson Number and shear required by (III-1) are calculated at each vertical level in the model. Because of the staggered grid in the model in which thermodynamic variables are defined at intermediate grid points between the velocity grid points, a linear interpolation of temperature (or velocity) is required to define a centered differenced Richardson Number.

As stated earlier, different models (non-local as opposed to local exchange coefficients) are used to represent the convective and the stable boundary layers. Recent evidence (Kaimal et al., 1976) indicates that the turbulent eddies above the surface in the convective boundary layer have scales related to the planetary boundary layer height. Because these scales would be large compared to the model grid resolution, the turbulent exchange processes should not be expected to be entirely dependent upon local conditions. The profile formulation used in the model for this condition simply parameterizes this non-local state by relating the exchange coefficients to the surface heat flux and the PBL height. On the other hand, in the stable boundary layer, the scale of the turbulence is generally smaller than the grid resolution in the model and locally dependent exchange processes, such as suggested by Blackadar (1979) are more appropriate.

In the nocturnal boundary layer, when situations occur where the model grid resolution is smaller than the mixing length, the scheme is made partially non-local. For this case, the exchange coefficient at a point is found by averaging exchange coefficients at neighboring points using an inverse weighting scheme dependent upon the ratio of grid distance to mixing length. It is felt that this is physically realistic and allows, for example, some heat to be mixed through the nose of a narrow low level jet where the local Richardson Number is quite large. This technique partially addresses the criticisms Shir and Bornstien (1977) raised with the use of local exchange coefficients in regard to the proper evaluation of the Richardson Number near a narrow jet.

Because two different exchange coefficient models are used, a physically plausible transition must be made from the non-local to the local model. The transition criteria used in these simulations is related to the sign of the surface heat flux. When the surface flux changes from positive to negative, i.e., when the surface stabilizes, the switch is made from the non-local to the local scheme. Even though the surface stabilizes, the decaying convective boundary layer aloft may contain superadiabatic lapse rates. Rather than use (III-1) for the exchange coefficient, which is not suitable in the limit for large negative Ri, an alternative form originally suggested by Panofsky et al. (1960) is used and given by

$$K_m = K_H = (1 - 18\ Ri)^{-\frac{1}{2}}\ l^2 S. \qquad Ri < 0 \qquad \text{III-4}$$

In the twenty-four hour simulations which follow, the opposite transition (stable to unstable) does not occur; however, it can be consistently handled by redefining the PBL depth to that predicted by the local exchange coefficient model. Table III-1 gives a summary of the turbulent exchange formulation as a function of surface heat flux and local stability.

Table III-1 Summary of turbulent parameterization. $\overline{w'}\theta_o$ refers to the sign of the surface heat flux; $K_z|_h$ and $K_z|_{z_i} = 1 cm^2 s^{-1}$ are the exchange coefficients at the top of the surface layer and boundary layer, respectively.

---

$$K_z(z) = \begin{cases} K_z|_{z_i} + (z_i - z)^2/(z_i - h)^2 \;\; K_z|_h - K_z|_{z_i} & \\ \quad + (z - h) \;\dfrac{\partial}{\partial z^*} K_z|_h + 2(K_z|_h - K_z|_{z_i} & \\ \qquad\qquad (z_i - h) \quad , z_i \geq z \geq h & \\ K_z|_{z_i}, & z > z_i \\ (z/h)K_z|_h, & z < h, \end{cases} \qquad \overline{w'\theta}\Big|_o < 0$$

$$K_z = 1.1\,(R_{ic} - R_i)l^2 s/R_i \qquad \frac{\partial\theta}{\partial z} > 0$$

$$\overline{w'\theta}\Big|_o > 0$$

$$K_z = (1 - R_i)^{-\frac{1}{2}} l^2 s \qquad \frac{\partial\theta}{\partial z} < 0$$

## Radiative and Surface Forcing

Although the above discussion has emphasized the form of the exchange coefficients in the stable boundary layer, other aspects of the boundary layer, such as long-wave radiative flux divergence and specification of surface fluxes cannot be ignored. A surface energy budget (Mahrer and Pielke (1977)) which includes sensible, latent and soil heat fluxes as well as short and long-wave radiation is used to force the model at the surface. The non-dimensional profiles suggested by Businger (1973) are used to compute the surface fluxes.

In the atmosphere, local heating or cooling can occur due to long-wave radiative flux convergence or divergence. Because turbulent levels in the nocturnal boundary layer are relatively low, radiative contributions can be significant in the local heat budget. Sasamori (1972) gave an expression for local radiative flux divergence at a level z in the form

$$\frac{\partial F}{\partial z} = \int_{o}^{z} \frac{\partial A}{\partial z}(z,\xi)\,\frac{\partial B}{\partial \xi}\,d\xi + \int_{z}^{z_t} \frac{\partial A}{\partial z}(z,\xi)\,\frac{\partial B}{\partial \xi}\,d\xi \qquad \text{III-5}$$

where $A(z,\xi)$ is the absorption of the atmosphere slab between level z and $\xi$, $z_t$ is the model top, and B is the blackbody emission at temperature T (i.e. $B = \sigma T^4$). While III-5 gives a comprehensive representation of the radiative heating as a function of the complete distribution of temperature and absorbing medium, numerical evaluation of the complex integrals is quite tedious. Spurred by the need to simplify the numerical computations and guided by the suggestion that radiative exchange between a given level and space (or the ground) may be of primary importance, Sasamori made the assumption that the atmosphere was isothermal at the temperature at which divergence was being calculated.

Using this assumption, the integrals could be approximated and the divergence given by

$$\frac{\partial F}{\partial z} = (B\ (z) - B\ (o))\ \frac{\partial A}{\partial z}\ (z,o) + (B\ (z_t) - B\ (z))\ \frac{\partial A}{\partial z}\ (z,z_t) \qquad \text{III-6}$$

Although Sasamori found III-6 to give a good approximation to gross atmospheric cooling for large scale temperature structures, it was decided that a comparison of III-5 and III-6 should be made for the specific case of a finely resolved nocturnal boundary layer. As noted by an anonymous reviewer of a preliminary version of this chapter submitted to J. Atmos. Sci., strict use of either III-5 and III-6 might present problems when applied to a limited depth mesoscale model due to the over estimate of the effective radiating temperature of the top of the atmosphere. André et al. (1978) in their higher order turbulence model utilized III-5 with the inclusion of an additional term to more effectively include radiative cooling to space. The additional term was obtained using Sasamori's approximation that the atmosphere was isothermal above the model top except at infinity where the temperature was assumed to vanish. Thus, André et al.'s expression for the flux divergence was given by

$$\frac{\partial F}{\partial z} = \int_{o}^{z} \frac{\partial A}{\partial z}\ (z,\xi)\ \frac{\partial B}{\partial \xi}\ d\xi + \int_{z}^{z_t} \frac{\partial A}{\partial z}\ (z,\xi)\ \frac{\partial B}{\partial \xi}\ d\xi - \frac{\partial A}{\partial z}\ (z,\infty)\ B\ (z_t) \qquad \text{III-7}$$

Using the 0300 LST sounding for temperature and humidity from Day 34 of the Wangara Experiment (Clark et al. (1971)) expression III-7 and III-6 for flux divergence were employed to calculate radiative warming from

$$\frac{\partial T}{\partial t} = \frac{g}{c_p}\ \frac{\partial F}{\partial P} \qquad \text{III-8}$$

where pressures were determined hydrostatically from the temperature distribution. The absorption functions were calculated (Sasamori (1968)) from the humidity distribution by

$$A(z,\xi) = .846(\overline{Q} + 3.59 \times 10^{-5})^{.243} - 6.9 \times 10^{-2} \text{ for } Q < .01$$

and

$$A(z,\xi) = .240 \log_{10} (\overline{Q} + .01) + .622 \text{ for } Q \geq .01$$

where Q is the mean water vapor path length (g $cm^{-2}$) between levels z and .
Water vapor content above the top of the model needed to evaluate $A(z, \infty)$ was taken to be the same as assumed by André et al., (i.e. 3 Kg $m^{-2}$).

Figure III-1 gives radiative warming rates calculated from III-7 for the 0300 sounding compared to the approximate calculation. The details in the radiative cooling are due to fine scale structure in the Wangara temperature profile. As can be seen the approximate calculation (III-6), yields cooling rates which are close to those from the more complex calculation except the details are not accentuated.

Based upon these sensitivity studies it appears that Sasamori's isothermal atmosphere approximation is adequate for use in modeling the mean structure of the nocturnal boundary layer. From a computational view point, this approximation is important in a mesoscale model since the approximate calculation (III-6) was nearly seven times faster than the full radiative computation. Thus, this approximation has been utilized in all model experiments which follow.

Figure III-1 Radiative warming rates using Wangara Day 34 0300 LST temperature and humidity sounding. Dashed line is based on the complete calculation of equation III-7. Solid line is based on the isothermal approximation of equation III-6.

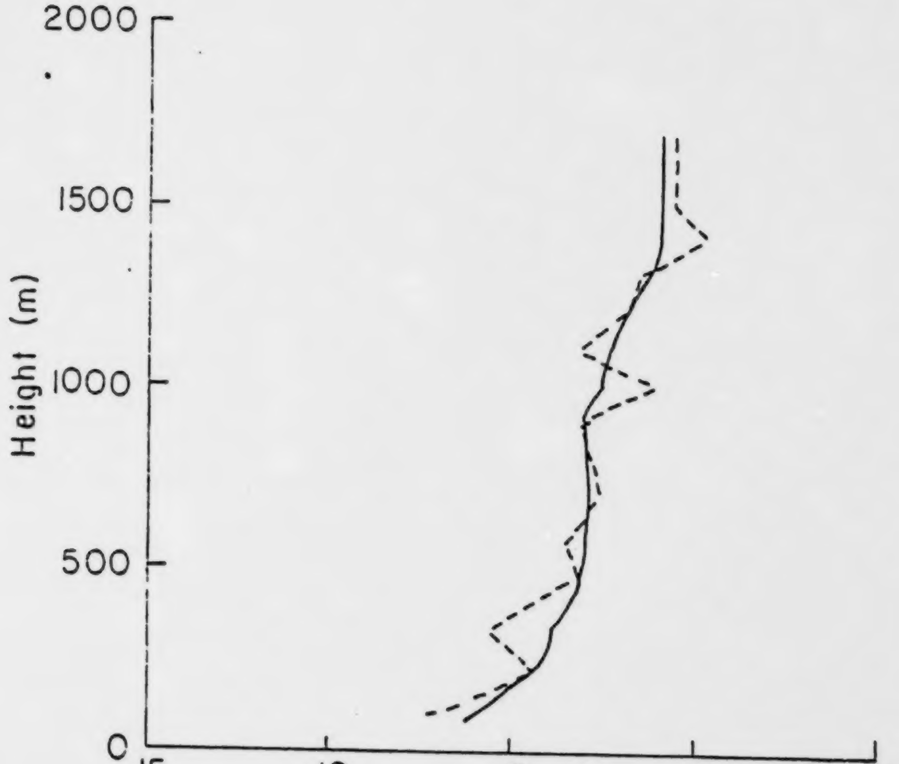
2000
1500
1000
500
0
Height (m)
-15
-10
-5
0
+5
Warming Rate ($10^{-5}$ °K $s^{-1}$)

Additional sensitivity studies were carried out to examine the effect of $CO_2$ as an absorber in the model atmosphere. Absorption functions for $CO_2$ given by Sasamori (1968) were utilized. Absorption band overlap between $CO_2$ and $H_2O$ was accounted for by adjusting the $CO_2$ absorption by the $H_2O$ absorption in the 15  band. It was found that although inclusion of $CO_2$ had a negligible effect on atmospheric cooling rates directly, it did increase the net downward flux at the surface, affecting surface temperatures. For example, in the full Wangara boundary layer experiments given in a subsequent section, the inclusion of the $CO_2$ downward flux increased minimum temperatures by approximately $3^{o}K$.

## Simulation of an Idealized Nocturnal Boundary Layer

The first simulation case uses a one-dimensional version of the model equations employing the local exchange scheme described in the previous section. A constant geostrophic wind of 4 m/s was imposed and an initial neutral Ekman profile was generated. Radiation was ignored and the ground surface was cooled at constant rate of .5 deg/hr.

A surface inversion began to form immediately and deepened with time. Velocities near the surface decreased initially while those aloft increased. Gradually a near steady state begin to develop as the accelerations decreased and the boundary layer height, as defined by the existance of turbulent activity, reached a constant value. The existence of a near steady state for a constant cooling rate is consistent with the results of Brost and Wyngaard (1978) and Rao and Snodgrass (1979).

Figure III-2 shows profiles of the exchange coefficients predicted in the present model after reaching a steady state compared to those deduced from higher order turbulence models of the stable boundary layer for equivalent stability. As can be seen, the magnitude and form of the exchange

Figure III-2 Profiles of exchange coefficients from the current model (X) for the idealized nocturnal boundary layer compared to those produced by more complex models for equivalent stability given by $|u_* / fL| = 65$. (from Rao and Snodgrass, 1979.)

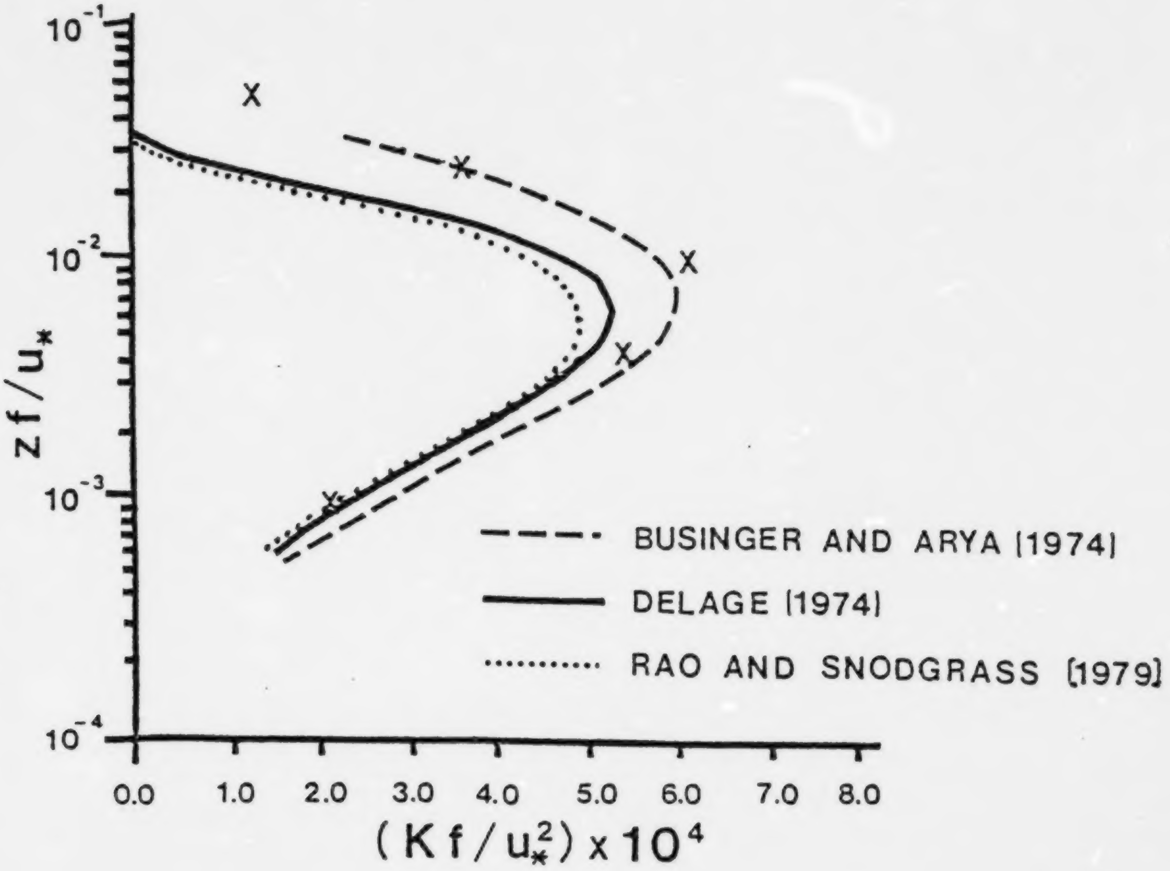
$10^{-1}$
$10^{-2}$
$10^{-3}$
$10^{-4}$
$zf/u_*$
0.0
1.0
2.0
3.0
4.0
5.0
6.0
7.0
8.0
$(Kf/u_*^2) \times 10^4$
BUSINGER AND ARYA (1974)
DELAGE (1974)
RAO AND SNODGRASS (1979)

coefficients using the local Richardson number agree well with the more complex models. The shape of the profile of the exchange coefficients for this case over flat land will be compared later with that in a drainage flow on a valley sidewall.

## Simulation of Wangara Days 33-34

André et al. (1978) noted that although considerable attention has been given to modeling the convective and nocturnal boundary layers separately, fewer studies have attempted simulations through the full diurnal cycle. In the recent literature, only the higher-order closure models, such as those of Yamada and Mellor (1975) or André et al. (1978), have been applied to the twenty-four hour simulation of the extensive Wangara data set (Clarke et al (1971)). In the following, we summarize the results of the simpler exchange coefficient model described earlier when applied to the Wangara Day 33-34 situation.

The model was initialized using the 0900 sounding on Day 33 and run until 0600 on Day 34. Geostrophic velocities and thermal shears were time-interpolated from the three-hourly observations in a similar fashion as performed by Yamada and Mellor. Soil characteristics for the surface energy budget and other pertinent parameters are given in Table III-2. Note that a surface roughness length of 1 cm was used rather than the 1.2 mm roughness length evidenced in the observations. This change is based on the previous works of Andre et al., and Yamada and Mellor which indicated that 1.2 mm was too small and actually reflected the smooth micrometeorological site rather than the general area. This conclusion was further substantiated in experiments with the present model which indicated that the 1.2 mm roughness gave nocturnal boundary heights much lower than observed.

Table III-2 Model parameters used for the Day 33-34 Wangara boundary layer simulation.

| | |
|---|---|
| Albedo | .2 |
| Latitude | 35°S |
| Surface Roughness | 1.0 cm |
| Soil Specific Heat Capacity | .5 cal $g^{-1}$ $K^{-1}$ |
| Soil Density | 1.2 g $cm^{-3}$ |
| Soil Conductivity | .003 cal $cm^{-1}$ $K^{-1}$ $S^{-1}$ |
| Number of Vertical Grid Levels | 18 |
| Time Step | 30 S |

As mentioned earlier, the daytime convective boundary layer segment of the simulation has been reported by Pielke and Mahrer (1975) with the exception that their model used specified surface temperatures while the current investigation employs the surface energy budget. Figure III-3 provides a time plot of the surface temperatures predicted by the surface energy budget in which interactions with the boundary layer are included. For comparison, the surface temperatures diagnosed by Deardoff (1974) which were used in the earlier study by Pielke and Mahrer (1975) are also given. The observed screen temperatures and modeled temperatures (brought to screen level using the similarity profiles) are also given in the figure and show good agreement through the diurnal cycle. The accompanying growth of the convective PBL and thermodynamic structure in this study are very similar to that described in the earlier study by Pielke and Mahrer (1975) and agree well with the observed behavior.

At sunset as the surface stabilizes, the exchange coefficients began to change dramatically. Figure III-4 shows the time evolution of the exchange coefficient structure. At mid-day the profile structure of the exchange coefficients in the convective boundary layer can be seen clearly while after sunset (2200) the structure is more complicated. Near the surface, a new shallow frictional boundary layer begins to grow with strong shear at the surface producing Richardson Number instability even in the face of the strong thermal stability. Aloft, small shears in conjunction with the near adiabatic lapse rates of the decaying convective boundary layer also produces Richardson Number instability and some turbulent mixing. This appears consistent with the results of André et al. which indicated a low level of turbulence in the remains of the convective boundary layer. By

Figure III-3 Time plot of model predicted surface and screen level temperatures compared with observed screen temperatures and Deardorff's diagnosed surface temperatures for Wangara Day 33-34.

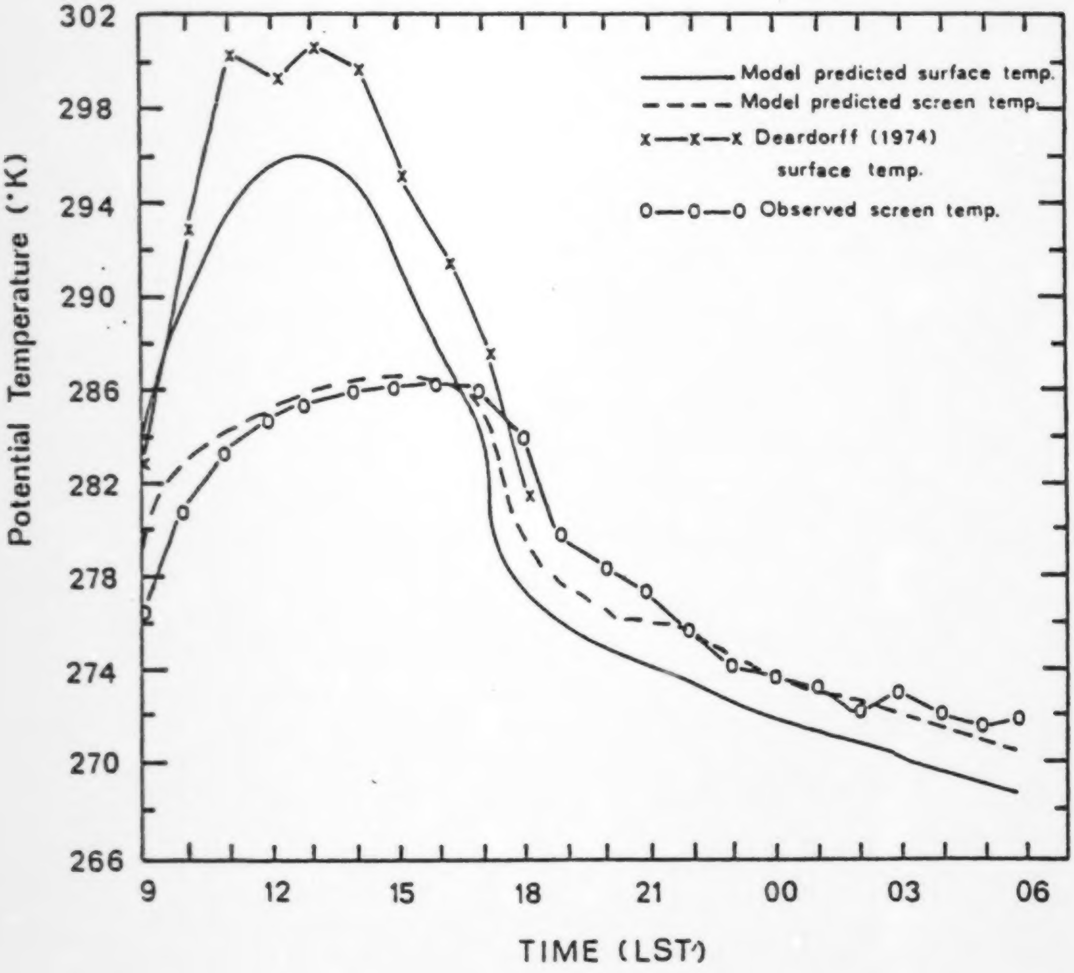
Model predicted surface temp.
Model predicted screen temp.
x—x—x Deardorff (1974) surface temp.
o—o—o Observed screen temp.
Potential Temperature (°K)
302
298
294
290
286
282
278
274
270
266
9
12
15
18
21
00
03
06
TIME (LST)

Figure III-4 Profiles of model predicted exchange coefficient, $K_H$, during the evolution of the boundary layer for Wangara Day 33-34..

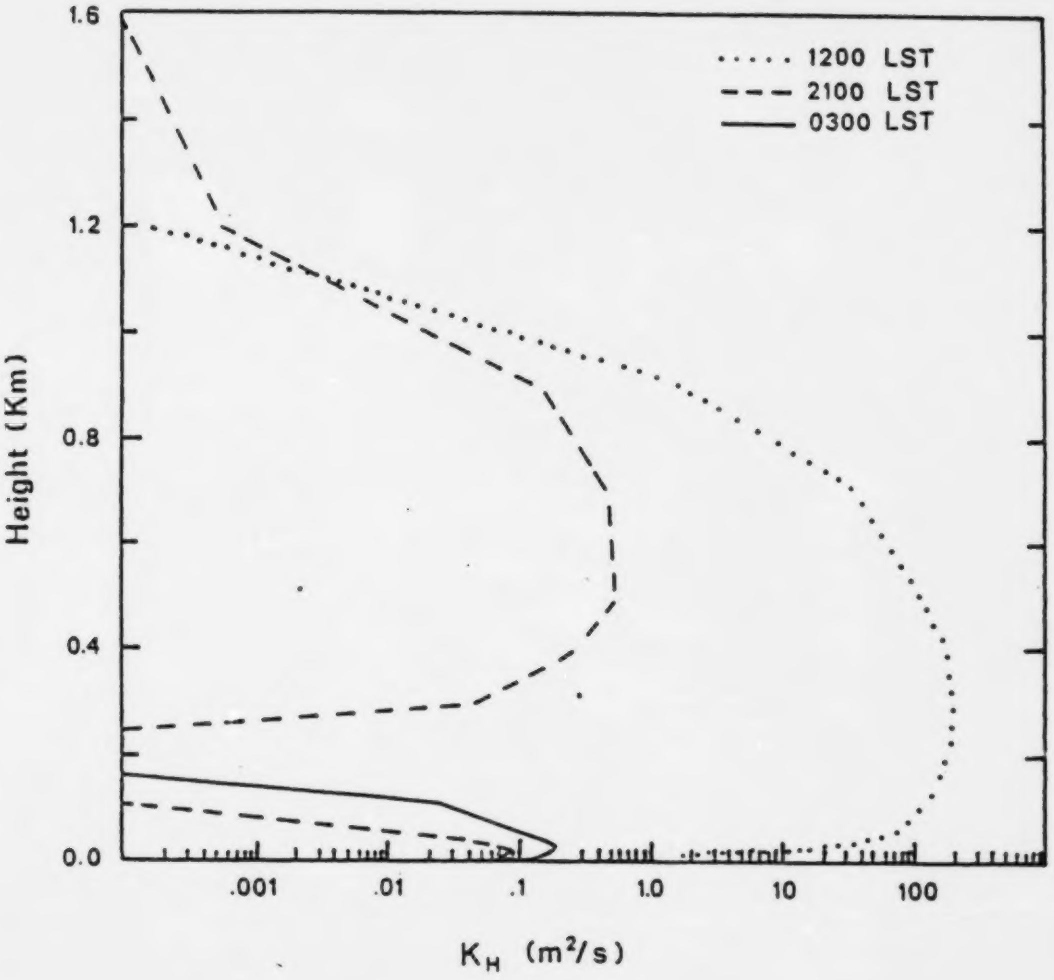
1200 LST
2100 LST
0300 LST
Height (Km)
1.6
1.2
0.8
0.4
0.0
.001
.01
.1
1.0
10
100
$K_H$ ($m^2/s$)

0300, the old convective boundary layer aloft has stabilized; but the new frictional boundary layer, as reflected in the vertical distribution of the exchange coefficients, has grown to a depth of near 175 meters.

The evolution of the modeled velocity field through the night and its interaction with the changing eddy viscosity is interesting and is shown in conjunction with the observations in Figures III-5 - III-7. During the day the u-velocity component shows significant departures below the geostrophic value in the lower part of the boundary layer in response to the frictional stress. At sunset as the turbulent stress decreases, the flow begins to accelerate; and by 0300, a pronounced supergeostrophic nocturnal jet has formed. As noted by Blackadar (1957) and Wipperman (1973), thermal shear in the opposite sense of the surface stress, as occurs here, produces a more pronounced jet than would a barotropic environment.

The nose of the nocturnal jet essentially defines the boundary layer depth in the model since large Richardson Numbers (see Figure III-8) at the nose of the jet inhibits vertical transfer. It can be noted that the modeled jets are slightly lower in magnitude and height than the wind maxima in the observations. This underestimate of the boundary layer depth was also found in the studies of André et al. (1978) and Yamada and Mellor (1975). Although André et al. ascribe the discrepancy to underestimates of the roughness length $z_0$, another factor which should be considered is uncertainty in the mesoscale pressure gradient. As can be seen at sunset, the flow field, seeking a new balance, accelerates in response to the existing pressure gradient; however, as emphasized by both Clark et al. (1971) and Yamada and Mellor (1975), this pressure gradient is difficult to measure precisely. Also, as will be stressed in the next section, mesoscale

Figure III-5 Model predicted and observed u and v components along with geostrophic components used in the simulation for 1200 LST Day 33 Wangara experiment.

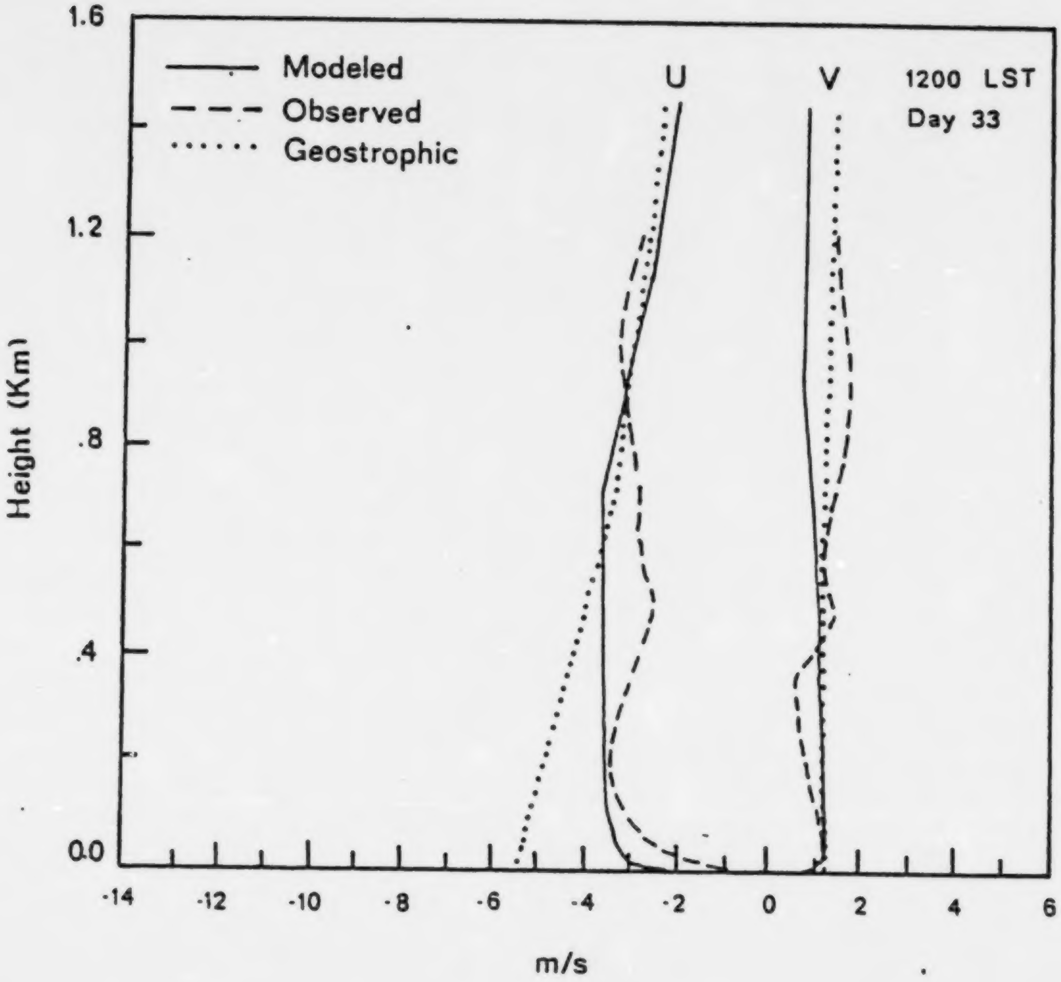
Modeled
Observed
Geostrophic
U
V
1200 LST
Day 33
Height (Km)
1.6
1.2
.8
.4
0.0
-14
-12
-10
-8
-6
-4
-2
0
2
4
6
m/s

Figure III-6 Same as 5. except for 2100 LST Day 33.

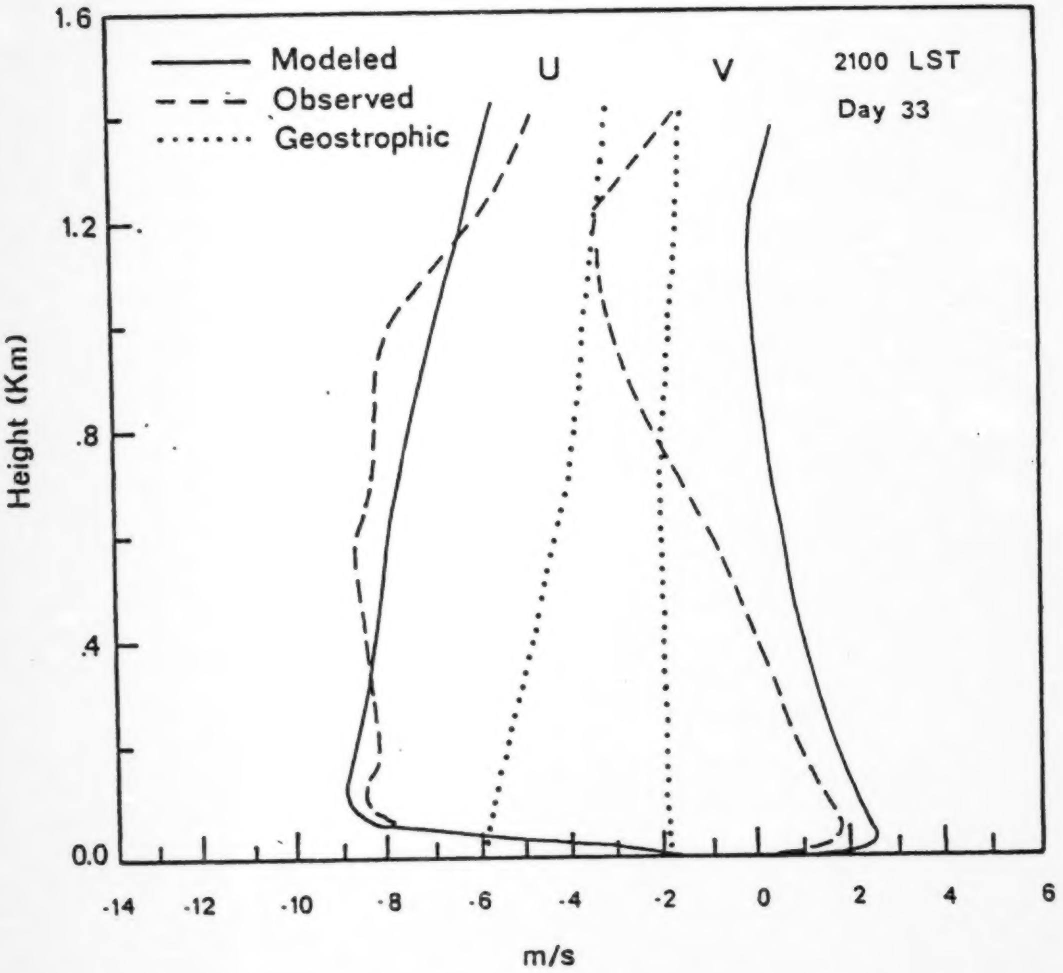
Modeled
Observed
Geostrophic
U
V
2100 LST
Day 33
Height (Km)
1.6
1.2
.8
.4
0.0
-14
-12
-10
-8
-6
-4
-2
0
2
4
6
m/s

Figure III-7 Same as 5. except for 0300 LST Day 34.

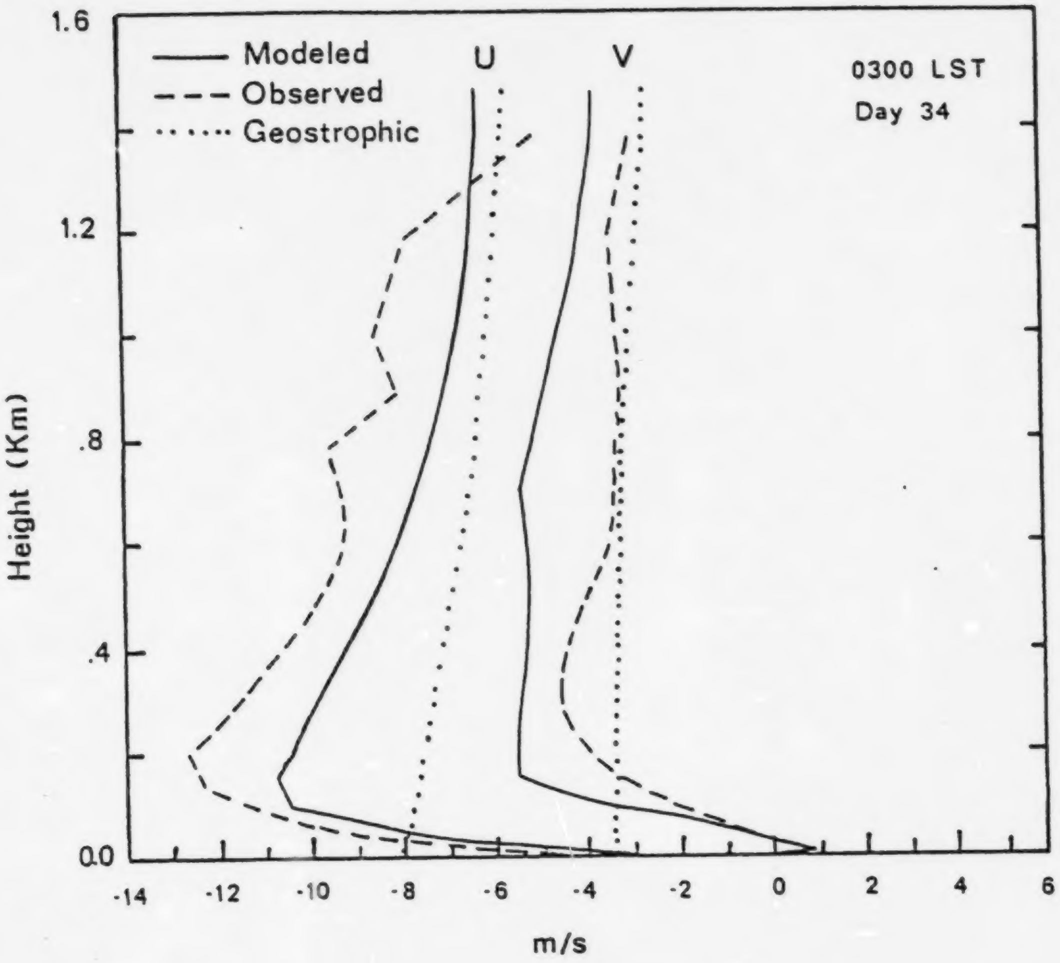
Modeled
Observed
Geostrophic
U
V
0300 LST
Day 34
Height (Km)
1.6
1.2
.8
.4
0.0
-14
-12
-10
-8
-6
-4
-2
0
2
4
6
m/s

Figure III-8 Profile of model predicted Richardson Number for 0300 LST Day 34. For comparison the critical Richardson Number from equation (3) is plotted.

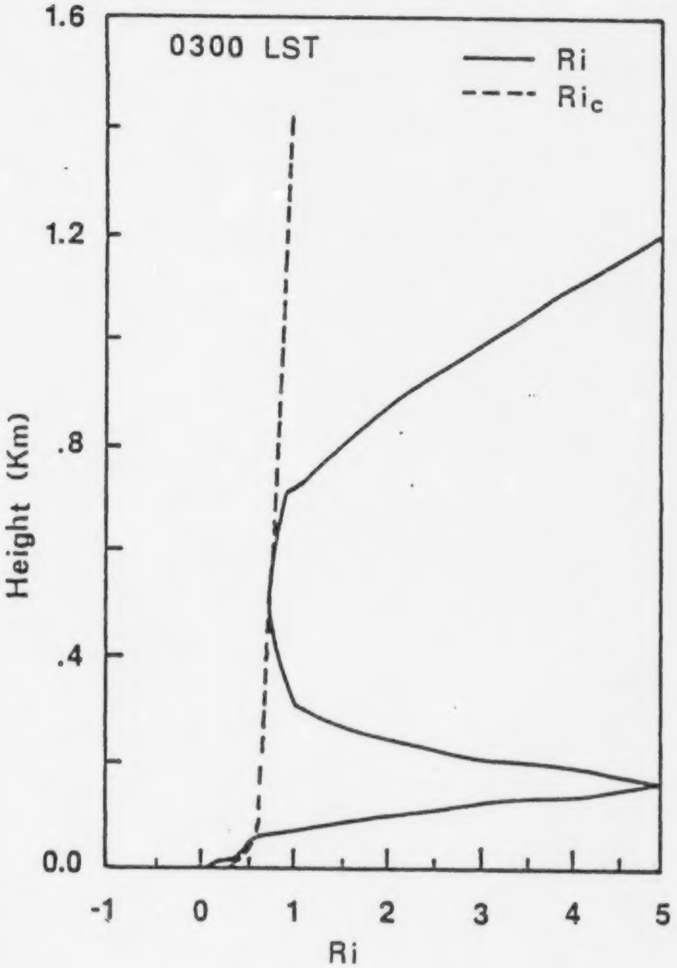
0300 LST
Ri
Ri$_c$
Height (Km)
0.0
.4
.8
1.2
1.6
-1
0
1
2
3
4
5
Ri

influences, such as sloping terrain and horizontal variations in surface heating can introduce localized pressure gradients and thermal shears not resolved in standard synoptic observations. Because of the interaction of the imposed geostrophic velocities and the shear near the surface, larger imposed geostrophic velocities have the same effect as larger roughness lengths in producing a deeper frictional boundary layer (i.e. both produce a larger $u_*$). The discrepancies in this simulation and also in the previously mentioned studies are, therefore, perhaps in part due to inaccuracies in specifications of the magnitude and structure of the mesoscale pressure gradient.

The evolution of the temperature structure and growth of the surface inversion along with modeled soil profiles are depicted in Figure III-9. Because the temperature structure is determined by both turbulent mixing and long-wave flux divergence, it is instructive to examine the model partitioning of these processes. Figure III-10 shows profiles of the turbulent and radiative contributions. During the day, as would be expected, the turbulent processes dominate the long-wave radiative effects. Early in the day, increasing surface turbulent fluxes provide turbulent warming near the surface while later as the radiative contribution increases, a shallow layer of turbulent cooling is evident. Also from Figure III-10, the rapid drop in modeled screen temperatures after sunset, as evidenced in Figure III-3, can be largely attributed to turbulent cooling. As the night progresses, the height of the maximum in the mean turbulent cooling rate rises in conjunction with the growth of the nocturnal inversion.

The near surface cooling rate through the night is decidedly non-steady and, as shown in Figure III-11, is marked by an interesting series of peaks. The peaks correspond to Richardson Number instability being realized

Figure III-9 Model predicted atmospheric temperature and soil temperature profiles for Day 33-34. (For clarity the soil temperature for 1800 LST is not shown.)

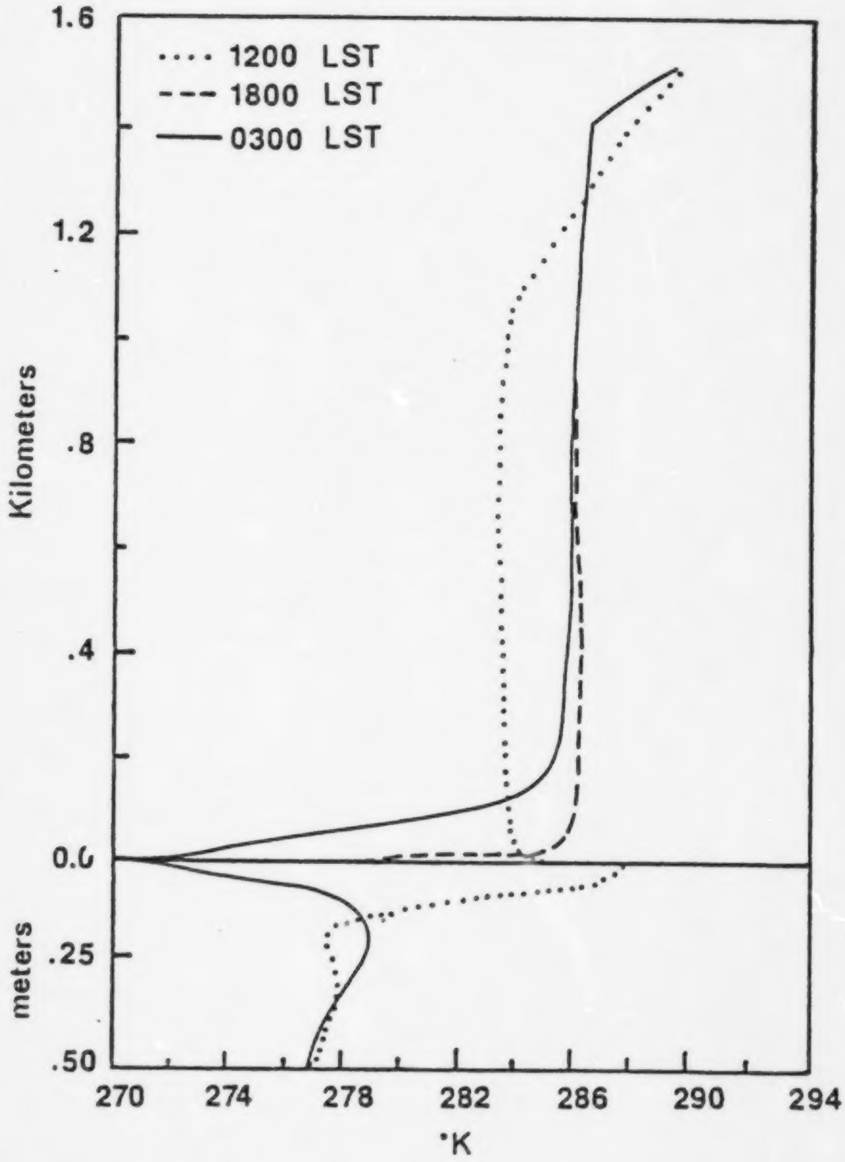

1200 LST
1800 LST
0300 LST
1.6
1.2
.8
.4
0.0
Kilometers
meters
.25
.50
270
274
278
282
286
290
294
°K

Figure III-10 Profiles of the partitioning of the turbulent and radiative contributions to local warming for 1200 LST, 2100 LST, and 0300 LST Day 33-34. Warming rates are one-hour averaged rates ending at the specified hour.

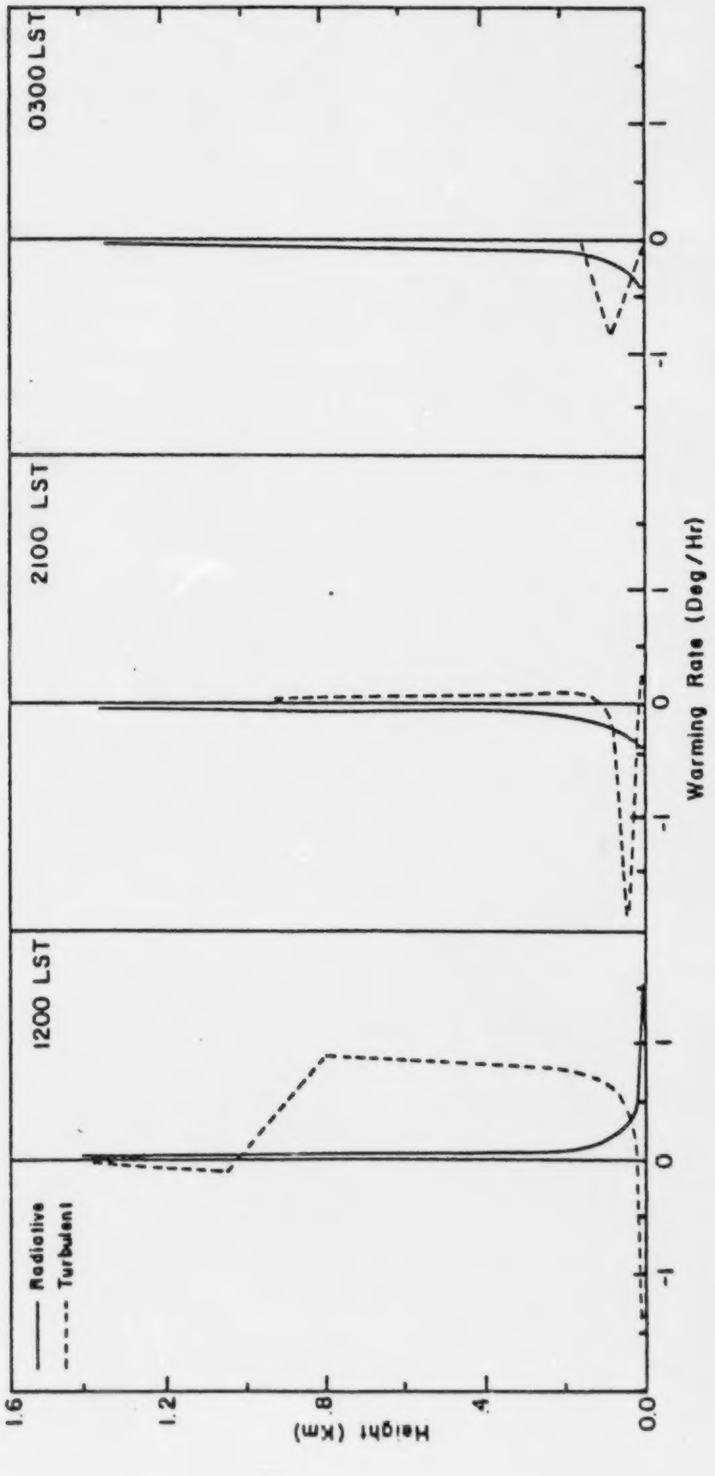
1200 LST
2100 LST
0300 LST
Radiative
Turbulent
Height (Km)
1.6
1.2
.8
.4
0.0
Warming Rate (Deg/Hr)
-1
0
1
-1
0
1
-1
0
1

Figure III-11 Time plot of model predicted local warming rate (radiative and turbulent) and temperature at 5 meters above ground.

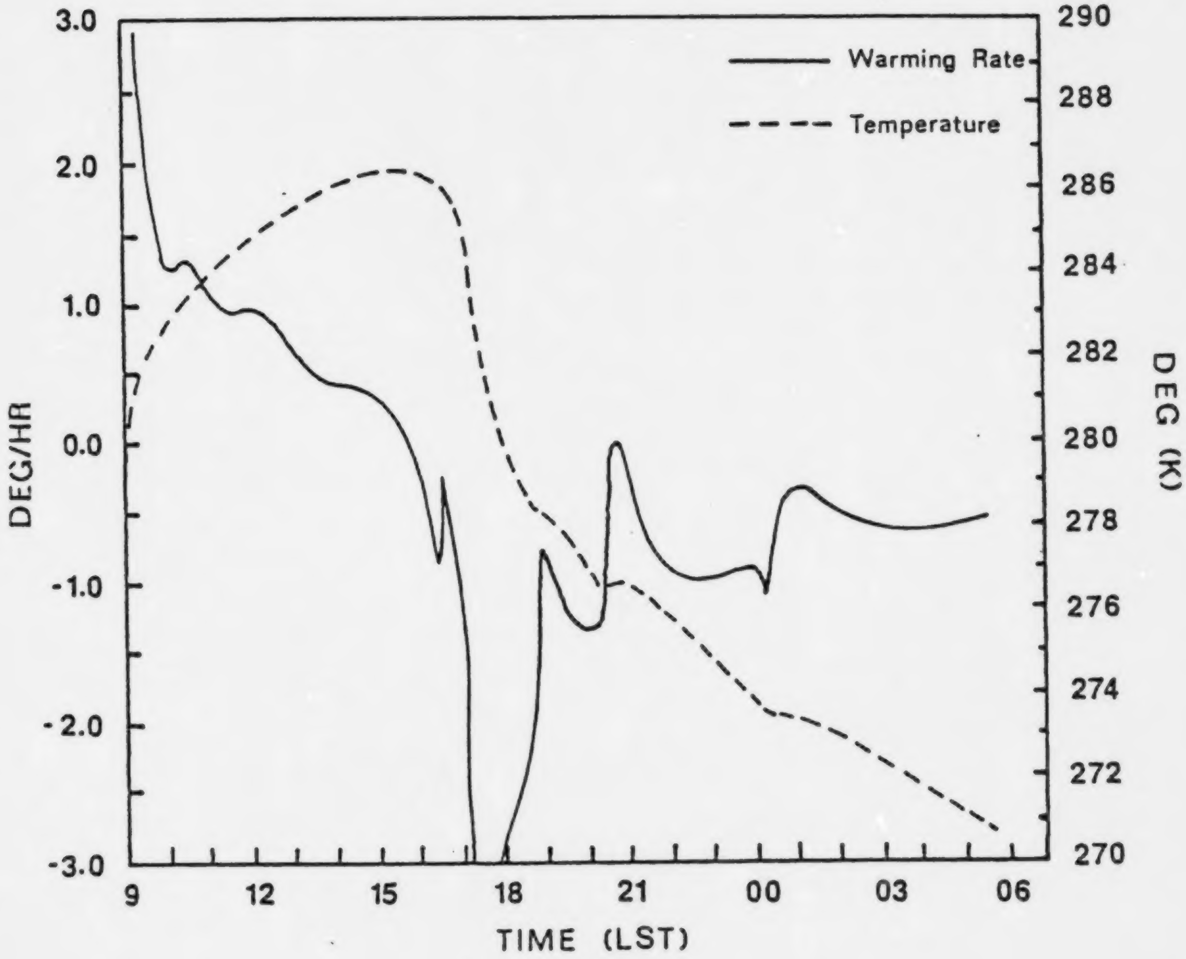
Warming Rate
Temperature
3.0
2.0
1.0
0.0
-1.0
-2.0
-3.0
DEG/HR
290
288
286
284
282
280
278
276
274
272
270
DEG (K)
9
12
15
18
21
00
03
06
TIME (LST)

simultaneously at several levels and corresponding rapid redistribution of momentum and temperature. The peaks are also manifested as humps in the temperature trace in Figure III-3 and Figure III-11, and it is interesting that the observed trace also shows similar humps, though at different times. Two factors evidently contribute to the phenomenon. First, the inertial acceleration in the velocity field leads to large wind shears near the ground. Also, the observed geostrophic velocities increased throughout the night. The combined increase in winds aloft produces larger surface shears ultimately leading to Richardson Number instability and in turn to increased surface stress. Since the equilibrium boundary layer height is evidently a function of $u_*$, (Yu(1978)) the boundary layer depth grows through the night in response to the larger surface stress. The growth occurs sporadically as breakdowns in equilibrium occurs. Blackadar (1979) found similar features in his model and compared them to the turbulent bursting phenomenon found in observations. (see for example Kaimal and Izumi (1965) or Shubert and Pepper (1976)).

In summary, it appears that the combined profile and local exchange coefficient formulation does a good job in modeling the diurnal evolution of the planetary boundary layer. Discrepancies noted in the simulation of the Wangara data, such as underestimates of the height of the nocturnal boundary layer and screen temperatures, also appear to be found in the higher closure models of André et al. (1978), and Yamada and Mellor (1975).

## Sloping Terrain of the Great Plains

Some of the more interesting features of the stable boundary layer are low level wind maxima or jets which have been documented observationally in diverse locations and intensively studied. (For a review, see Wipperman

(1973)). Although alternate hypotheses have been offered (e.g. Uccellini and Johnson (1979) or Wexler (1961)), the low-level jets have been more generally recognized to be essentially a complex response of the atmospheric boundary layer to the diurnal cycle of thermal forcing. The thermal forcing can contribute to the jets' development through two mechanisms: 1) time dependent variation in the effective eddy viscosity in the boundary layer, and 2) production of a diurnal thermal wind component over sloping terrain or other diurnally forced baroclinic zone.

The first mechanism, introduced by Blackadar (1957), relies on the fact that as the boundary layer stabilizes at the surface at sunset the frictional stress in the remaining daytime convective boundary layer is reduced dramatically. Blackadar showed that the reduction in stress aloft leads to an acceleration in the velocity as the wind field adjusts to a new balance with the existing pressure gradient. During this adjustment to the geostrophic wind, an inertial oscillation develops in which the wind will become supergeostrophic. Because of the general applicability of the physical processes involved, this mechanism probably explains the widespread and common existence of nocturnal jets in diverse locations.

Climatological studies of the low level jet, however, (e.g. Bonner (1968)), have shown that certain areas, such as the Great Plains of the U.S., exhibit higher frequencies of occurrence and more intense low level jets than at most other locations. Because of the sloping terrain over the Great Plains, investigators (e.g. Holton (1967)) have suspected that diurnal wind oscillations due to the heating and cooling of elevated terrain could be responsible for the strength and persistence of the jets. Hoecker (1965) found that strong oscillations did exist in deduced surface geostrophic winds from measurements over the Great Plains. However, these observations as well as conceptual ideas of the manner in which geostrophic winds should vary over sloping terrain indicated that the geostrophic maxima were out of phase with the observed winds. Using a simplified analytical model, Bonner and Paegle (1970) demonstrated that joint consideration of a time varying geostrophic component and a time varying eddy viscosity (with specified lag to the geostrophic component) could produce strong wind maxima at approximately the times indicated by observations.

It is the purpose of this section to examine the diurnal boundary layer development and thermal wind oscillations over sloping terrain using a numerical model. Use of a numerical model allows interaction between vertical mixing processes and the evolving terrain induced pressure gradient in the convective and stable boundary layers. This fully integrated approach is shown to be important because the phase and amplitude of the oscillating thermal wind component is dependent upon the boundary layer mixing processes while the boundary layer structure itself is a function of the resulting geostrophic velocities.

The one-dimensional boundary layer model described and tested in the previous sections was incorporated into the full mesoscale model described in Chapter II. These equations were used to examine boundary layer development over sloping terrain. For comparison with model results, cross-sections of the low level jet over the Great Plains (Hoecker (1963)) using data from a special pibal network from Amarillo, Texas to Little Rock, Arkansas, are presented in Figure III-12. Rather than attempt a detail case study simulation of actual data, idealized sloping topography was used to gain insight into the interaction of the boundary layer with the diurnally heated sloping terrain.

Figure III-12 Contours of northerly (v) velocity component over sloping terrain as reported by Hoecker (1963) from a special pibal network between Amarillo, Texas, and Little Rock, Arkansas. Contour interval is 5 m/s.

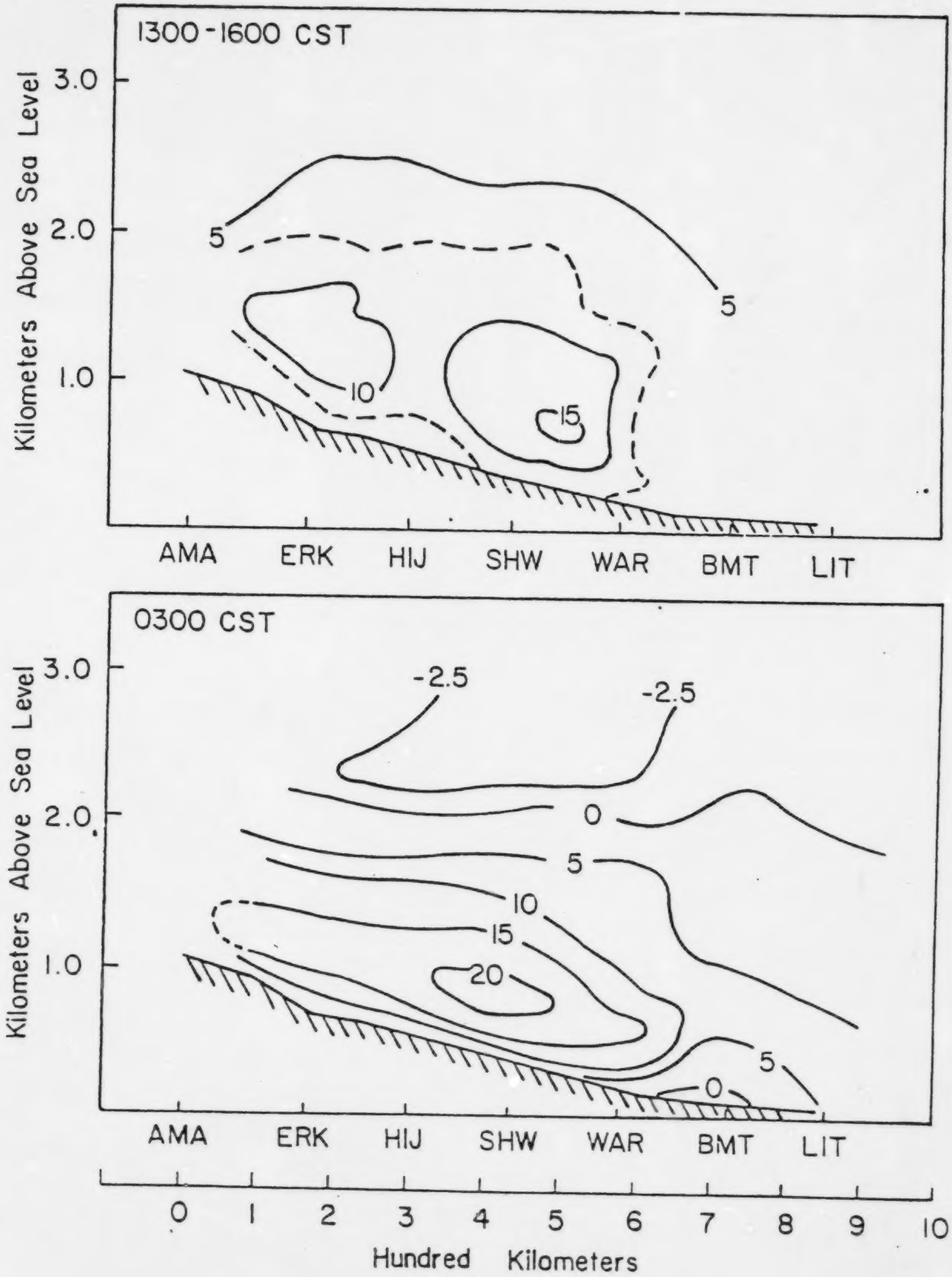
1300-1600 CST
0300 CST
Kilometers Above Sea Level
3.0
2.0
1.0
5
10
15
-2.5
0
20
AMA
ERK
HIJ
SHW
WAR
BMT
LIT
0
1
2
3
4
5
6
7
8
9
10
Hundred Kilometers

The first model case[1] employs topography sloping from west to east with a slope of .002 and having a lateral extent of 900 Km. This configuration approximates the extensive gradual slopes of the Great Plains. The model was initialized using the 0635 CST sounding at O'Niell, Nebraska, taken on August 31, 1953, during the Sixth General Observing Period (see Lettau and Davidson (1957)). To depict more clearly the effect of the terrain, a constant large scale geostrophic southerly component of 10 m/s was imposed throughout the integration rather than the more complex observed geostrophic components. Soil characteristics needed for the surface energy budget were also taken from the O'Niell experiment and are given in Table III-3 along with other information. To avoid spurious accelerations in the model initialization, a barotropic state was constructed by making potential temperature lines parallel to geopotential levels. The surface temperatures over the elevated terrain were initialized consistent with this scheme so that in effect cooler actual surface temperatures were specified over the higher elevations. Figure III-13 shows the sloping terrain and the prescribed initial potential temperature field. The initial velocity field was uniform except for adjustment to a neutral Ekman boundary layer.

The model was run from the initial state for twenty-four hours, beginning at sunrise. As the day progressed, surface heating produced a nearly adiabatic convective boundary layer extending to a maximum depth of approximately 2.5 km above the terrain. Figure III-14 shows the baroclinic zone that developed over the sloping terrain and the velocity maximum aloft in the boundary layer. Although weaker, the velocity maximum appears similar to the daytime maximum described by Hoecker (1963) in Figure III-12.

---

[1] In this experiment the material surface s was allowed to vary using the time dependent model top as utilized in Mahrer and Pielke (1975). In the drainage flow problems reported in later Chapters s was held constant.

Table III-3 Model parameters for sloping terrain cases

| | Case 1 | Case 2 | Case 3 |
|---|---|---|---|
| Latitude | 45°N | 45°N | 30°N |
| Slope | .0018 | .0036 | .0018 |

| | All Cases |
|---|---|
| Surface Roughness | 1 cm |
| Albedo | .2 |
| Soil Specific Heat Capacity | .37 cal $g^{-1}$ $K^{-1}$ |
| Soil Density | 1.6 g $cm^{-3}$ |
| Soil Conductivity | .002 cal $cm^{-1}$ $K^{-1}$ $S^{-1}$ |
| Number of Vertical Grid Levels | 14 |
| Number of Horizontal Grid Points | 43 |

Figure III-13 Terrain configuration used in the model and the specified initial potential temperature field for Case 1. Contour interval is 1°K.

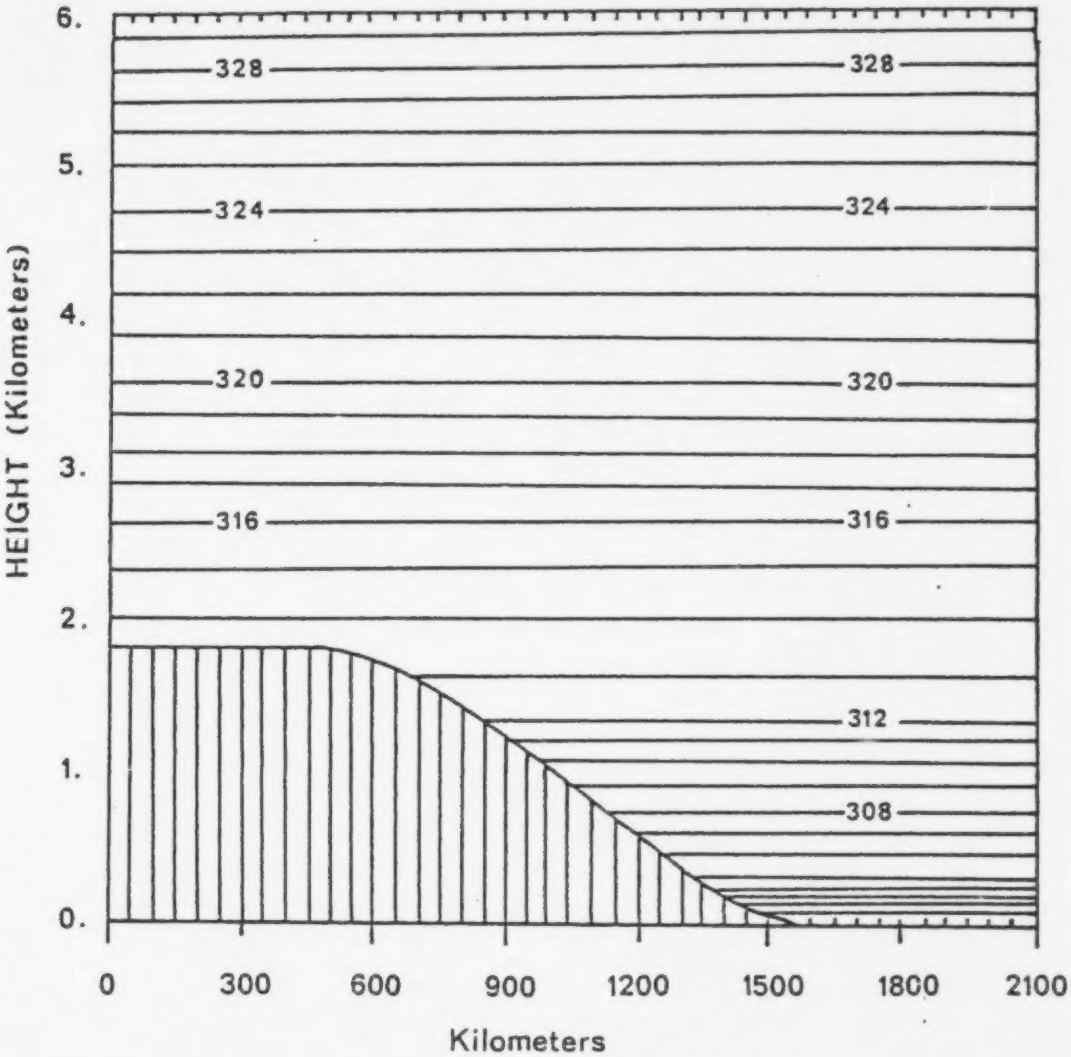
HEIGHT (Kilometers)
6.
5.
4.
3.
2.
1.
0.
328
328
324
324
320
320
316
316
312
308
0
300
600
900
1200
1500
1800
2100
Kilometers

Figure III-14 Composite V-component (solid) and potential temperature (dashed) contours at 1500 LST showing the development of the convective boundary layer and baroclinic zone over the sloping terrain for Case 1. Contour intervals are 1 m/s and 1°K.

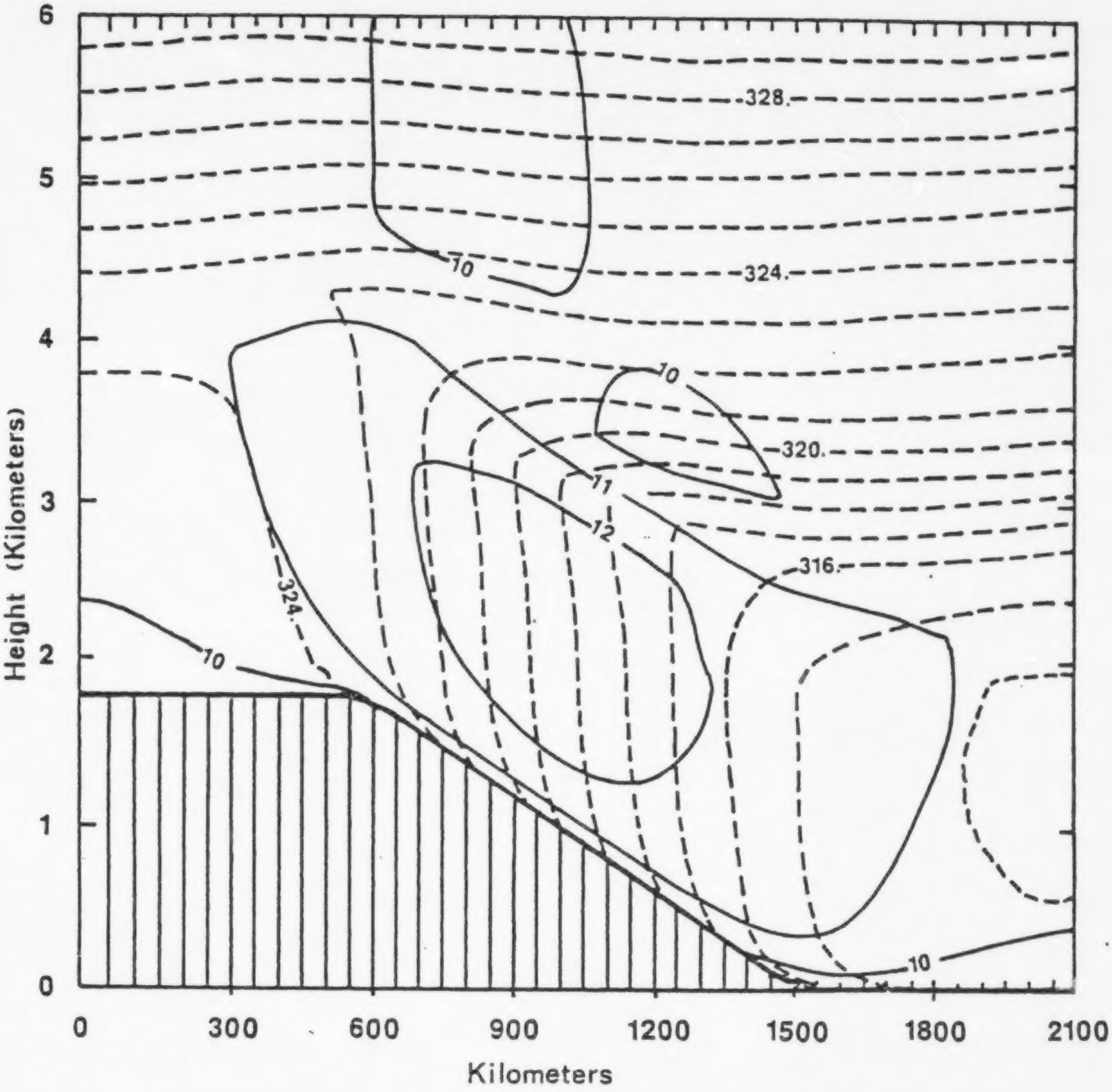

6
5
4
3
2
1
0
Height (Kilometers)
328.
10
324.
10
320.
11
12
316.
324.
10
10
0
300
600
900
1200
1500
1800
2100
Kilometers

To examine the development of the thermal wind component over the sloping terrain in the model, it is useful to define a mesoscale geostrophic component, $V_{gm}$, from the u-momentum equation so that

$$V_{gm} = \left( \theta \frac{\partial \tilde{\pi}}{\partial x} - g \frac{z^* - \bar{s}}{\bar{s}} \frac{\partial z_G}{\partial x} + g \frac{z_*}{s} \frac{\partial s}{\partial x} \right) / f \qquad \text{III-9}$$

The total geostrophic component, $V_{gt}$, is then

$$V_{gt} = V_{gm} + V_{gs} \qquad \text{III-10}$$

where $V_{gs}$ is the synoptic geostrophic component. By taking $\frac{\partial}{\partial z^*}$ of III-9 and substituting from the hydrostatic equation , a simple two-term expression for the thermal wind can be obtained as

$$\frac{\partial V_{gm}}{\partial z^*} = \left( \frac{\partial \theta}{\partial z^*} \frac{\partial \tilde{\pi}}{\partial x} + \frac{g}{\theta} \frac{s - z_G}{\bar{s}} \frac{\partial \tilde{\theta}}{\partial x} \right) / f \qquad \text{III-11}$$

In the initial conditions for the model as specified in Figure III-12, the pressure gradient terms balance, i.e.

$$\theta \frac{\partial \tilde{\pi}}{\partial x} = g \frac{z^* - \bar{s}}{\bar{s}} \frac{\partial z_G}{\partial x} \qquad \text{III-12}$$

(see Mahrer and Pielke (1977)). Taking $\frac{\partial}{\partial z^*}$ of III-12 and again substituting using the hydrostatic equation, we find that

$$\frac{\partial \theta}{\partial z^*} \frac{\partial \tilde{\pi}}{\partial x} = - g \frac{s - z_G}{\bar{s}} \frac{\partial \theta}{\partial x} \qquad \text{III-13}$$

Using this in the thermal wind expression (III-11) it can be seen that with the initial conditions as specified, the two terms exactly balance and $\frac{\partial V_{gm}}{\partial z^*}$ is zero, which is consistent with the concept of the specified initial barotropic state.

As the integration proceeds, it is instructive to examine the behavior of the two terms. Over the sloping terrain as shown in Figure III-13 on a constant $z^*$ surface, $\frac{\partial \tilde{\pi}}{\partial x} > 0$ and $\frac{\partial \tilde{\theta}}{\partial x} < 0$. In the daytime, $\frac{\partial \tilde{\theta}}{\partial z^*}$ is negative in the superadiabatic surface layer and is near zero through most of the convective boundary layer. Therefore, both terms in (III-11) are negative and the mesoscale geostrophic component must decrease with height. Figures III-15 and III-16 give profiles of u and v at 0930 LST and 1530 LST and show the evolution of the geostrophic component and the decrease in $V_{gt}$ with height which is consistent with the discussion presented here. Note also that the decrease is sharpest in the surface layer where the negative contribution of the term $\frac{\partial\tilde{\theta}}{\partial z^*}$ in (III-11) is the largest. As noted by Hoecker (1965) following Blackadar (1957), interaction between the frictional stress and geostrophic shear alters the classic Ekman spiral to produce, in this case, a broad maximum in the v component near the top of the boundary layer.

The development of a strong nocturnal jet after sunset is directly related to the growth of the mesoscale pressure gradient due to the heating of the sloping terrain during the day. At sunset, as the effective frictional stress is reduced in the dying convective boundary layer, the velocity accelerates as the velocity field begins to adjust to the total pressure gradient (or $V_{gt}$) which includes a mesoscale as well as an imposed synoptic component. The result of the inertial overshoot is therefore extremely large "supergeostrophic" velocities if the synoptic gradient is used as a baseline. Figure III-17 shows the development of the strong nocturnal jet. A recent study by Chang (1979) which simulated the O'Neill data but which did not include terrain effects also produced supergeostrophic velocities due to inertial effects alone, but the strength of the jet was much less than that observed or that presented here.

At night as the surface begins to cool, an opposite thermal wind component develops as the baroclinicity reverses from that generated during the day. At night $\frac{\partial\tilde{\theta}}{\partial z^*}$ is positive in the nocturnal boundary layer so that the two terms in (III-11) now have opposite signs. With a strong

Figure III-15 Profiles of model predicted u and v components at 0930 LST along with profiles of the total geostrophic component $V_{gt}$ over the center of the sloping terrain for Case 1.

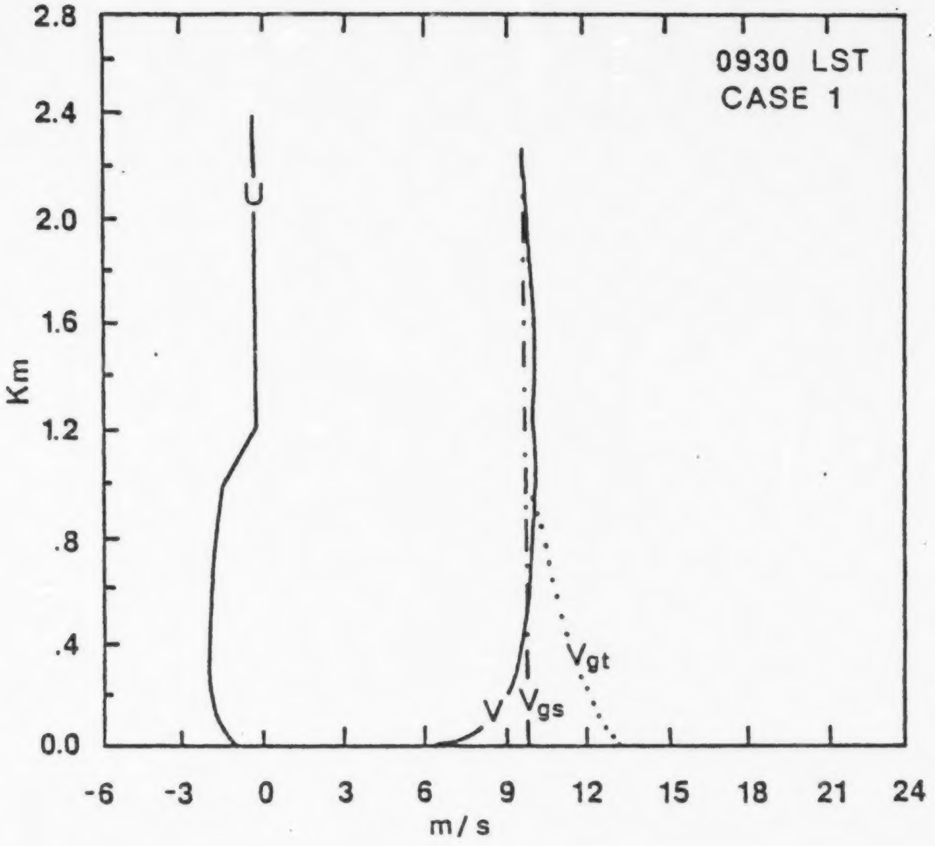
0930 LST
CASE 1
U
V
$V_{gs}$
$V_{gt}$
Km
2.8
2.4
2.0
1.6
1.2
.8
.4
0.0
-6
-3
0
3
6
9
12
15
18
21
24
m/s

Figure III-16  Same as Figure III-15 except for 1530 LST. (Case 1)

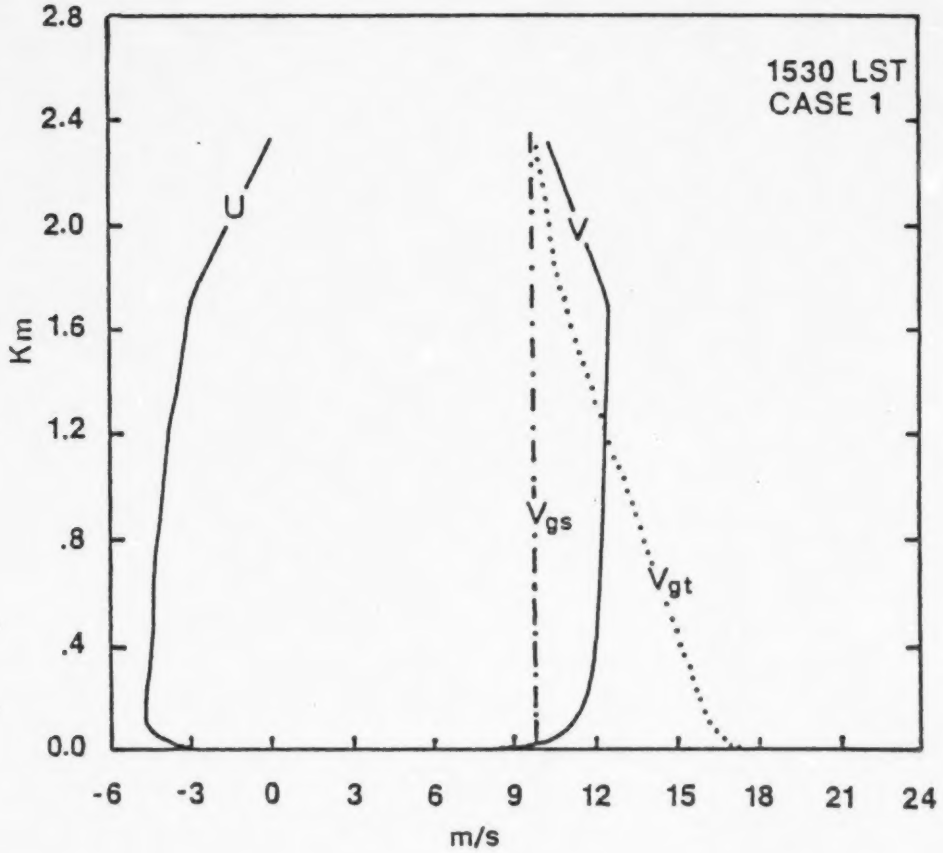
2.8
2.4
2.0
1.6
1.2
.8
.4
0.0
Km
-6
-3
0
3
6
9
12
15
18
21
24
m/s
1530 LST
CASE 1
U
V
$V_{gs}$
$V_{gt}$

Figure III-17  Same as Figure III-15 except for 2330 LST. (Case 1)

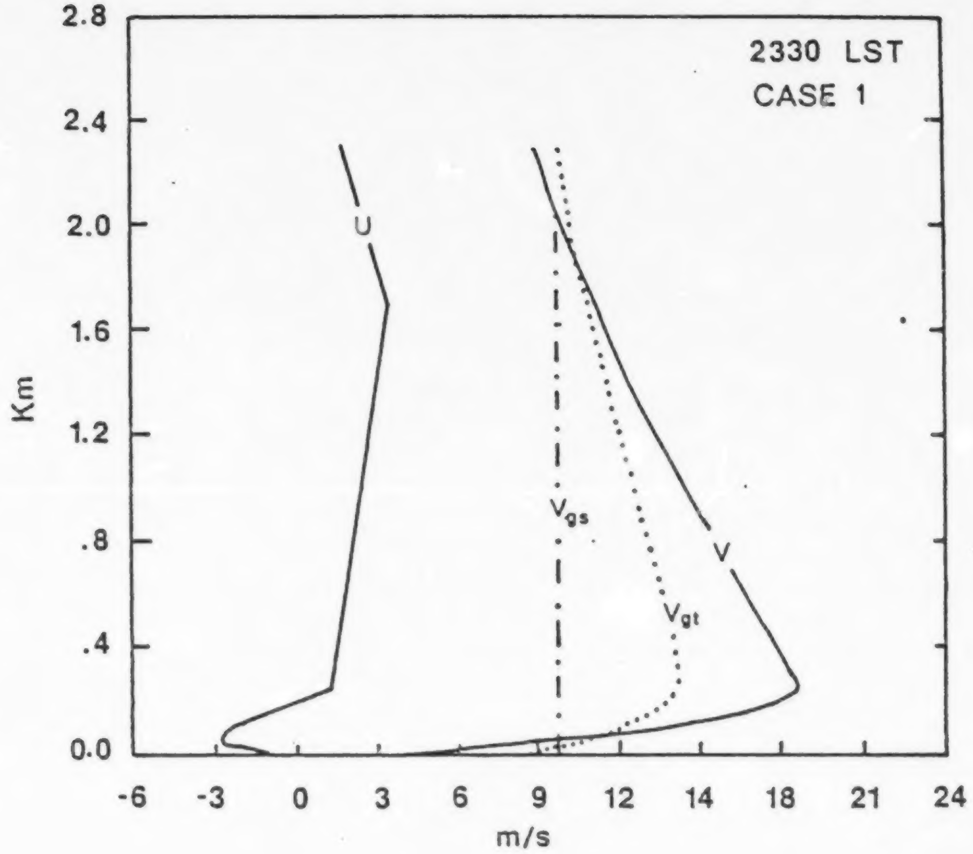
2330 LST
CASE 1
2.8
2.4
2.0
1.6
1.2
.8
.4
0.0
Km
-6
-3
0
3
6
9
12
14
18
21
24
m/s
U
V
$V_{gs}$
$V_{gt}$

inversion, $\frac{\partial \tilde{\theta}}{\partial z^{*}}$ becomes large so that $\frac{\partial V}{\partial z^{*}}{}_{gm}$ becomes positive and the thermal shear is now opposite to that of the daytime case. Figure III-17 shows the increase in the geostrophic wind with height near the surface. This produces surface geostrophic winds which are now less than the imposed synoptic geostrophic winds and much less than the maximum geostrophic surface winds occurring in the late afternoon. Although Bonner and Paegle (1970), Hoecker (1965) and others have discussed this oscillation, it appears that its relationship to the nocturnal boundary layer growth and its limited height have been neglected. Since the nocturnal boundary layer height can be roughly defined as that height to which significant cooling occurs, it appears that this should also be the limiting height for the reversal in baroclinicity. Note that aloft in the old convective boundary layer where $\frac{\partial \tilde{\theta}}{\partial z^{*}} \simeq 0$ the second term in (III-11) still gives $\frac{\partial V}{\partial z^{*}}{}_{gm}$ decreasing with height (also shown in Figure III-16). The fact that the thermal wind oscillation is not complete through the depth of the old convective boundary layer (because the nightime boundary layer is shallower than the daytime mixed layer) allows the nocturnal jet to remain strong even though surface geostrophic velocities decline. A time variation of actual and geostrophic velocities are given in Figure III-18 and are similar to those over the Great Plains described by Hoecker (1965). Paegle (1978) in a quasi-analytical study indicated that solutions over the three-dimensional topography were sensitive to the amplitude and decay rate of an imposed temperature oscillation. The results here indicate that the amplitude and decay rate are intimately related to the boundary layer processes and cannot be simply parameterized.

Figure III-18 Time variation of actual vector velocity at 300 m and surface geostrophic vector velocity for Case 1. Times are given to the side of the velocities.

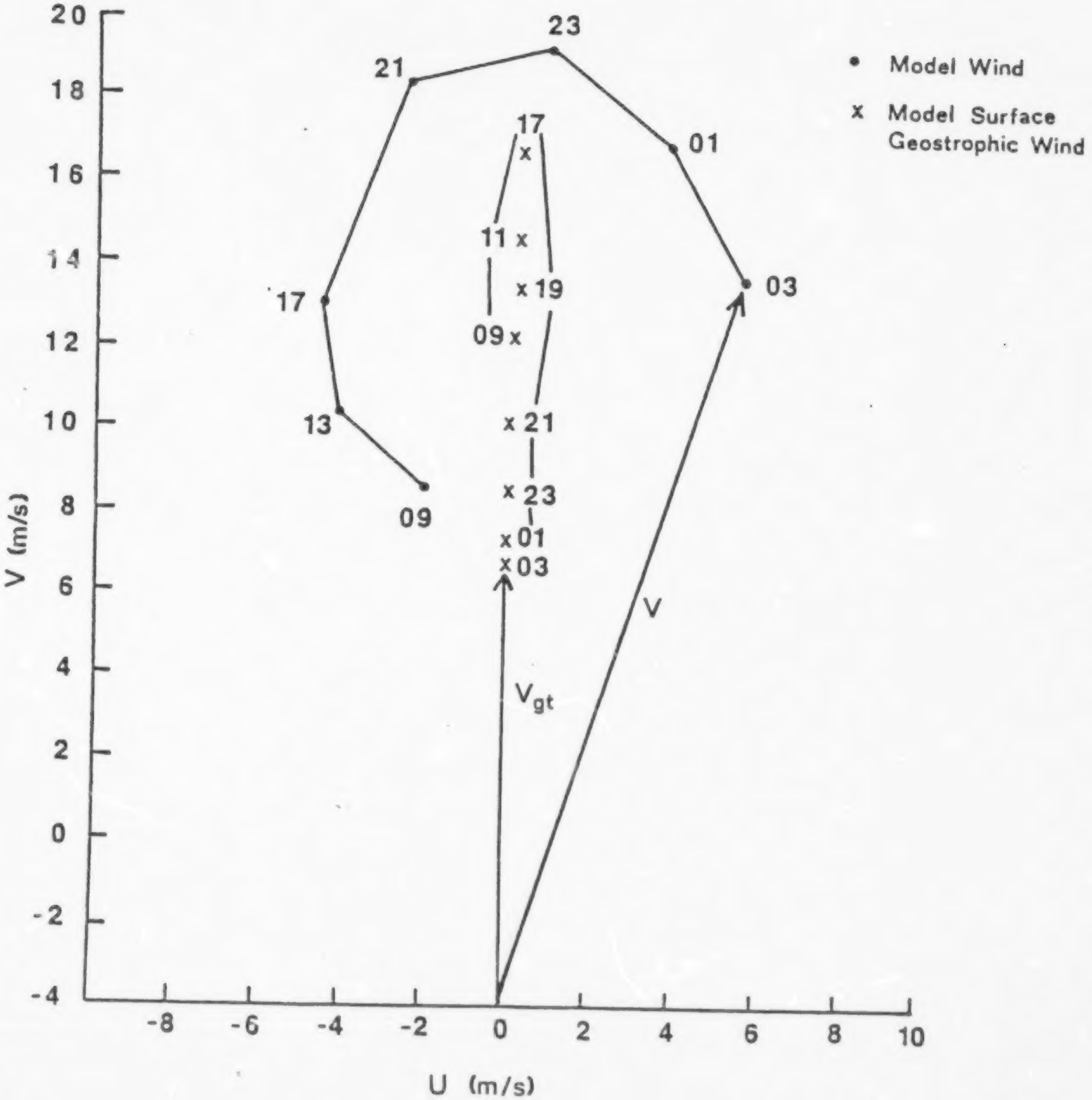
• Model Wind
x Model Surface Geostrophic Wind
23
21
01
17
03
13
09
17
11
x 19
09
x 21
x 23
x 01
x 03
V
$V_{gt}$
V (m/s)
20
18
16
14
12
10
8
6
4
2
0
-2
-4
-8
-6
-4
-2
0
2
4
6
8
10
U (m/s)

Figure III-19 shows the core of the nocturnal jet over the center of the sloping terrain and can be compared to Hoecker's diagram in Figure III-12. The strength of the jet is slightly less than in Hoecker's observations, and the observed component drops to near zero at 2 Km. These discrepancies in magnitude can probably be ascribed to differences in large scale forcing, such as the existence of a synoptic scale temperature gradient producing thermal shear in the geostrophic wind which would be superimposed on the thermal forcing of the terrain. Also, as will be discussed next, the magnitude of the terrain slope is important to the strength of the jet. As such, local terrain slopes in the real topography larger than those considered in this first case would contribute to discrepancies in the strength of the modeled jet.

Additional experiments were undertaken to evaluate the impact of terrain slope and latitude on the boundary layer development as outlined in Table III-3. Case 2 in which the terrain slope was doubled produced stronger mesoscale pressure gradients and resulting nocturnal jets (see Figures III-20 and III-21). Figure III-22 shows velocity profiles after the peak in the inertial overshoot has occurred. As can be seen, the terrain-induced geostrophic component still maintains a significant component to the north above the nocturnal boundary layer. Thus, although Blackadar's inertial theory produces significant overshoot to the total mesoscale and synoptic geostrophic velocities and significant jet formation, the maintenance of the mesoscale pressure gradient aloft keeps velocities larger than the synoptic geostrophic values even after the inertial peak has passed.

Figure III-19 Contours of (a) northerly (v) component and (b) potential temperature ($\theta$) over the sloping terrain at 2230 LST for Case 1. Contour intervals are 2 m/s and $1^{o}$K.

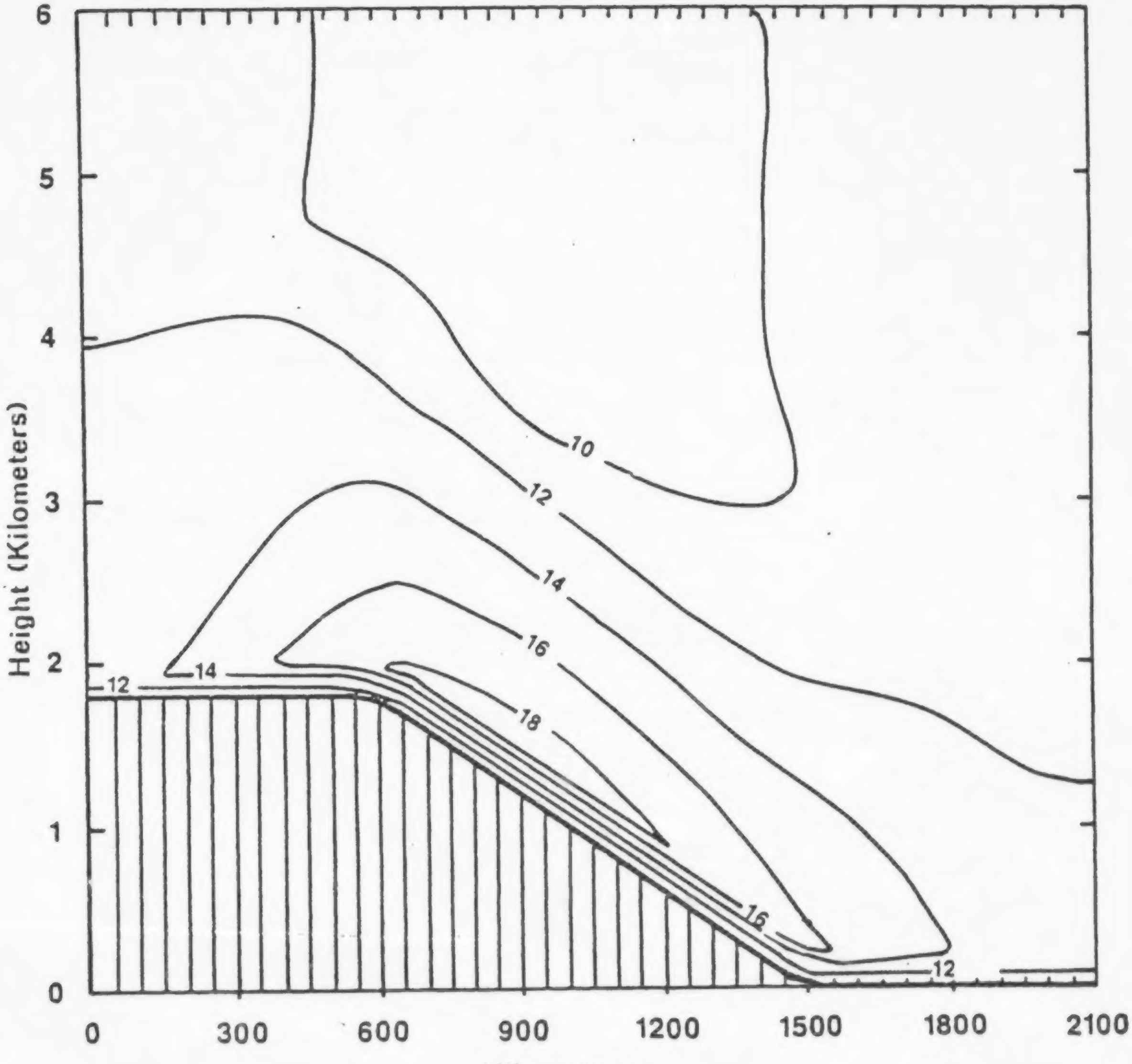
Height (Kilometers)
0
1
2
3
4
5
6
0
300
600
900
1200
1500
1800
2100
Kilometers
10
12
14
16
18
12
14
16
12

(a)

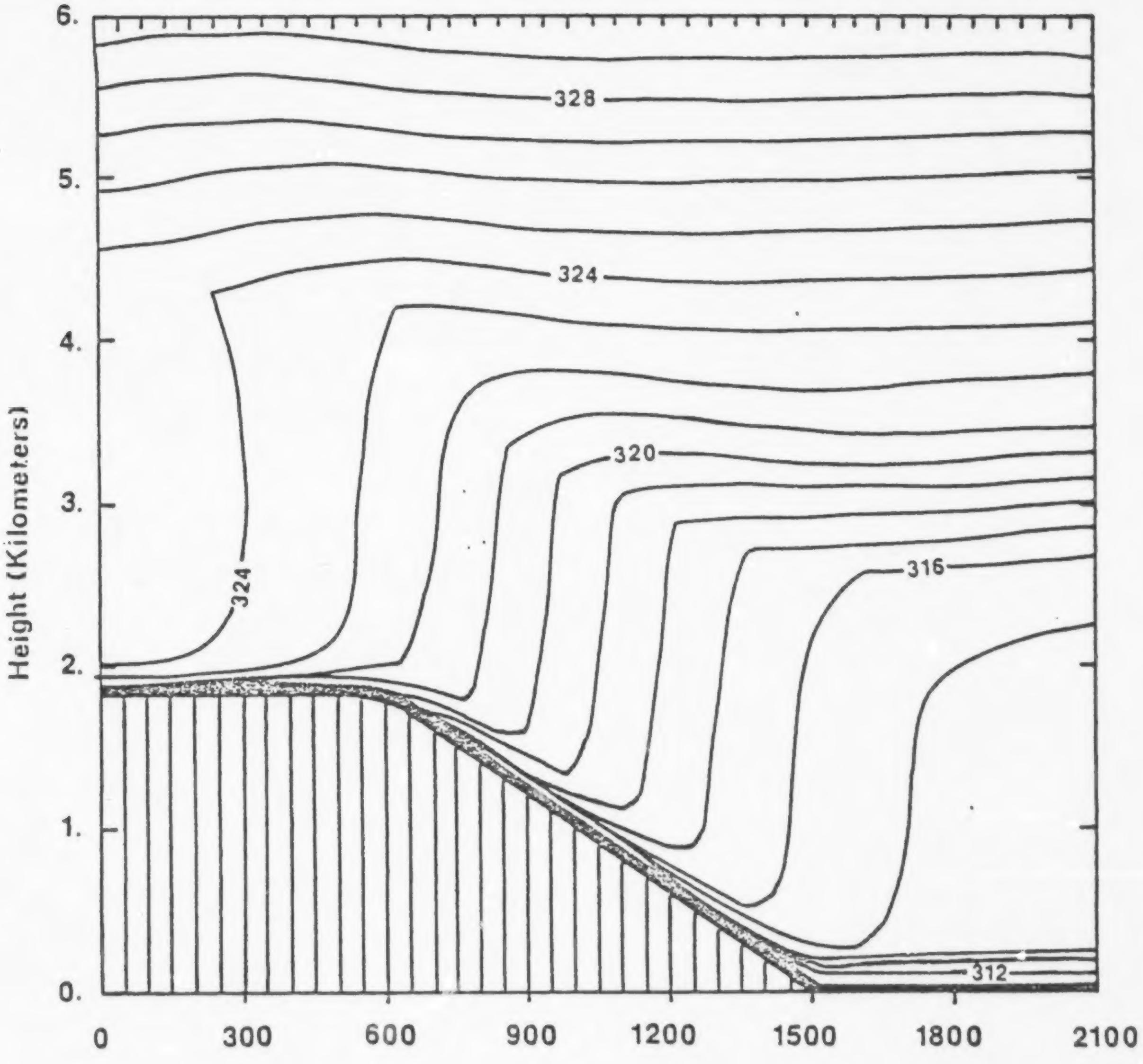
Height (Kilometers)
6.
5.
4.
3.
2.
1.
0.
0
300
600
900
1200
1500
1800
2100
Kilometers
328
324
324
320
316
312

(b)

Figure III-20 Profiles of model predicted u and v components at 1530 LST along with profiles of the total geostrophic component $V_{gt}$ for Case 2 in which terrain slope is double that of Case 1.

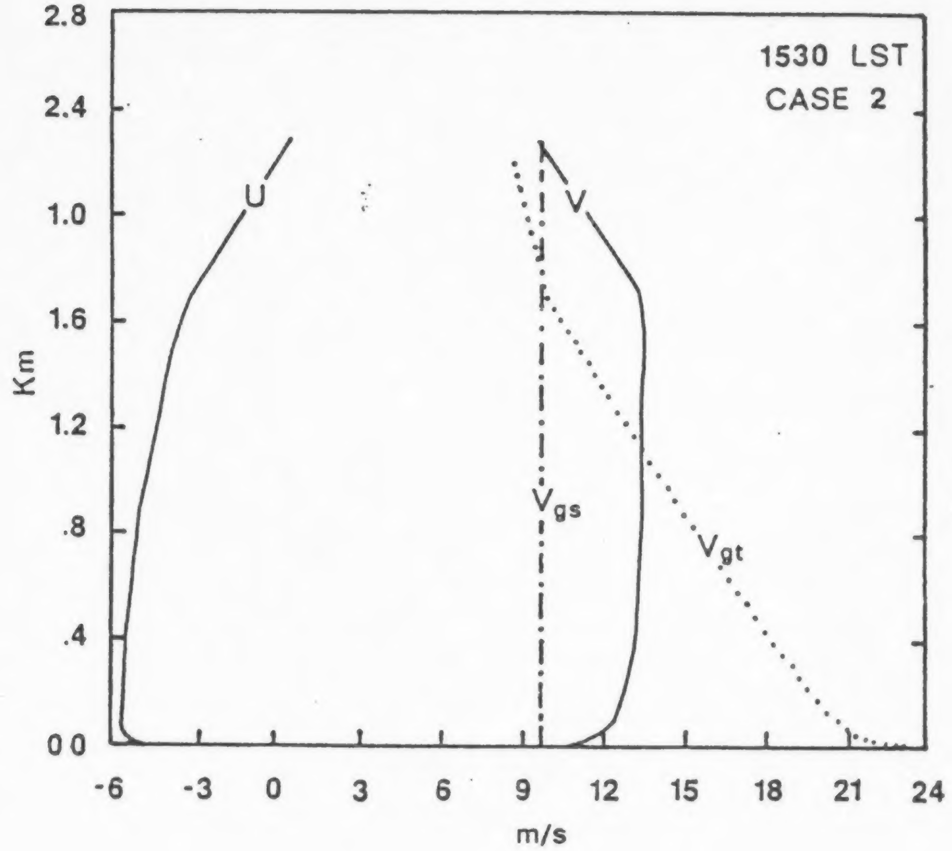
1530 LST
CASE 2
U
V
$V_{gs}$
$V_{gt}$
2.8
2.4
1.0
1.6
1.2
.8
.4
0.0
Km
-6
-3
0
3
6
9
12
15
18
21
24
m/s

Figure III-21 Same as Figure III-20 except for 2330 LST. (Case 2)

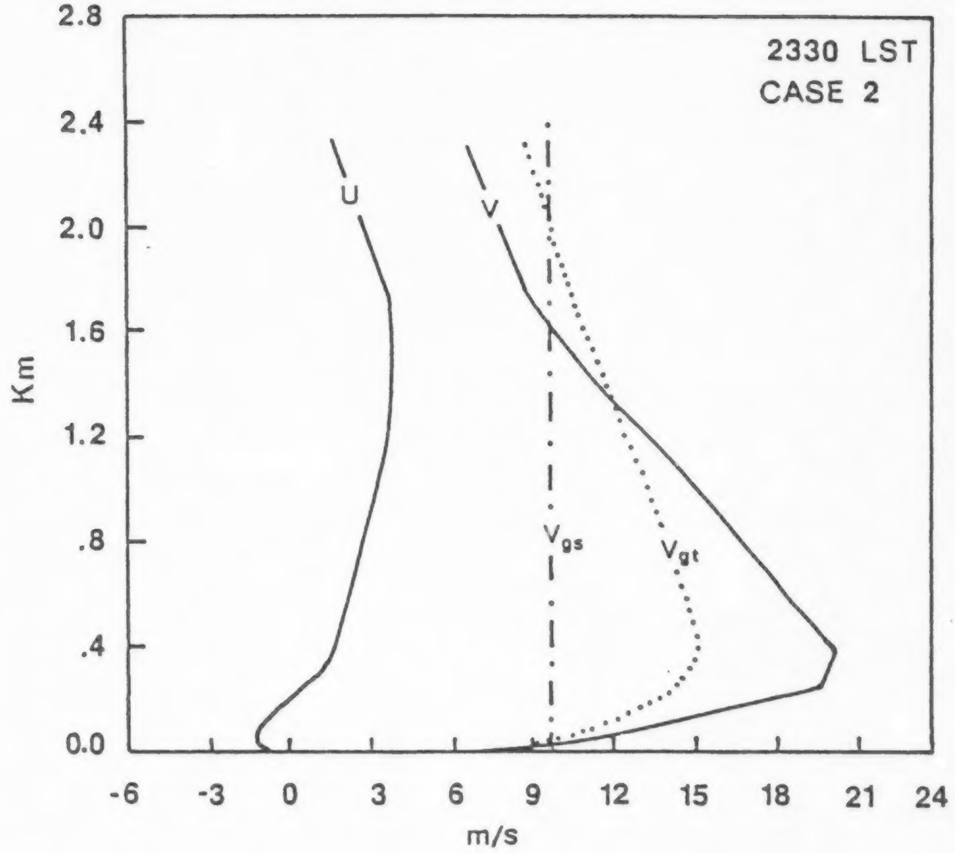
2330 LST
CASE 2
2.8
2.4
2.0
1.6
1.2
.8
.4
0.0
Km
-6
-3
0
3
6
9
12
15
18
21
24
m/s
U
V
$V_{gs}$
$V_{gt}$

Figure III-22. Same as Figure III-20 except for 0330 LST. (Case 2)

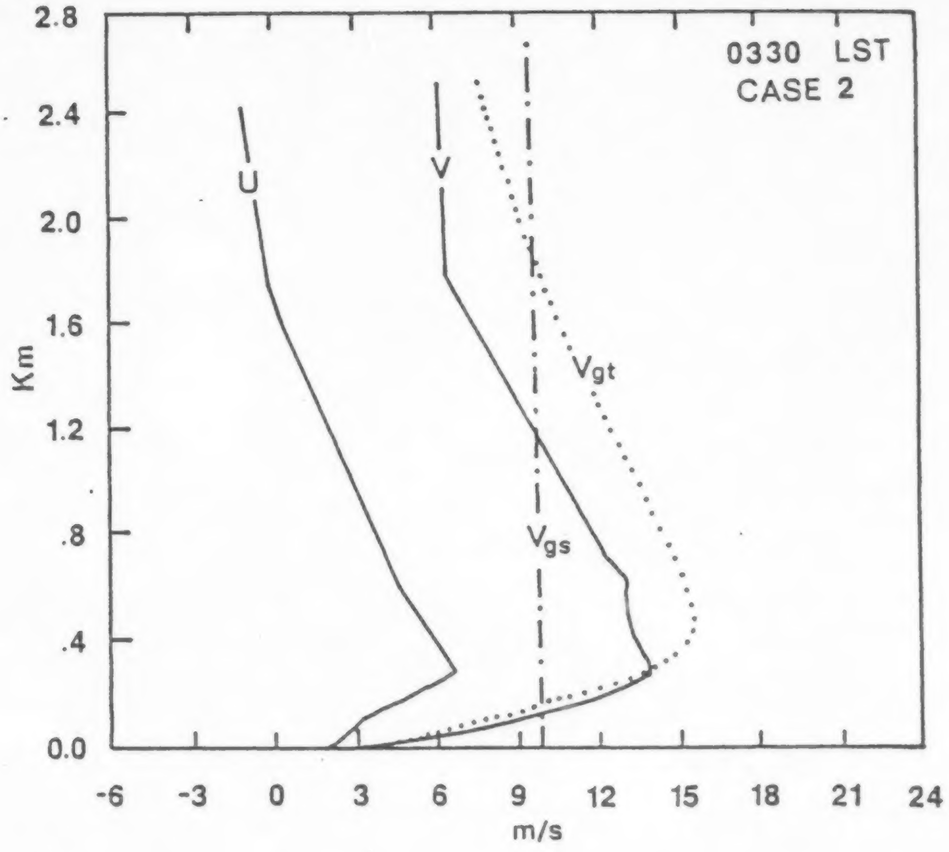
2.8
2.4
2.0
1.6
1.2
.8
.4
0.0
Km
-6
-3
0
3
6
9
12
15
18
21
24
m/s
0330 LST
CASE 2
U
V
$V_{gt}$
$V_{gs}$

In Case 3, the same slope and initial conditions were employed as in Case 1; however, the latitude was changed from 45° to 30°. Because of the longer inertial period, the maximum jet velocities occurred later. As can be seen in Figures III-23 and III-24, the pressure gradient induced by the terrain is stronger than in Case 1 and produced stronger nocturnal jets. The strength of the terrain induced pressure gradient is greater because of stronger surface heating at the lower latitude.

## Summary of Boundary Layer Formulation

As mentioned in the beginning of this chapter, turbulent exchange processes are important in slope and mountain winds. The test results presented here indicate that the local exchange coefficient formulation and radiative approximation can simulate the mean structure of the nocturnal PBL as well as existing more computationally costly, second order turbulence models with more complete radiative formulations.

Figure III-23 Profiles of model predicted u and v components at 1530 LST along with profiles of the total geostrophic component $V_{gt}$ for Case 3.

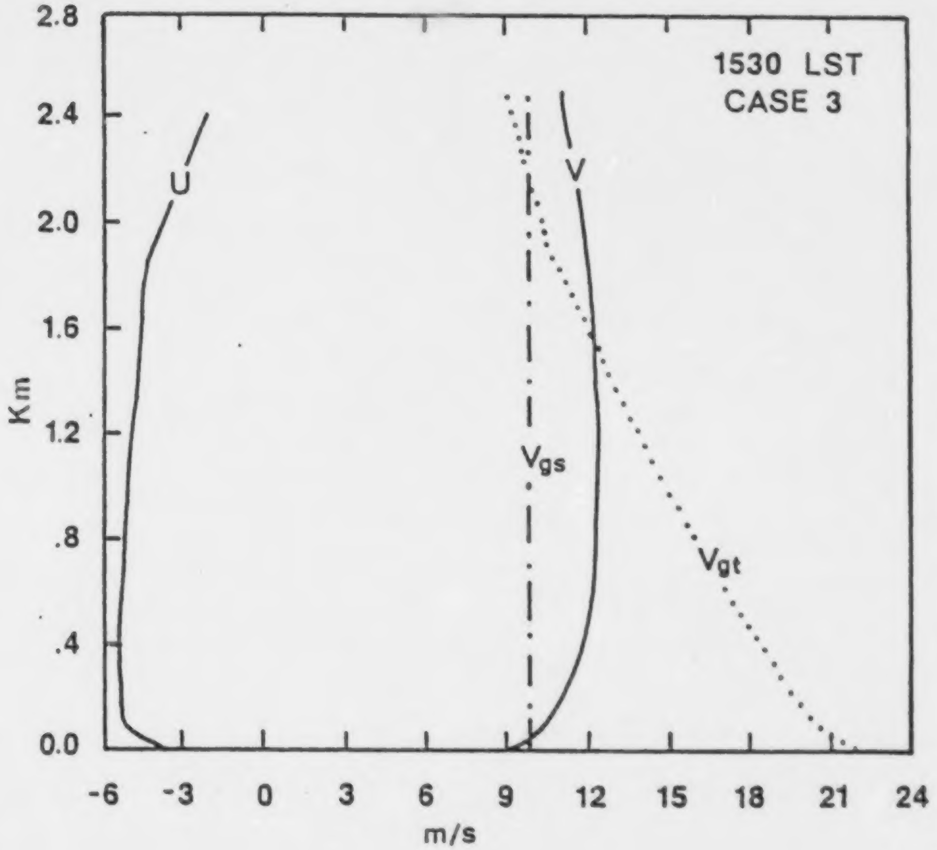
1530 LST
CASE 3
U
V
Vgs
Vgt
Km
m/s
2.8
2.4
2.0
1.6
1.2
.8
.4
0.0
-6
-3
0
3
6
9
12
15
18
21
24

Figure III-24  Same as Figure 21 except for 0130 LST. (Case 3)

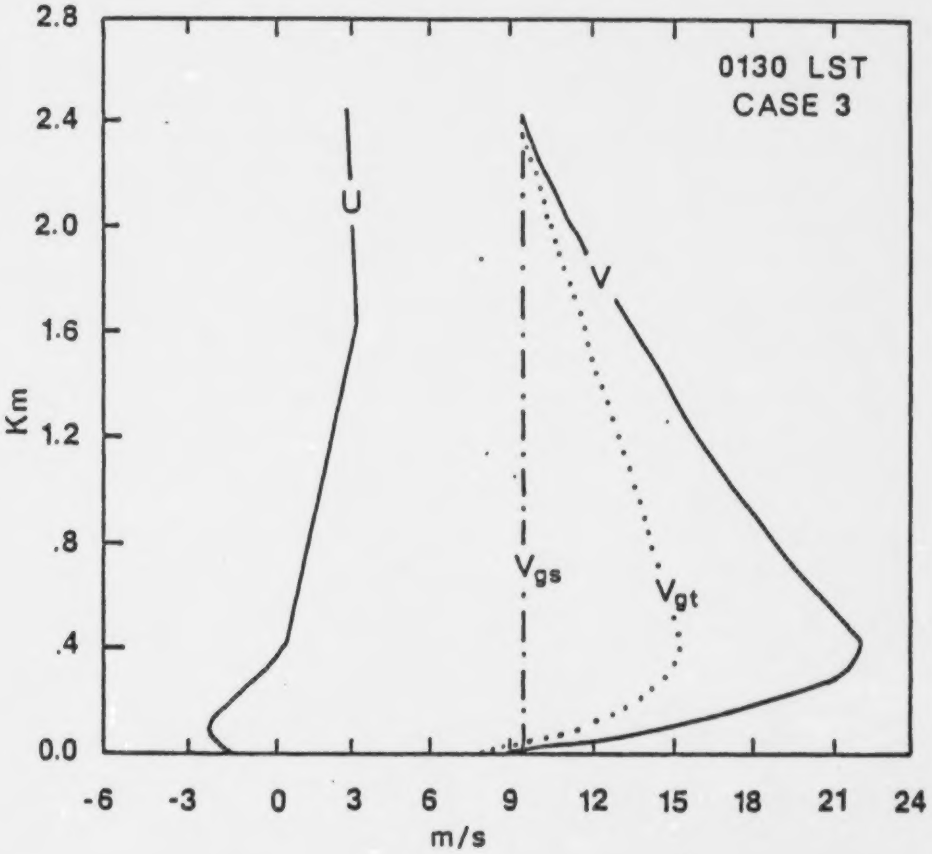
0130 LST
CASE 3
U
V
Vgs
Vgt
Km
2.8
2.4
2.0
1.6
1.2
.8
.4
0.0
-6
-3
0
3
6
9
12
15
18
21
24
m/s

# IV. HISTORICAL OVERVIEW OF MOUNTAIN-VALLEY CIRCULATIONS

Before beginning discussion of the modeled circulations, it is appropriate to provide an historical perspective on the description and theories of mountain-valley circulations.

## Descriptive Models

Much of the early ideas and conceptual models of topographic circulations were rooted in observations taken in European valleys. Defant (1951) provided an excellent description of this work, including the characteristics of slope and mountain-valley flows and the importance of the slope flow in driving the mountain-valley circulations. Defant (actually following Wagner (1938)) attributed the slope flow, as one might expect, to the difference in temperature over the inclined slopes and the air at the same altitude over the center of the valley. This produces upslope flow during the day and downslope flow at night. These slope flows are relatively shallow, especially the nocturnal downslope flow, and because they are limited to the valley walls would probably not be a conspicuous feature. However, the mountain-valley flow is much deeper extending from the valley floor to near the ridge crests of the valley walls. The physical mechanism producing the valley flow, put forward by Defant and Wagner, is the establishment of a pressure gradient between the valley and the plains outside the valley. The pressure gradient is introduced by the slope winds which gradually fill the valley with cooler (or warmer) air through a greater depth than on the plains. Thus, a deeper flow in the valley is established whose physical generation is less direct then the slope flows. Observations in some of the larger European valleys and more recently the work of Whiteman and McKee (1979), show both the shallow slope flows and the deeper flows along the axis of the valley.

A major consequence of this theory is that the slope of the valley floor is of little consequence to the direction of the along valley component. The most important features determining the direction of the mountain-valley flow are the direction of the valley opening onto a plain, the slopes of the ridgetops, and the direction of the widening or narrowing of the valley. The influence of the these features on mountain-valley winds are explored in a lively audience discussion contained in a paper by Davidson and Rao (1963).

## Analytical Models

Because of the complex three-dimensional nature of mountain-valley circulations most of the analytical work has been confined to a description of the slope flows. One of the earliest and most successful analytical studies of the slope winds was carried out by Prandtl (1949; see Sutton (1953) or Rao and Snodgrass (1979)). Prandtl, incorporating frictional stress in the form of a constant turbulent exchange coefficient and assuming a steady state, found analytical solutions for the velocity and temperature profiles above the slope as a function of an arbitrary length scale, l. Thus, for a given l and an assumption on the ratio of the turbulent exchange coefficients for heat and momentum, the profile of the slope wind could be computed. Sutton (1953) demonstrated good agreement between Prandtl's analytic solution with observations made by Defant on steep slopes and Tyson (1967) also found similarity even in flows that would have to be characterized as mountain flows rather than pure slope flows.

Other investigators have made extensions of Prandtl's work such as Lykosov and Gutman (1972), who considered the case of an external ambient wind. More recently Manins and Sawford (1979a) presented a hydraulic model in which vertical details are eliminated by a layer average; but, entrainment into the downslope flow with distance is considered. With this model, for steady conditions, they found the thickness of the slope flow to grow linearly with distance downslope. Briggs (1980) using similiar methods, addressed the slope flows in the context of a turbulent entraining jet. Also, neglecting the vertical details, Briggs examined the characteristic velocity and depth of the slope flow in terms of slope angle, bulk Richardson number and entrainment coefficients.

Time dependent analytical solutions for the slope wind have also been attempted by various authors. Defant (1951) in a crude approximation extended Prandtl's solution to include the diurnal oscillation of the slope wind. In more detail, Fleagle (1950) used layer-averaged equations to examine interesting surges which appeared in observed downslope flows. Fleagle in his analysis found that inclusion of the effects of compressibility through adiabatic warming lead to an oscillatory solution in the downslope flow. The oscillation is due to adiabatic warming of the downward moving air occurring faster than the radiational cooling of the layer, producing what has been referred to as katabatic overshoot. Petkovsek and Hocevar (1971) also considered time dependent solutions with compressional warming but in a fashion so their solutions do not include an oscillatory behavior. A detailed investigation of the time dependent solutions using a linearized version of the mesoscale model equations is given in a later section.

## Numerical Models

Only in recent years have computer technology and numerical knowledge progressed to the point where numerical simulation of three-dimensional mountain-valley flows is possible. Perhaps the most courageous attempt at numerical simulation of these circulations was that of N. H. Thyer in his dissertation in 1962 and also reported later (Thyer (1966). Thyer, trying to model particularly steepwalled valleys, encountered innumerable numerical stability problems in several model formulations. He achieved his most success employing a three-dimensional vorticity equation; but, was only able to integrate the model for 120 seconds of model time. Although his solutions did produce an along-the-valley axis component, the results would appear questionable given the short time period of the simulation.

More recently Mahrer and Pielke (1977) simulated large scale two-dimensional upslope and downslope winds using the same basic hydrostatic primitive equation model employed in the present investigation. Their study, however, was primarily a simulation study and did not address the details of the physics of the slope flows.

Several investigators have undertaken numerical studies of slope winds using a one-dimensional model (vertical resolution only). This is accomplished by rotating the x-directed equation of motion parallel to the slope producing a buoyancy term acting parallel to the slope. Since the vertical structure is retained, Brost and Wyngaard (1978), Lykosov and Gutman (1972) and Rao and Snodgrass (1979) have used this approach to examine the effect of the slope flow on the evolution of the boundary layer variables.

### Laboratory Models

The classic work in this area would have to be that of Ellison and Turner (1959). In their experiment they employed a long tank filled with water which could be tilted to any angle. After selecting an angle, they introduced relatively denser salt water at the top of the tank and let it flow downward through the fresh water. By dyeing the salt-water they were able to measure the flow and the depth of the downward flowing current, thus deducing characteristic velocities and entrainment rates. Briggs (1979) provides an excellent summary of their work along with his analytical treatment mentioned earlier.

Recently Peterson et al. (1980) attempted a more complex laboratory experiment using two-dimensional topography. Employing an aluminum mock-up of the topography, they cooled the aluminum surface from beneath using dry ice and produced interesting drainage flows. Although their modeled flows appeared realistic, complete similarity in the characteristic scales for such a model and the real atmosphere is impossible to attain.

## Field Observations

Because mountain-valley flows are common and reoccurring features in complex terrain, numerous observational studies have appeared in the literature. The number of experiments precludes a complete discussion. Defant (1951) provides a good overview of the early European experiments. Major studies in the U.S. have been those of Davidson and Rao (1963) in Vermont valleys; Buettner and Thyer (1965) in the Washington Cascades and more recently Whiteman and McKee (1977) in the Colorado Rocky Mountains. In South Africa, P. D. Tyson and colleagues have carried out numerous and continuing studies in the exceedingly complex terrain of the escarpment valleys of the region. Much of the work has been reported in South African journals, however, glimpses of the results are given in Tyson and Preston-Whytte (1972).

With the renewed interest in air pollution applications, a major field experiment sponsored by the Department of Energy has recently been started to examine details of drainage flows. Known as the ASCOT program, (Dickerson and Gudikson, 1980) it should provide comprehensive information on the flows from a wide variety of observing perspectives. The U.S. Environmental Protection Agency has also undertaken an extensive observation program in complex terrain (Holzworth (1980)); however its emphasis is plume behavior near terrain obstacles as opposed to the basic study of mountain-valley flows.

## V. SIMPLE SLOPE FLOWS

The model equations and parameterization described in chapters II and III form a very complex mathematical system. When attempting to apply this system to complicated topography configuration, the resulting solutions are many times just as complex and confusing to interpret as the real atmosphere, thereby masking the physical understanding of the process. Because of this potential complexity it is useful to simplify the model equations and geometry to examine possible characteristics of the physical system using analytical solutions. The phrase "possible characteristics" should be emphasized, since exclusions of non-linear effects or over-simplifications in the analytical solutions can neglect important factors contributing to the actual behavior of the real physical system.

In this section model equations are simplified and analytical solutions are examined for simple linear slopes. The analysis given below follows the approach of Fleagle (1950) by neglecting details of vertical structure through layer averaging in order to examine the time-dependent behavior of the slope flows.

### Simplified Equations

Begin with the u - momentum equation (II-1) with s constant given in Chapter II.[1]

$$\frac{du}{dt} = fv - fV_g - \theta\frac{\partial\pi}{\partial x} + \bar{g}\frac{z^* - s}{\bar{s}}\frac{\partial z_G}{\partial x} + \text{turbulent stress divergence} \qquad \text{V-1}$$

Neglect Coriolis terms and assume the slope is infinite so that the velocity field is uniform along the slope and the advective term is zero. Also, for flow near the surface $\frac{z^*}{\bar{s}} \ll 1$ then,

$$\frac{\partial u}{\partial t} = -\theta\frac{\partial\pi}{\partial x} - g\frac{\partial z_G}{\partial x} + \text{turbulent stress divergence} \qquad \text{V-2}$$

---

[1] The tilde notation utilized in Chapter III and Appendix A for the mesoscale component has been dropped in this section so that, e.g. $\tilde{\pi} = \pi$.

Next define

$$\theta = \theta_o + \theta'$$

where $\theta_o$ is an initial temperature distribution and $\theta'$ is a departure and begin with an initial temperature distribution which is only a function of z, i.e.

$$\theta_o = \theta_s + \gamma z$$

where $\gamma$ is a constant lapse rate and $\theta_s$ is the surface temperature. Likewise define

$$\pi = \pi_o + \pi'$$

where $\pi_o$ is the initial hydrostatic pressure distribution which is dependent upon the initial temperature distribution, i.e.

$$\frac{\partial \pi_o}{\partial z} = -g/\theta_o \qquad \text{V-3}$$

Since uniformity along the slope is assumed, $\frac{\partial \pi'}{\partial x} = 0$, from which it follows that $\frac{\partial \pi}{\partial x} = \frac{\partial \pi_o}{\partial x}$,

Then,

$$\frac{\partial u}{\partial t} = - \theta\frac{\partial \pi_o}{\partial x} - g\frac{\partial z_G}{\partial x} + F \qquad \text{V-4}$$

where F is taken to be the turbulent stress divergence.

When $\left| \frac{\partial z^*}{\partial x} \right| \ll 1$ the coordinate transformation from a z system to the terrain following ($z^*$) system yields

$$\left.\frac{\partial \pi_o}{\partial x}\right|_{z^*} = \left.\frac{\partial \pi_o}{\partial x}\right|_{z} + \frac{\partial \pi_o}{\partial z}\frac{\partial z}{\partial x} \qquad \text{V-5}$$

where $\partial z/\partial x$ is the slope of the z* surface (see Pielke and Martin (1980) for a discussion of the validity of this transformation procedure). Near the surface, the slope of a z* coordinate surface is approximately the same as the slope of the topography i.e. $\left.\frac{\partial z}{\partial x}\right|_{z^*} = \frac{\partial z_G}{\partial x}$ . Using this fact and that $\left.\frac{\partial \pi_o}{\partial x}\right|_{z} = 0$ then,

$$\left.\frac{\partial \pi_o}{\partial x}\right|_{z^*} = -\frac{g}{\theta_o}\frac{\partial z_G}{\partial x}$$

Substituting this expression into V-4 above produces

$$\frac{\partial u}{\partial t} = g\frac{\partial z_G}{\partial x}\left(\frac{\theta - \theta_o}{\theta_o}\right) + F$$

This equation is now (for small angles) essentially in the form utilized by Rao and Snodgrass (1980) or Fleagle (1950) and expresses the drainage induced flows as a function of temperature departure from the balanced state.

Next take the thermodynamic equation (eq. III-3) in the form

$$\frac{\partial \theta}{\partial t} = -\left.u\frac{\partial \theta}{\partial x}\right|_{z^*} + L_c \qquad \text{V-7}$$

where $L_c$ is a local cooling rate due to radiative or turbulent contributions. Since uniformity along the slope is assumed, cooling is also uniform and $\frac{\partial \theta'}{\partial x} = 0$ so that

$$\frac{\partial \theta}{\partial t} = -\left.u\frac{\partial \theta_o}{\partial x}\right|_{z^*} + L_c \, . \qquad \text{V-8}$$

Again, using the coordinate transformation in the same manner as for pressure in V-5 yields

$$\left.\frac{\partial \theta_o}{\partial x}\right|_{z^*} = \frac{\partial \theta_o}{\partial z}\left.\frac{\partial z_G}{\partial x}\right|_{z}$$

or V-9

$$\frac{\partial \theta_o}{\partial x} = \gamma\,\frac{\partial z_G}{\partial x}$$

Substituting V-9 into V-8 gives

$$\frac{\partial \theta}{\partial t} = - u \frac{\partial z_G}{\partial x} + L_c \qquad \text{V-10}$$

In order to eliminate vertical dependence in the drainage flow problem, assume that all cooling is confined within a layer of depth h. Correspondingly, layer average the u - momentum equation (V-6) and the thermodynamic equation (V-10) by integrating over the layer. Upon dividing by the depth of the layer this yields

$$\frac{\partial \overline{u}}{\partial t} = g\frac{\partial z_G}{\partial x} \left( \frac{\overline{\theta} - \theta_o}{\theta_o} \right) + \overline{F} \qquad \text{V-11}$$

and

$$\frac{\partial \overline{\theta}}{\partial t} = - u \frac{\partial z_G}{\partial x} + \overline{L}_c \qquad \text{V-12}$$

where the overbars indicate average quantities within the layer.

Now take $\frac{\partial}{\partial t}$ of (V-11) and substitute for $\frac{\partial \overline{\theta}}{\partial t}$ from V-12 to produce

$$\frac{\partial^2 \overline{u}}{\partial t^2} = - \frac{\overline{u} g \gamma}{\theta_o} \left( \frac{\partial z_G}{\partial x} \right)^2 + \frac{g}{\theta_o} \frac{\partial z_G}{\partial x} \overline{L}_c + \frac{\partial}{\partial t} (\overline{F}) \qquad \text{V-13}$$

Equation V-13 is similar in form to the equation derived by Fleagle (1950); however, it is more general in that it contains the ambient lapse rate. In the following two sections we derive and examine analytical solutions to V-13. First friction, is ignored and a simple solution is obtained which allows insight into the role of the various parameters. Second, a more complete solution is found including friction for comparison with the numrical model solutions.

## Neglecting Friction

Since we assumed uniformity in the velocity field, $\overline{u}$ is only a function of time and equation V-13 is an ordinary differential equation for $\overline{u}$. For now neglect the time tendency of the frictional term, then the differential equation is of the form

$$\frac{d^2\overline{u}}{dt^2} + \beta^2\,\overline{u} = L_c \qquad \text{V-14}$$

where $\beta^2 = \frac{g\gamma}{\theta_o}\left(\frac{\partial z_G}{\partial x}\right)^2$ and $\alpha = \frac{g}{\theta_o}\,\frac{\partial z_G}{\partial x}$.

Starting at rest the initial conditions are

$$\overline{u}\,(0) = 0 \qquad \text{V-15}$$

$$\frac{\partial\overline{u}}{\partial t}\,(0) = 0.$$

Equation V-14 has a general solution of the form

$$\overline{u} = Ae^{i\beta t} + Be^{-i\beta t} + \frac{\alpha}{\beta^2}\,\overline{L}_c \qquad \text{V-15}$$

Using the initial conditions in (V-15) the complete solution is

$$\overline{u} = -\frac{\alpha}{\beta^2}\,\overline{L}_c\,\frac{(e^{i\beta t} + e^{-i\beta t})}{2} + 1$$

or, in trigonometric form substituting for $\alpha$ and $\beta$.

$$\overline{u} = \frac{\overline{L}_c}{\gamma\frac{\partial z_G}{\partial x}}\,(1 - \cos\beta t) \qquad \text{V-16}$$

Thus, $\overline{u}$ has an oscillatory solution about $.5\,\overline{L}_c/(\gamma\frac{\partial Z_G}{\partial x})$ with a period $\tau$, given by

$$\tau = \frac{2\pi}{\beta} = 2\pi\Big/\left[\frac{g}{\theta_o}\left(\frac{\partial z_G}{\partial x}\right)^2\gamma\right]^{1/2}$$

In examining the solution we see that the mean velocity in time is directly proportional to the cooling rate and inversely proportional to the stratification and slope. Likewise for the length of the period. Table V-1 gives periods and mean values for the velocity for several combinations of parameters.

Table V-1 Periods and mean velocities from equation V-16. The symbol $\bar{\bar{u}}$ denotes a time average of $\bar{u}$.

| $L_c$ (Deg/hr) | $\frac{\partial z_G}{\partial x}$ | (Deg/Km) | Period (s) $\tau$ | $\bar{\bar{u}}$ (m/s) |
|---|---|---|---|---|
| .5 | .25 | 2 | 3107 | .14 |
| .5 | .25 | 8 | 1553 | .04 |
| .5 | .50 | 4 | 1098 | .04 |
| .5 | .25 | .5 | 6215 | 1.1 |

The basis of the oscillatory nature of the solution is essentially that put forward by Fleagle (1950). Fleagle pointed out that as the flow begins to develop, the adiabatic warming counteracts the local cooling thus slowing, in fact, reversing the acceleration of the downslope flow. The present solution differs from that of Fleagle (1950) in that it contains the ambient lapse rate.[1] Because the gradient of the potential temperature along the slope is directly proportional to the vertical lapse rate it can easily be seen in equation V-8 or V-12 that the rate of advective or adiabatic warming is directly related to the gradient of potential temperature along the slope.

The inclusion of the lapse rate as a component of the solution is important in that it essentially defines the parameter space in which resolveable oscillations will occur and indicates the importance of the stratification in limiting the strength of the drainage flow. For example, in an initial well-mixed (adiabatic) atmosphere where there is little or no gradient along the slope, the present solution would indicate periods of oscillation so long that they could not be resolved in overnight observations. Further discussion of the solutions will be given in the next section.

## Including Friction

Returning to equation (V-13), the simplest representation for the turbulent stress divergence is that it is proportional to speed (Fleagle 1950), i.e.

$$\overline{F} = - k\overline{u}.$$

---

[1] Fleagle, deriving the basic differential equation from a more heuristic point of view considered in effect only the case of an isothermal atmosphere.

Using this in equation (V-13) gives

$$\frac{d^2\overline{u}}{dt^2} + \frac{g}{\theta_o}\left(\frac{\partial z_G}{\partial x}\right)^2 \gamma\,\overline{u} = \frac{g}{\theta_o}\frac{\partial z_G}{\partial x}\overline{L}_c - k\frac{d\overline{u}}{dt} \qquad \text{V-17}$$

or using the notation adopted earlier

$$\frac{d^2\overline{u}}{dt^2} + k\frac{d\overline{u}}{dt} + \beta^2\,\overline{u} = \overline{L}_c \qquad \text{V-18}$$

This is formally the same differential equation developed by Fleagle except the coefficients contain the ambient lapse rate. This equation is essentially the non-homogeneous equivalent to the classic problem of a mass on a spring with a damping coefficient k. If $k^2 > 4\beta^2$ then the solution corresponds to overdamped motion (see Boas (1966)). In the drainage flow problem, however, (except for small slopes and near adiabatic conditions) $k^2$ is generally less than $^2$ so that the solution corresponds to underdamped or oscillatory motion. This underdamped solution is given by

$$\overline{u} = Ae^{-\frac{1}{2}kt}\cos\left(\omega_o t - B\right) + \frac{\alpha}{\beta^2}\overline{L}_c \qquad \text{V-19}$$

where

$$\omega_o = \left[\frac{g}{\theta_o}\left(\frac{\partial z_G}{\partial x}\right)^2 \gamma - \frac{1}{4}k^2\right]^{\frac{1}{2}} \qquad \text{V-20}$$

and A and B are constants to be determined by the initial conditions.

Using the initial conditions given in V-15

$$A = -\alpha L_c/\beta^2 \cos(\tan^{-1}(-\tfrac{1}{2}k/\omega_o))$$

and

$$B = -\tan^{-1}(-\tfrac{1}{2}k/\omega_o)$$

or using a trigonometric relationship

$$A = -\alpha L_c(k^2 + 4\omega^2_o)^{\frac{1}{2}}/2\beta^2\omega_o$$

The final solution is then

$$\overline{u} = L_c \left[ 1 - (k^2 + 4\omega_o{}^2)^{\frac{1}{2}} e^{-\frac{1}{2}kt} \cos(\omega_o t - B)/2\omega_o \right] / \frac{\partial z}{\partial x} G\gamma \qquad \text{V-21}$$

This solution is similar to that obtained by Fleagle (1950) except, again, it contains the ambient lapse rate.

In examining the solution we note first that the period of the oscillation depends on the slope and ambient stratification in a similar manner to the simpler solution given in the previous section; however, the period is affected by the friction coefficient k. The mean velocity is also inversely dependent upon the slope and stratification. It is not appropriate, however, to take the solution to the extreme of small slopes or small stratifications since this would violate the condition of underdamped motion assumed for the solution.

Early observations of slope and mountain-valley flows indicated surges in the flow with periods of the order of 20 minutes, thus, Fleagle's oscillatory solution appeared to be a satisfactory explanation of the surges (Tyson (1967)). The more complete solution given here, however, indicates the restricted parameter space that exists for oscillatory behavior. For example, in a valley for a well-mixed environment (such as near sunset) equation (V-21) would not indicate the existance of surges. If fact, if surges were to appear the solutions here would indicate they would have to occur much later when a substantial stratification had developed in the valley.

As mentioned in a previous chapter Petrovsek and Hocevar (1971) also obtained an analytical solution for time drainage flows which contained stratification as a parameter. Their formulation of the differential equation is, however, different than that of Fleagle (1950) or that presented here and does not give an oscillatory solution.

## Numerical Comparisons

Using the analytical solution given in equation (V-21) as a guide to the proper parameter space, a series of simple experiments were attempted to determine if the full non-linear numerical model would exhibit the same behavior as the analytical solution. It should be emphasized that this is not to be viewed as a pure numerical test of the analytical solution employing the simplified model structure. Rather, it is to determine whether the essential characteristics of the analytical solutions are manifest in the more complex non-linear numerical model when simplified model forcing and topography are used.

A simple slope-plateau geometry (slope of .25) was used in the numerical experiments which is not as simple as the infinite slope employed in the analytical solution. Because of the non-uniformity in the topography, edge-effects limit the length of the numerical integration; however, the essential problem can be investigated with a minimum of restructuring of the numerical code. A constant initial lapse rate was imposed and the potential temperature lines were constructed from the stratification to lie along geopotential surfaces, thus intersecting the topography. Ideally, this should provide an initial balanced state between the pressure terms in the model equations (Mahrer and Pielke (1977)); however, specification of non-continuous topography near the ridge break introduces some initial imbalance in the pressure terms. R. Lee (personal communication, 1980) has indicated the imbalance is a function of stratification. This was also verified by numerical experiments in the present model.

For most real world applications with small initial stratification this initial imbalance should be quickly overwhelmed by the developing flow field. For the present problem, however, the proper stratification needed to produce the oscillatory behavior introduces imbalance accelerations which are comparable to the size accelerations expected from the analytical solutions. In order to make the comparisons with the analytical solutions a temporary measure was adopted to compute a pressure gradient residual at the initial time and use this as a constant forcing function in the model. A test with no forcing showed that this procedure reduced accelerations from the numerical imbalance to less than .05 m/s per hour. This procedure was only adopted to study the analytical solutions discussed in this chapter and is not an acceptable correction for integrations in which the stratification changes with time.

Forcing for the experiments was accomplished by direct cooling (.25 degrees/hour) of the lowest 50 meters. Downslope flows began almost immediately. Figure V-1 gives time series of model results at the lowest model level (2 m) for three stratifications. The length of the time series was limited to about 2 hours because of edge effects due to the imperfect geometry imposed in the numerical model. For comparison Figure V-2 shows a time series from the analytical solution (equation V-21) for the same stratifications.

Although the model solutions appear to have a "spin-up" period (perhaps due to the non-linear inertial terms), the numerical solutions do exhibit the same oscillatory characteristics as the analytical solutions. It can also be seen that the mean speed of the numerically predicted flows are inversely dependent upon the stratification as are the analytic solutions. Figure V-3 gives the advective warming in the numerical solutions and confirms the role of advection in slowing the net cooling rate.

Figure V-1 Time series of downslope velocity component produced by the non-linear numerical model for three stratifications.

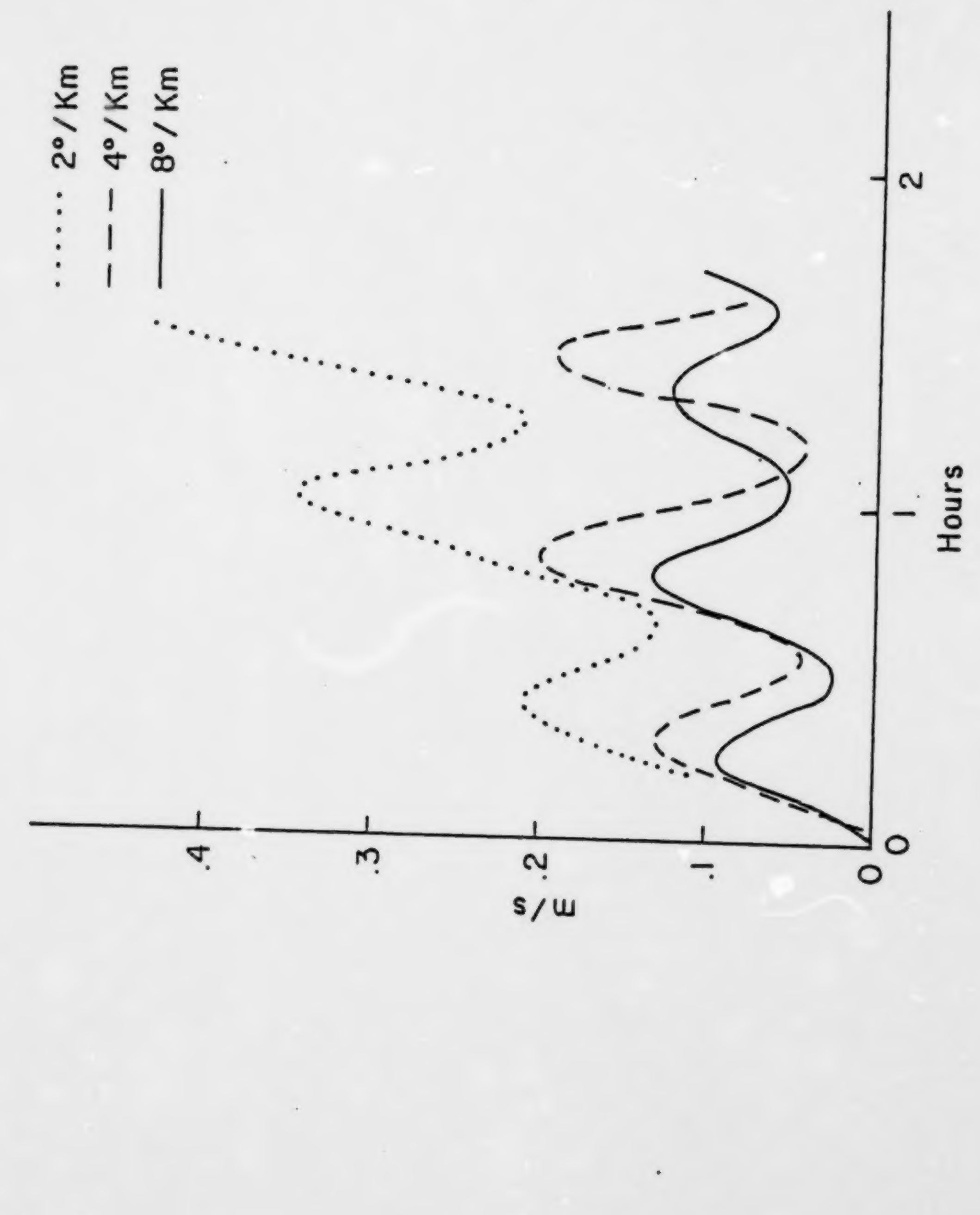
······ 2°/Km
— — 4°/Km
—— 8°/Km
m/s
.4
.3
.2
.1
0
0
1
2
Hours

Figure V-2 Time series of downslope velocity component from the analytical solution (V-21) for three stratifications.

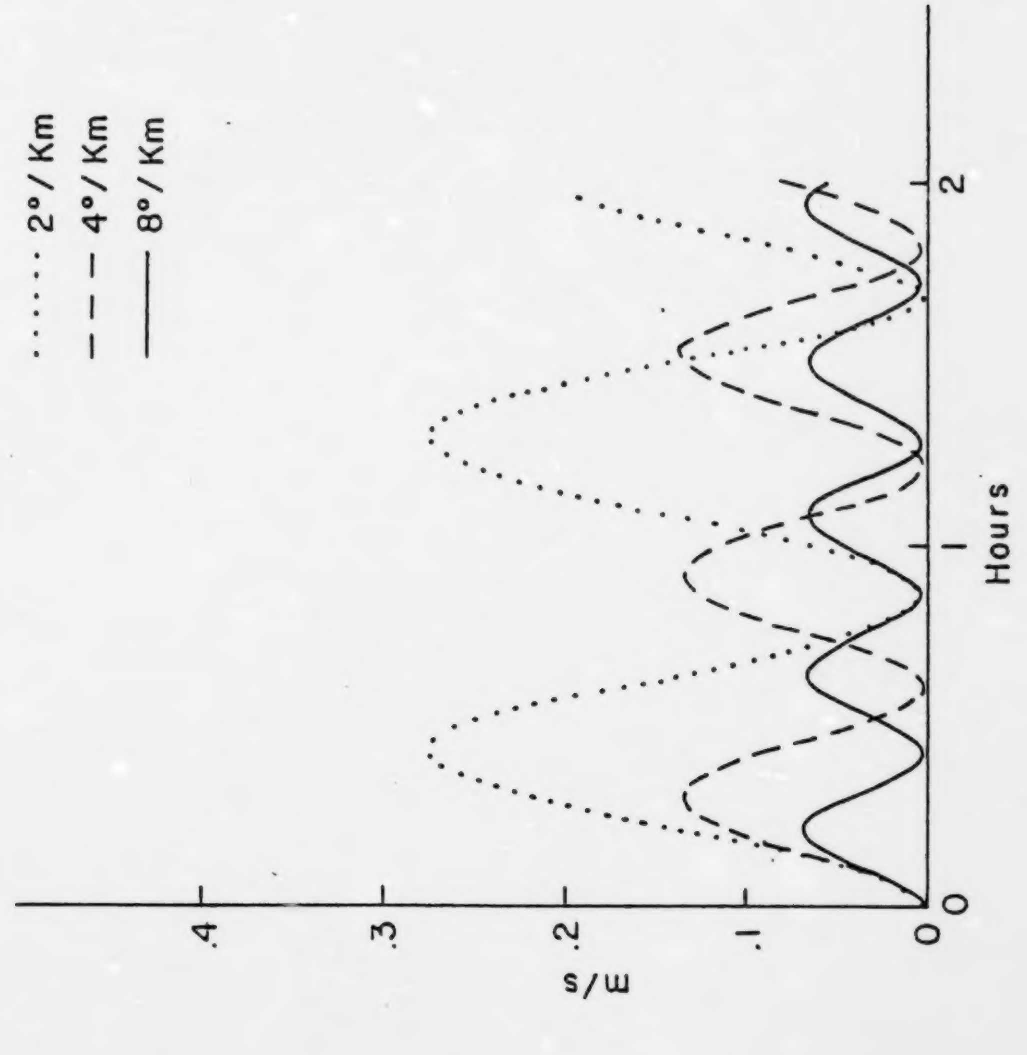
.... 2°/Km
— — 4°/Km
—— 8°/Km
m/s
0
.1
.2
.3
.4
0
1
2
Hours

Figure V-3 Advective warming in degrees per hour for the $8^{\circ}\ \mathrm{km}^{-1}$ stratification from the solution given in Figure V-1.

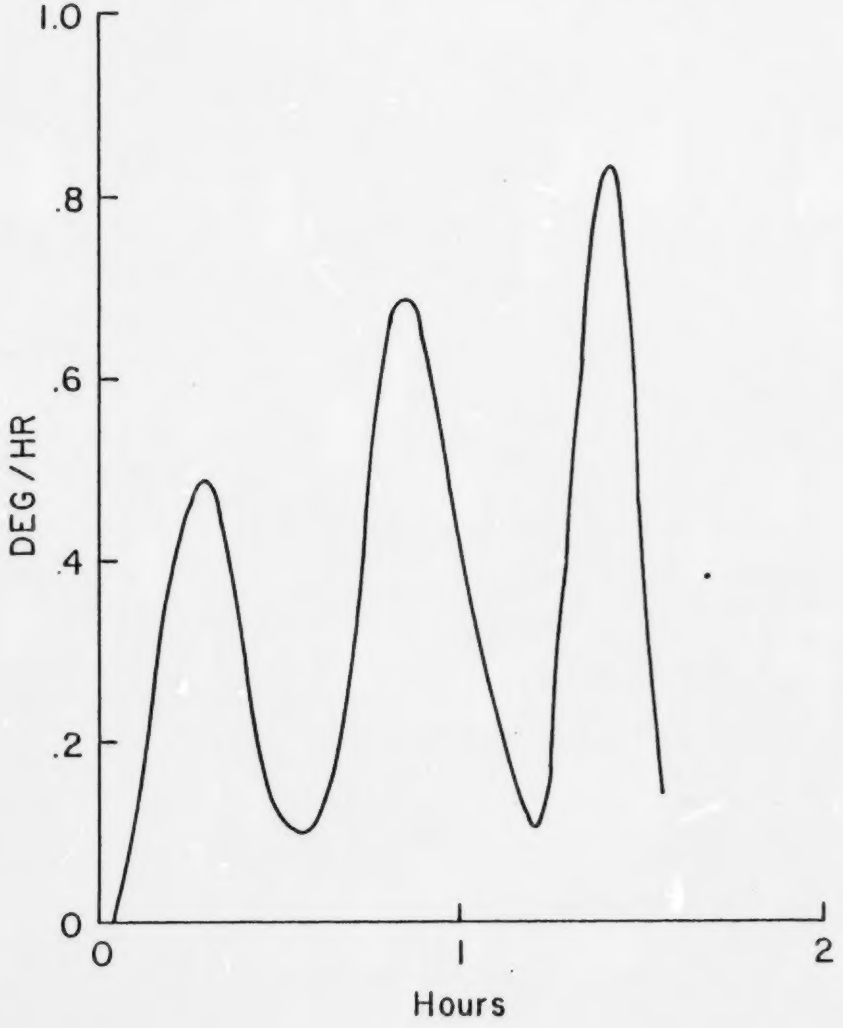
1.0
.8
.6
.4
.2
0
DEG/HR
0
1
2
Hours

One of the most important points to the solutions shown here is the extremely small magnitude (less than 50 cm/s) of the slope flows. This is primarily due the large stratifications imposed and the restrictive nature of the stratification in arresting the vertical motions. Additional runs with near adiabatic initial stratifications produced downslope flows of over 5 m/s. This dependence of the slope flow upon stratification may be an important braking mechanism for the flows in real valleys. For example, initial downslope flows into a valley would probably begin in the well-mixed environment of the late afternoon or early evening and the flows might be quite strong. Later as the valley became stably stratified the downslope flows might begin to decrease and perhaps oscillate in response to the stratification. Such a reduction in drainage speeds late at night has been noted by McNider (1977) and Hosker et al. (1980).

A major discrepancy between the analytical and numerical solutions is that the period of oscillation in the numerical solutions does not show as strong a dependence upon the stratification as the analytical solution especially for the 2° K/km lapse rate. This can be attributed to any number of factors where the numerical model system deviates from the ideal structure of the simplified equations upon which the analytical solutions are based. As examples - the stratification can dynamically change in the numerical model; return flows are present; and edge effects due to the imperfect geometry can contaminate the solutions.

A true test of the numerical and non-linear effects (and a study in its own right) would require development of a linear model and model configuration more closely aligned with that of the simplified structure of the analytical system. The present analytical study has, however, indicated the limited parameter space for which oscillatory solutions are present and the importance of the stratification in restricting the magnitude of slope flows. The simple test of the numerical system also indicates that it behaves in a similar manner to the analytical solutions for the parameters imposed.

# VI. TWO-DIMENSIONAL SLOPE FLOWS

The mesoscale model described in Chapters II and III was used to examine the development of drainage flows in an idealized two-dimensional valley. The primary purposes of the experiment was to examine the cooling occurring in the valley due to the drainage of cold air into the valley and the response of the slope flows to this cooling. The valley modeled was purposely accentuated to have a high height-to-width ratio (19 km wide, 2 km deep) with a side wall slope of .25 ( 14°). Table VI-1 gives additional details of the model run.

Although initial sensitivity studies were carried out using specified constant surface cooling rates, the cases reported here were forced by cooling produced by the surface energy budget. Soil characteristics were the same as those used in the Wangara experiment given in Chapter III. Actual surface cooling rates produced by the budget ranged from approximately .5 degrees per hour on the sidewalls to 1.5 degrees per hour in the valley center for the first few hours of integration. Later, both sidewall and valley center surface cooling rates approached .5 degrees per hour.

## Sidewall Slope Flows

The model was started at rest (1 cm/s imposed velocity) and cooling began immediately. Shallow drainage flows developed quickly on both valley walls, coverging toward the center. A slight return circulation or upslope flow also appeared above the downslope flow. This is shown in Figure VI-1 which gives the velocity profile that developed over the center of the western sloping wall along with the temperature profile (see Figure VI-2 for the shape of the valley). As can be seen, the slope flow is strong but shallow with the velocity maximum occurring at only 8 meters above the surface.

Table VI-1. Model parameters and configuration

| | |
|---|---|
| Surface roughness | 10 cm |
| Time step | 30 s |
| Latitude | 35° N |
| Horizontal grid space | 1 Km (stretched at boundaries) |
| Vertical grid levels | 2., 8., 20., 50., 100., 200., 300., 600., 1000., 2000., 3000., 4000., 6000., 9000. |
| Initial Stratification | .2° K/km |

Figure VI-1 Downslope component (solid line) and potential temperature (dashed) profiles over the western sidewall of the two-dimensional valley at 0230 LST.

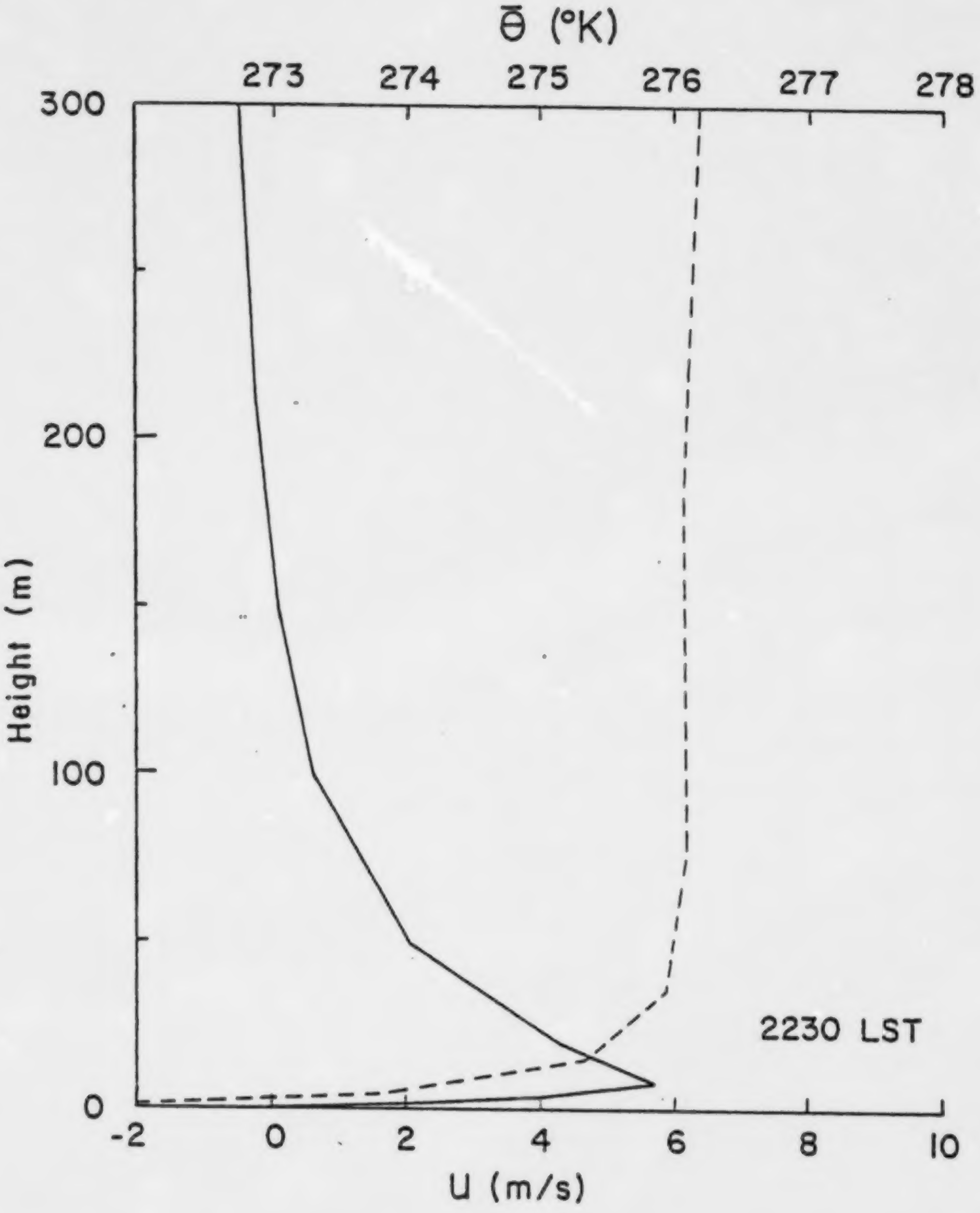
$\bar{\theta}$ (°K)
273
274
275
276
277
278
300
200
100
0
Height (m)
-2
0
2
4
6
8
10
U (m/s)
2230 LST

Observations by Defant (reported by Sutton (1953)) over extremely steep terrain showed maximum velocities at approximately 30 meters above the surface. More recent observations (Hosker et al. 1980) taken under the ASCOT program for slopes more nearly similiar to those modeled here indicated extremely shallow slope flows with maximum velocities occurring below 3 meters.

## Valley Inversion

As the sidewall slopes cool, the slope flows begin to fill the valley with the cooled air. This is graphically illustrated in Figure VI-2 which gives potential temperature contours in the valley. Initially there is only a slight stratification in the valley, while after several hours of slope flow a deep inversion has formed within the entire valley. The pooling of the cool air extends nearly to the ridge tops. This pooling of the cool air is a significant feature in the model solutions, since in Wagner's (1938) descriptive model it is the filling of the valley with the cooled air which produces the along-the-valley axis mountain wind.

The cooling pattern in the valley is quite interesting. As can be seen by the contours in Figure VI-2 the cooling within the valley does not appear to originate at the surface. Rather, the cooling occurs at essentially all heights. This is demonstrated in Figure VI-3 which gives temperature profiles over the center of the valley as a function of time. Although this shows that more cooling does occur at the surface, the entire profile within the valley is cooled with time. This cooling pattern is consistent with that observed in deep valleys in the Rockies (Whiteman and McKee (1977)).

To more closely investigate this cooling pattern, model cooling over the center of the valley was partitioned into radiational, advective and turbulent components. In the first few grid points very near the surface

Figure VI-2 Contours of potential temperature in the two-dimensional valley. a) Contours for 2030 LST, b) Contours for 0230 LST. Contour interval is 1° K. Asterisk gives location for profiles and time series in Figures VI-1 and VI-4.

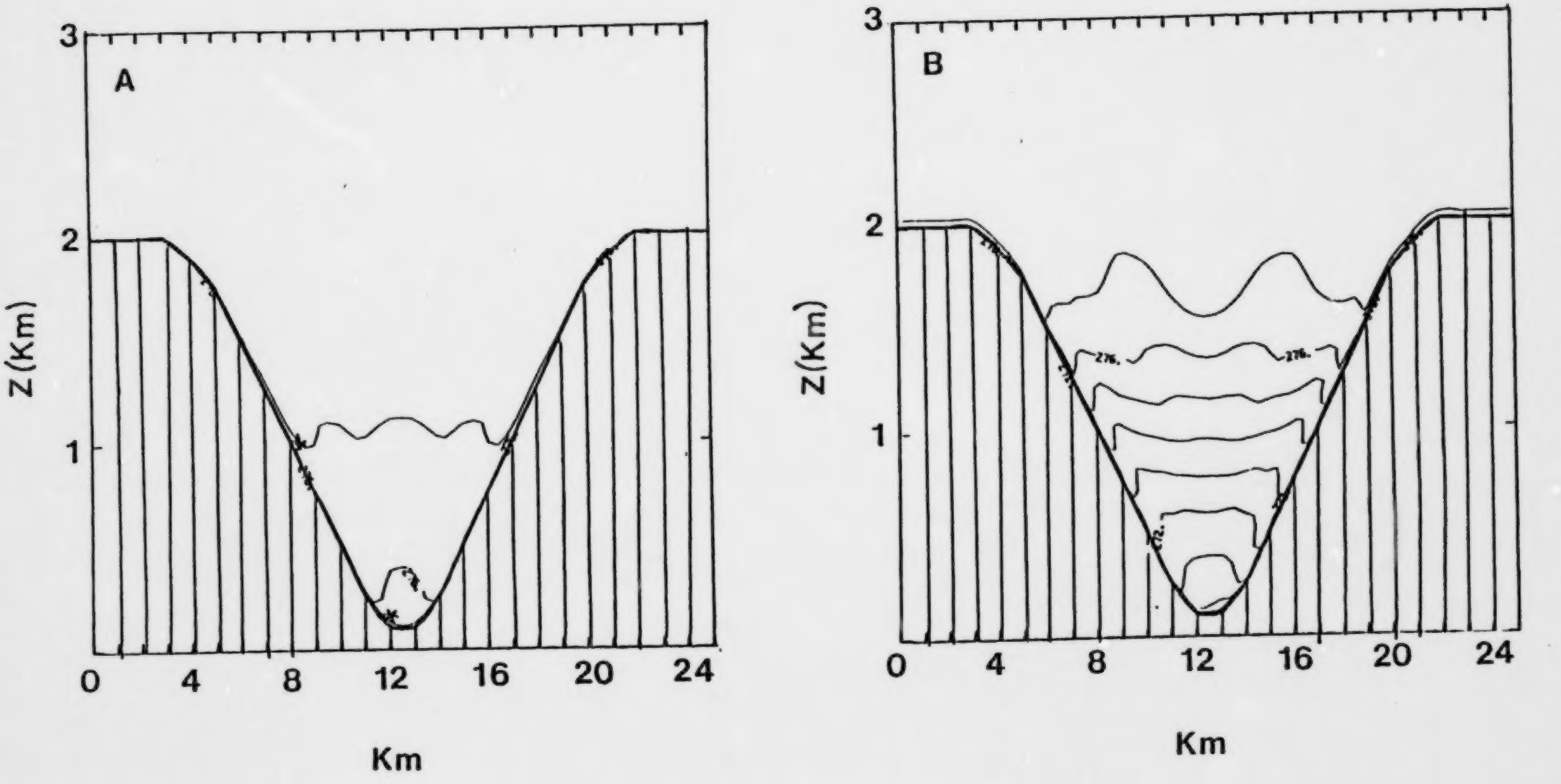
A
B
Z(Km)
3
2
1
0
4
8
12
16
20
24
Km
276.
272.

Figure VI-3 Profiles of potential temperature over the center of the two-dimensional valley for the indicated times.

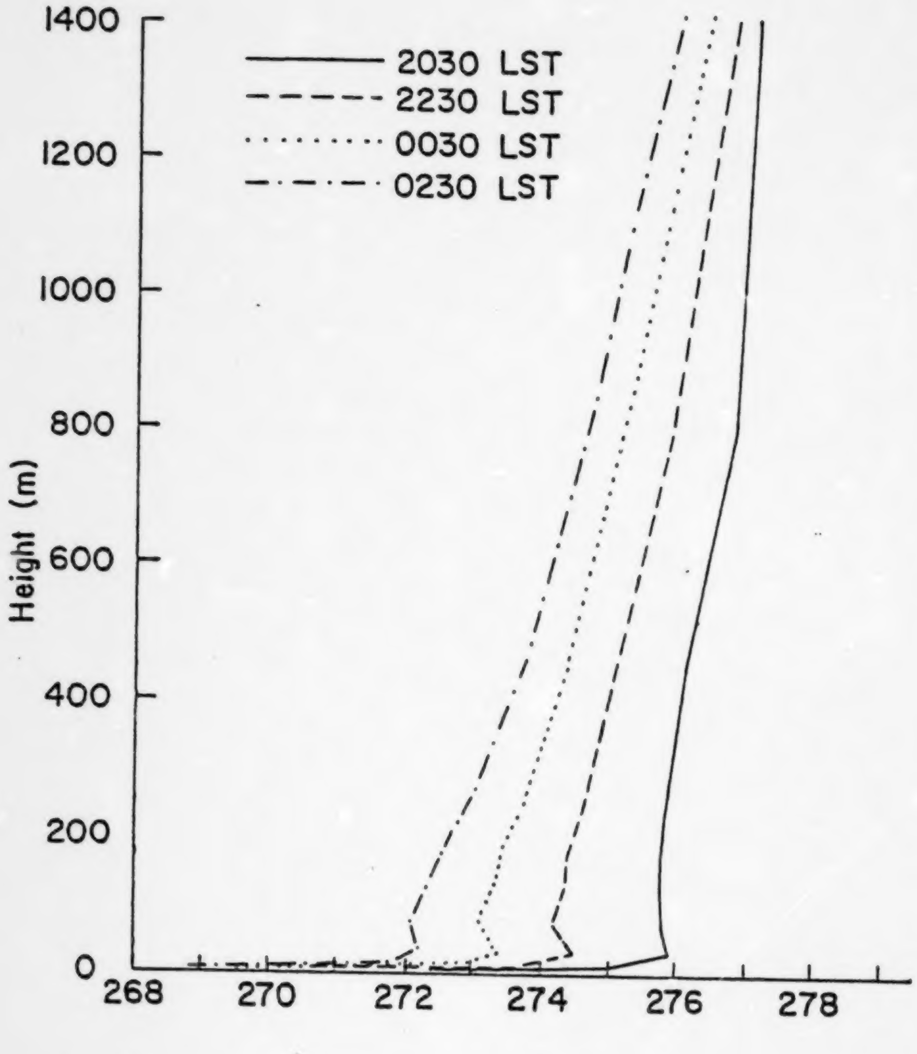
2030 LST
2230 LST
0030 LST
0230 LST
Height (m)
0
200
400
600
800
1000
1200
1400
268
270
272
274
276
278

the thermodynamic balance was extremely complicated with advection and turbulence both making substantial contributions of opposite signs. This complexity occurs in the complex zone where the drainage flows from the sidewalls are converging and may indicate that additional model vertical resolution is required near the surface. Aloft above 100 meters, the cooling as exhibited in Figure VI-3 is almost entirely due to cold air advection.

## Time Dependence of the Slope Flows

As mentioned, the slope flows developed very quickly in response to the cooling reaching a maximum velocity over the center of the slope of approximately 6 m/s after forty-five minutes of cooling. Afterwards velocities decreased through the night finally reaching a near steady state after seven hours. Figure VI-4 shows a time plot of the slope flows at two meters and 50 meters above the middle of the western slope and the along-the-valley flow over the center of the valley.

The velocities evidently decrease in part due to the increasing temperature stratification occurring in the valley. This is consistent with the analytical solutions presented in Chapter V in which the downslope velocities were found to be inversely proportional to the strength of the stratifications.

Two other factors, both related, also contribute to the decreasing velocity. First, the cooling rate over the slope begins to decrease as a balance develops between the local cooling (radiational and turbulent) and advective warming due to the developing stratification. This is illustrated in Figure VI-5 which gives the local and advective contributions to the cooling above the slope. The short-period fluctuations seen in the Figure

Figure VI-4 Time series plot of a) downslope component at two meters (dashed) and 50 meters (solid) above the western side wall and b) V component above the middle of the valley floor. Velocities plotted are three minute averages.

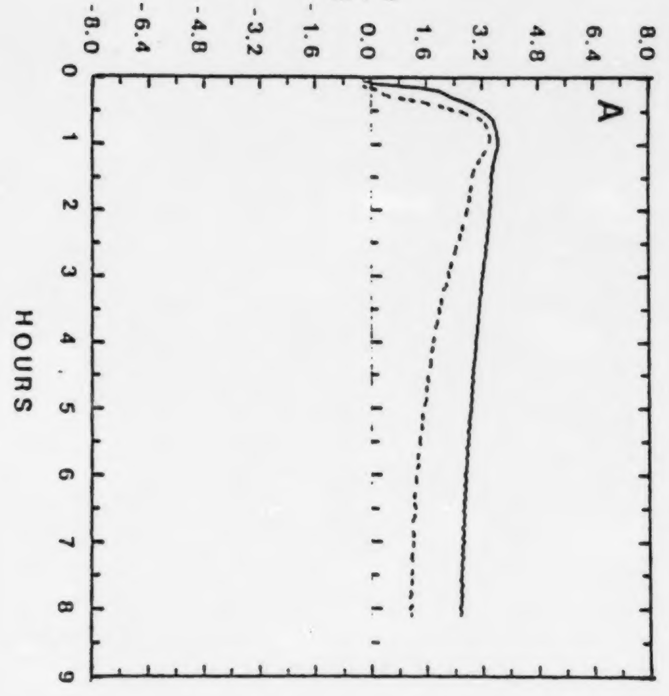
A
M / S
8.0
6.4
4.8
3.2
1.6
0.0
-1.6
-3.2
-4.8
-6.4
-8.0
HOURS
0
1
2
3
4
5
6
7
8
9

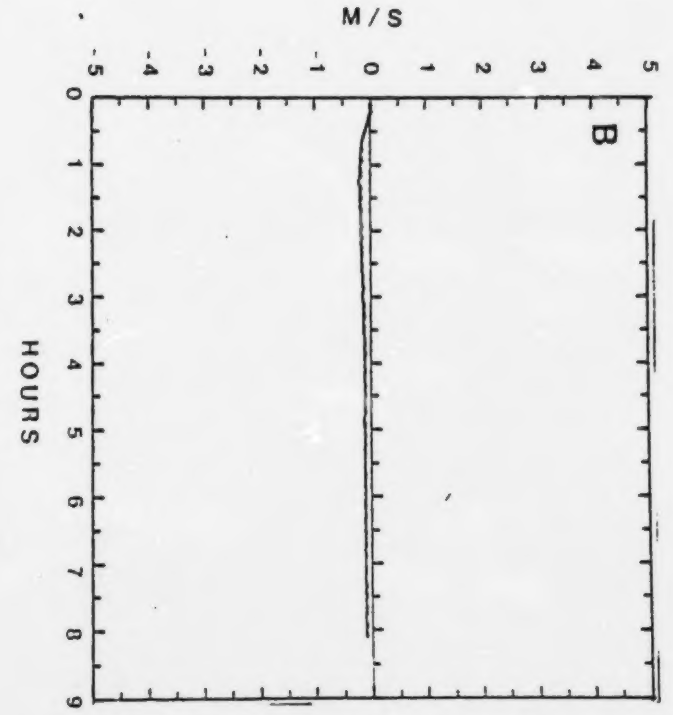
B
M / S
5
4
3
2
1
0
-1
-2
-3
-4
-5
HOURS
0
1
2
3
4
5
6
7
8
9

Figure VI-5 Time series of local warming (solid) and advective warming (dashed) over the western side wall. Warming rates are three minute averages.

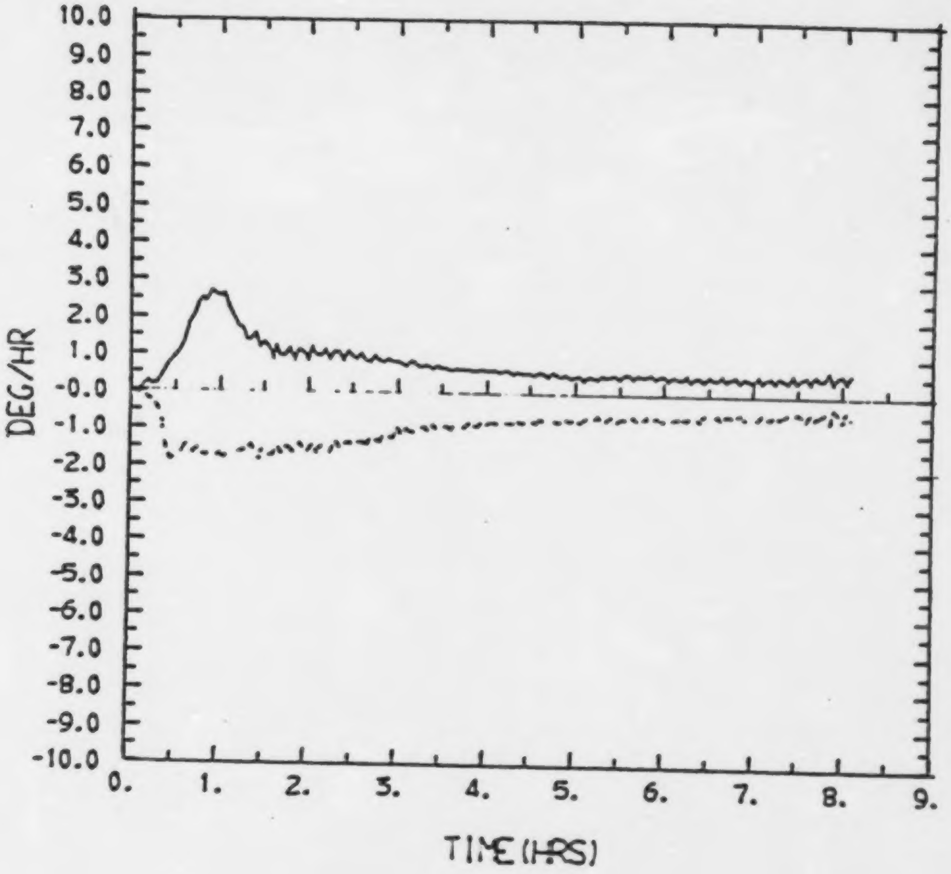
10.0
9.0
8.0
7.0
6.0
5.0
4.0
3.0
2.0
1.0
-0.0
-1.0
-2.0
-3.0
-4.0
-5.0
-6.0
-7.0
-8.0
-9.0
-10.0
DEG/HR
0.
1.
2.
3.
4.
5.
6.
7.
8.
9.
TIME(HRS)

Figure VI-6 Schematic of the deformation of the potential temperature field due to downslope and return upslope flow and resulting destabilization. a) initial field, b) after deformation by slope flow.

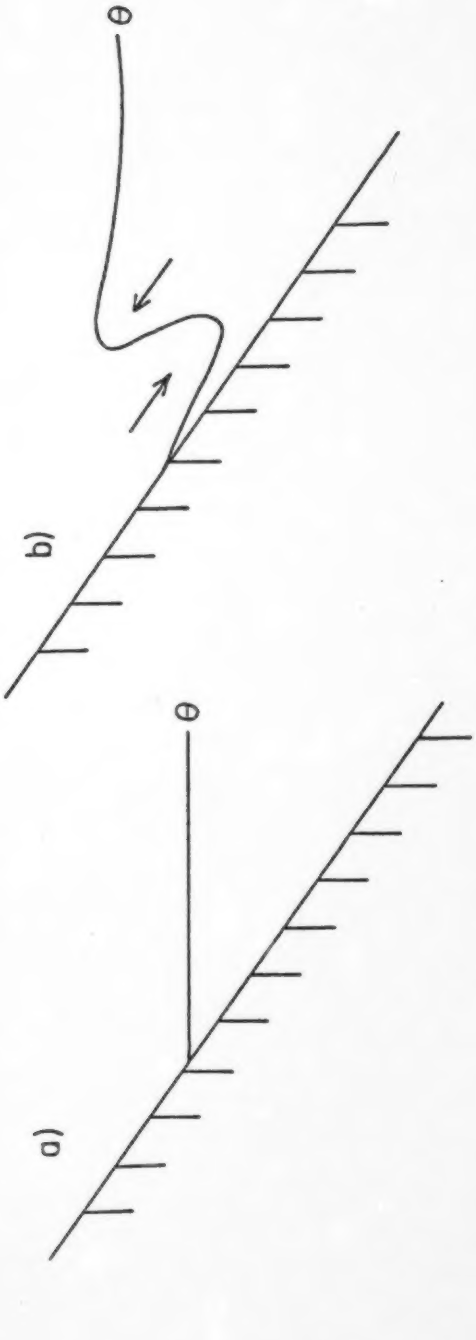
a)
θ
b)
θ

are turbulent bursts due to Richardson number instability discussed in the next section. Second, the cooling over the center of the valley, due to the pooling of cool air, reduces the horizontal temperature gradient which directly drives the slope flows.

Some slight oscillation occurs in the downslope flow as it reaches the near steady state. This oscillation, less than .2 m/s, may be due to katabatic overshoot as described in Chapter V; however, it is much smaller than the type oscillations or surges referred to in the literature (Tyson, 1967).

## Turbulent Structure

The turbulent exchange processes in the slope flows are directly linked to the developing flow field and are much more complicated than the boundary layer processes occurring over flat land. The first reason for this complexity is that the slope flow is imposed as a body force near the surface causing turbulent momentum transfer to be upward rather than downward in the upper part of the slope flows. This is contrary to normal boundary layer structure. Second, the modeled slope flows perturb the potential temperature structure destabilizing the boundary layer creating high turbulent levels aloft.

This second factor appears to have been neglected in other slope flow investigations, since a two-dimensional dynamical model is needed to exhibit this characteristic and the turbulent exchange processes must depend on local conditions. Physically the downslope flows, through advective processes, deform the potential temperature field creating a less stable profile. The upslope flow further deforms the field actually producing an unstable profile. Figure VI-6 shows schematically the deformation of the potential temperature profile over the slope. This deformation is also visible in the contours of potential temperature in Figure VI-2.

Figure VI-7 Turbulent exchange coefficient (solid) over the western valley wall showing pronounced maximum near the top of the slope flow. This profile can be compared to the profile given in Figure III-2 over a flat boundary. The dashed line gives the local gradient Richardson Number showing the unstable layer aloft created by the deformation illustrated in Figure VI-6.

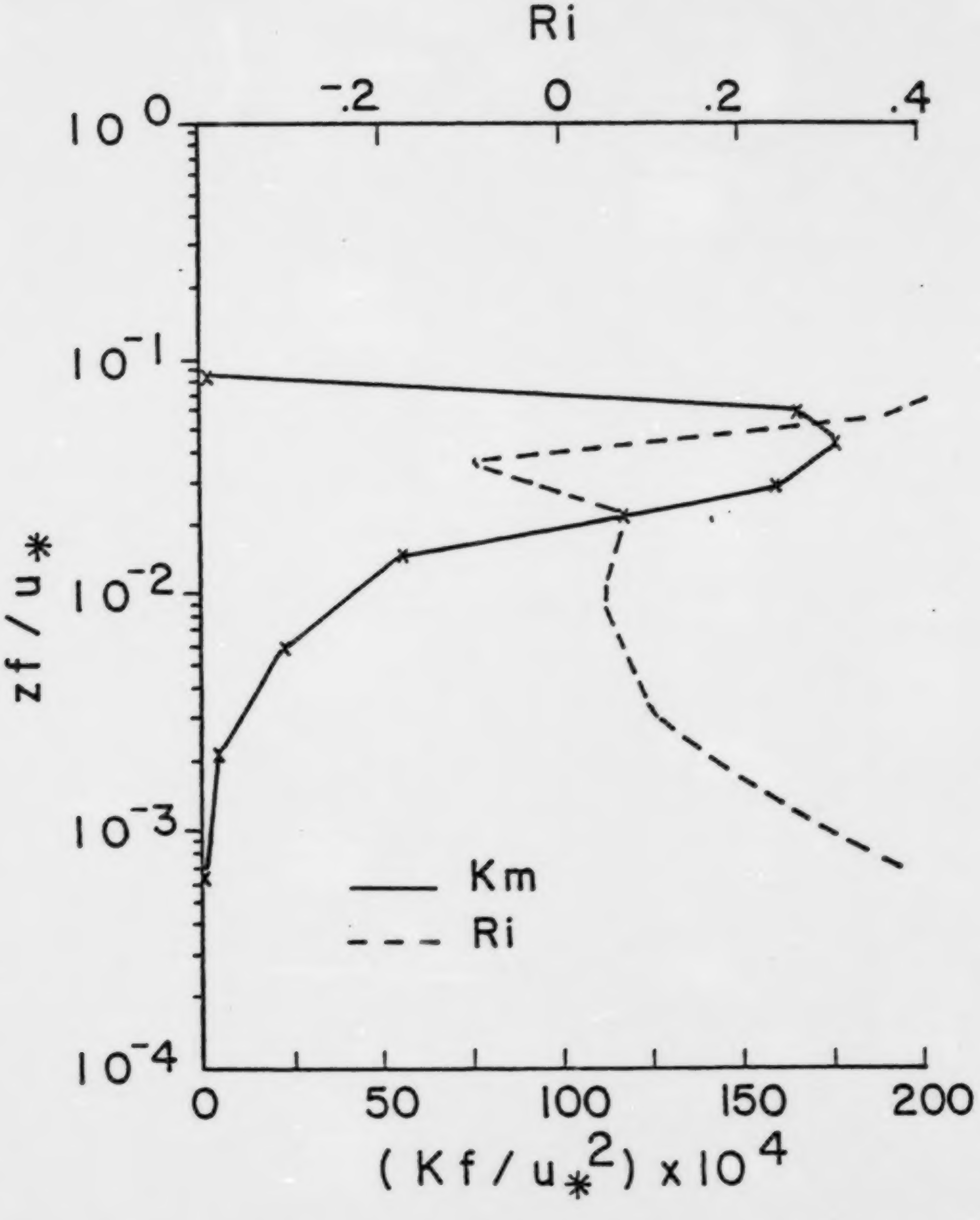
Ri
-.2
0
.2
.4
10^0
10^-1
10^-2
10^-3
10^-4
zf / u*
Km
Ri
0
50
100
150
200
( Kf / u*^2 ) x 10^4

Because turbulent exchange in the model is dependent upon the local Richardson number, the destabilized temperature profile in conjunction with wind shear between the downslope and upslope flows produces a highly turbulent region aloft. Figure VI-7 gives the turbulent exchange coefficient over the slope along with the local gradient Richardson number. In the face of the flow field continually destablizing the temperature profile, the high level of turbulence tries to create a near adiabatic profile removing the instability. This is seen in the temperature profile in Figure VI-1. The unstable layer is persistent even in hour averaged profiles as can be seen in Figure VI-3. This profile can be compared to the profile given in Figure III-2 over a flat stable boundary layer.

The complex thermodynamic and shear structure in the slope flows emphasizes the importance of using turbulent parameterization dependent upon local conditions. Although this discussion has centered upon the role of the slope flows in producing the turbulent structure, it must be remembered that it is also the turbulent exchange processes which determine the depth and strength of the slope flows. Because of the complexity of the system, it is likely that even more sophisticated or higher order turbulence models may be needed to properly handle the problem.

## Surges in the Downslope Flow

The analytical solutions in Chapter V indicated that compressibility (or adiabatic warming) may not be a satisfactory explanation for surges in downslope flows, because of the limited parameter space in which oscillatory solutions exist. An alternate mechanisms for the surges may be Richardson number instability and associated mixing of heat and momentum. The model solutions presented here did exhibit some oscillations due to turbulent bursting associated with the deformation and destabilization of the temperature profile as described above. These fluctuations are, however, very small in magnitude and have shorter periods than those surges referred to in the literature. It is possible that a different combination of surface roughness, ambient wind slope, etc. could produce longer period oscillations (see Blackadar (1978)). Also, more complete turbulent parameterization might produce a different behavior. Thus, turbulent bursting cannot be eliminated as a possible mechanisum for the surges.

# VII. Three Dimensional Slope and Mountain Flows

While the previous chapter provided a description of the characteristics of the two-dimensional slope flows, the mountain wind or the along-the-valley axis component is a three-dimensional feature, directly coupled to the side-wall slope flows. The following two case studies are designed to investigate the pooling of the cooling air in a three-dimensional valley and the development of the mountain wind in response to the pooled air.

## Valley-Plain Case Study A.

The first case study utilizes topography purposefully accentuated to maximize the development of the mountain wind. Figure VII-1 gives a three-dimensional perspective of the topography which is essentially the classic valley-plain configuration considered in the descriptive model of Defant (1951). The north end cross-section corresponds to the two dimensional cross-section utilized in Chapter VI. Grid spacing is 1 km in the east-west direction and 2km in the north-south direction except at the boundaries where the grid is stretched by 1 km per grid for 5 grids. Because gradient boundary conditions are utilized at the lateral boundarys the topography corresponds to an infinite valley extending to the north and a flat plain extending to infinity toward the south. Note that the valley floor does not slope toward the plain. The model parameters are the same as those given in Table VI-1 in the previous chapter.

The model was started at sunset with a near adiabatic initial state and was run for seven hours. As in the two-dimensional cases, the slope flows start almost immediately and begin to converge at the valley center. Slope flows also develop over the slopes leading onto the plain. The profiles of the downslope component were virtually identical to those given in the two-dimensional case.

Figure VII-1 Three-dimensional perspective of the topographic configuration used in Case A. Ridge height is 2 km; valley width is 19 km. (Note that the vertical scale is exaggerated.)

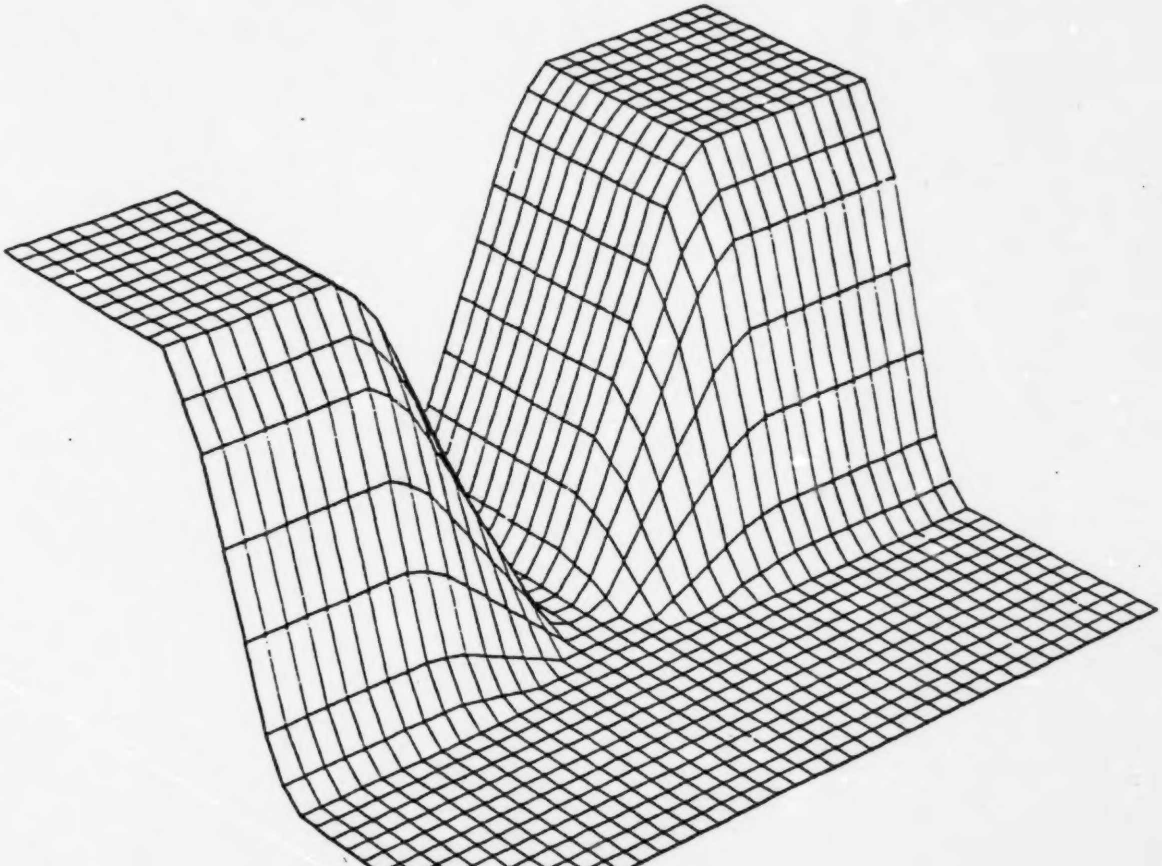

Figure VII-2 a) Times series of u component at 2 meters and 50 meters over the middle of the western sidewall (x = 15, y = 23).

b) Times series of v component at 2 meters and 50 meters at the center of the valley (x = 18, y = 23).

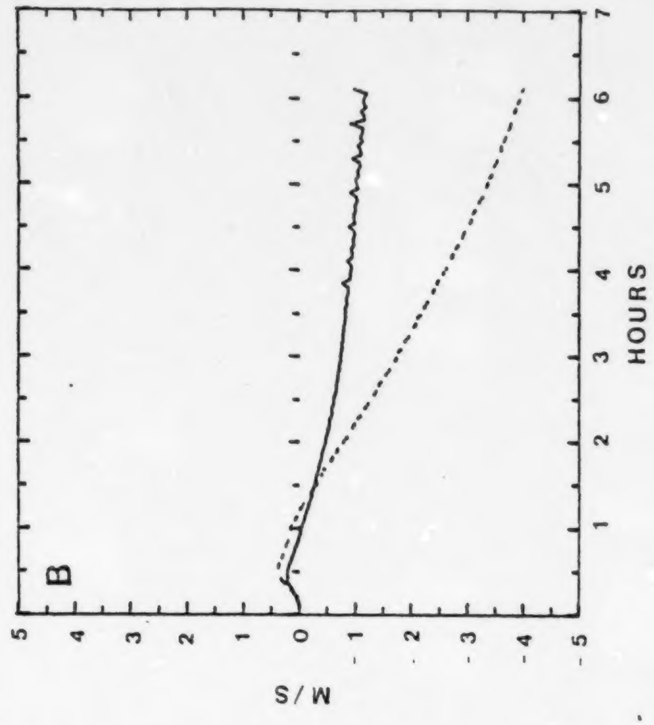
B
M/S
5
4
3
2
1
0
-1
-2
-3
-4
-5
HOURS
1
2
3
4
5
6
7

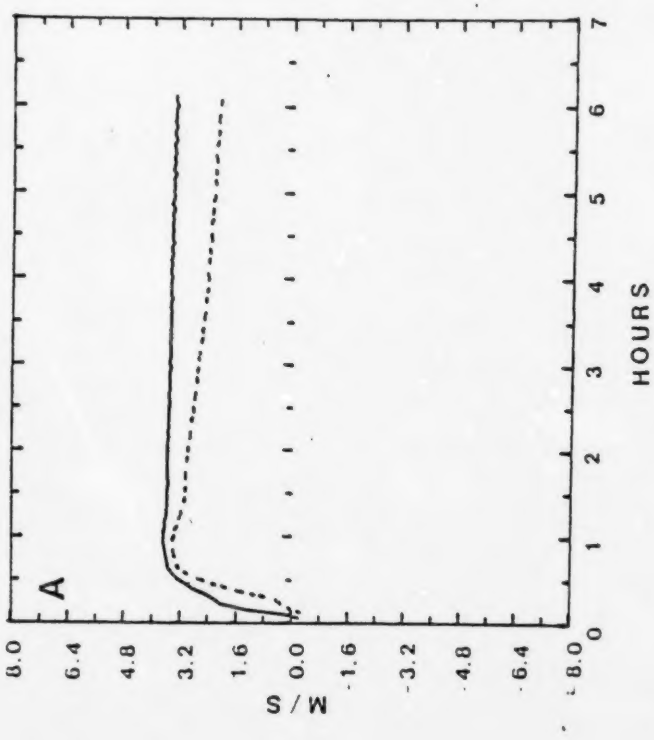
A
M/S
8.0
6.4
4.8
3.2
1.6
0.0
-1.6
-3.2
-4.8
-6.4
-8.0
HOURS
0
1
2
3
4
5
6
7

Cool air began to pool in the center of the valley as in the two-dimensional runs; however, in the three-dimensional case a true mountain wind from the valley to the plain began to develop. Figure VII-2 shows the time dependent development of both the slope flow (u-component) and mountain wind (v-component) and can be compared to the two-dimensional run (Figure VI-4) in which no significant v-component developed. As can be seen in the figure, the mountain wind does not begin immediately and lags the development of the slope flows by approximately one-hour. Also the flow toward the plain is entirely due to the pooling of the cold air since no slope exists in the valley floor.

Figure VII-3 gives contours of the mountain wind (v-component) at a cross-section of the valley after six hours. The mountain wind is pervasive and fills almost the entire valley. The development of the deep mountain flow in the third dimension is essentially the culmination of the present investigation and is consistent with the observations of Davidson and Rao (1963) and the descriptive ideas of Defant (1951) presented in Chapter IV.

Figure VII-4 gives a plan view of the velocity field at a constant $z^*$ level of 8m and 100m and shows both the effect of the slope and mountain flow on the resulting velocity vector. Note at the 100m level the magnitude of the outflow is largest at the valley opening. This is perhaps to be expected since, at least initially, the largest pressure gradient along-the-valley axis should exist here.

### Valley-Plain Case B.

Although the topography given in Case A elucidated the development of the mountain flow out of the valley, the accentuation of the scale and the cut formation is perhaps not representative of typical valleys. Figure

Figure VII-3 a) Contours of potential temperature at 2330 LST (y = 23). Contour interval is 1°K. b) Contours of the mountain wind (v-component) for the same time and location for Case A. Contour interval is 1 m/s.

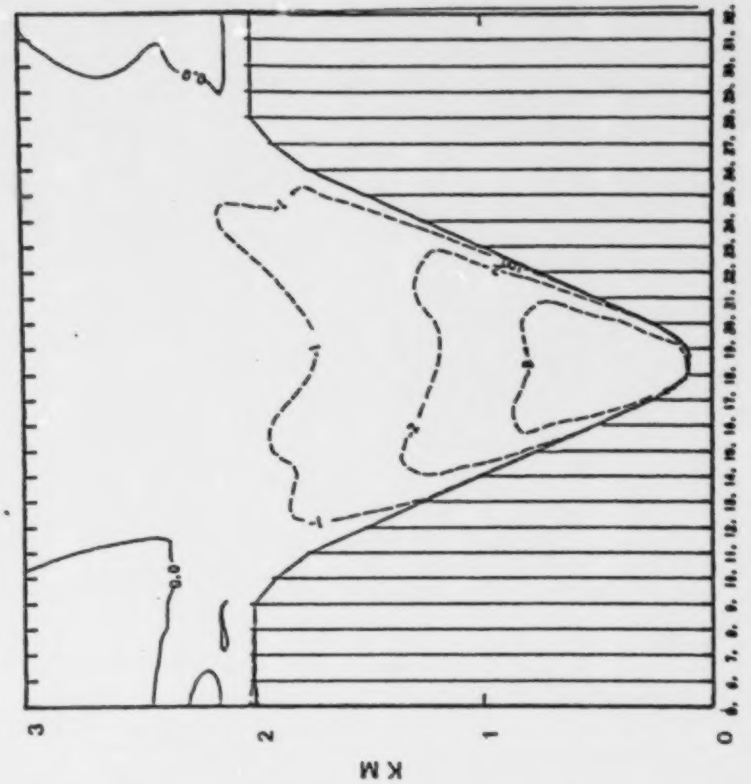
3
2
1
0
K M
0.0
0.0
-1
-1
-2
-3

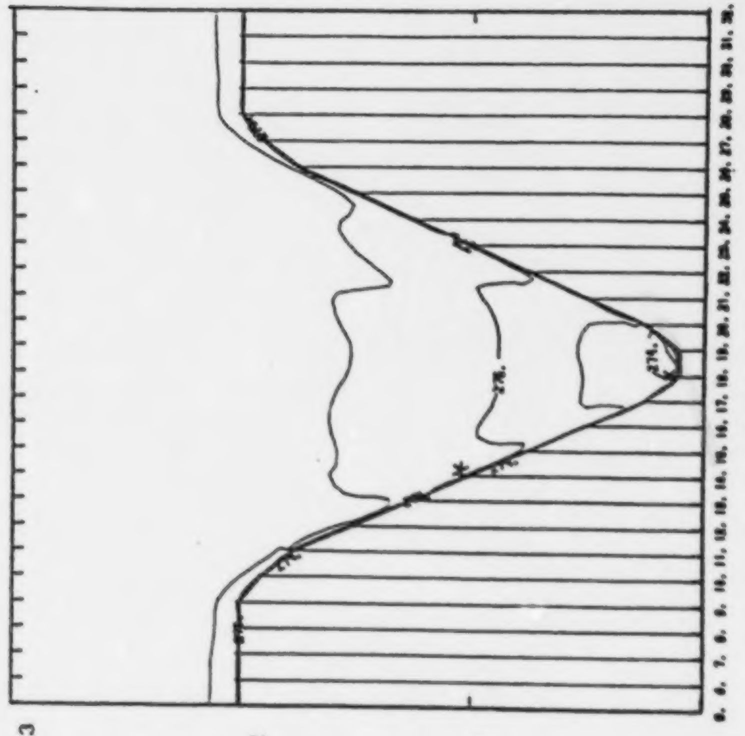
3
2
1
0
K M
274.

Figure VII-4 Plan view of velocity field for Case A at 2330 LST. a) at $z^*$ level of 8 meters. b) at $z^*$ level of 100 meters.

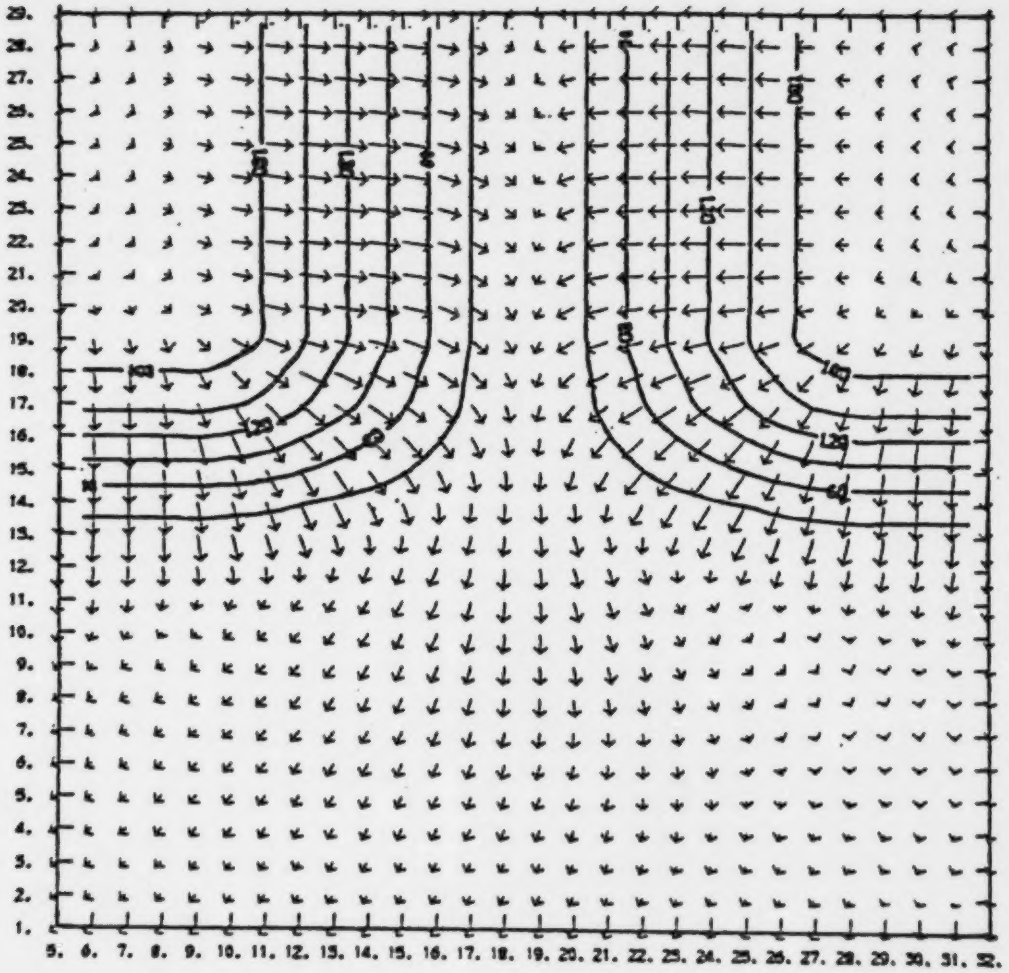
29.
28.
27.
26.
25.
24.
23.
22.
21.
20.
19.
18.
17.
16.
15.
14.
13.
12.
11.
10.
9.
8.
7.
6.
5.
4.
3.
2.
1.
5.
6.
7.
8.
9.
10.
11.
12.
13.
14.
15.
16.
17.
18.
19.
20.
21.
22.
23.
24.
25.
26.
27.
28.
29.
30.
31.
32.
100
120
60
100
120
60

A

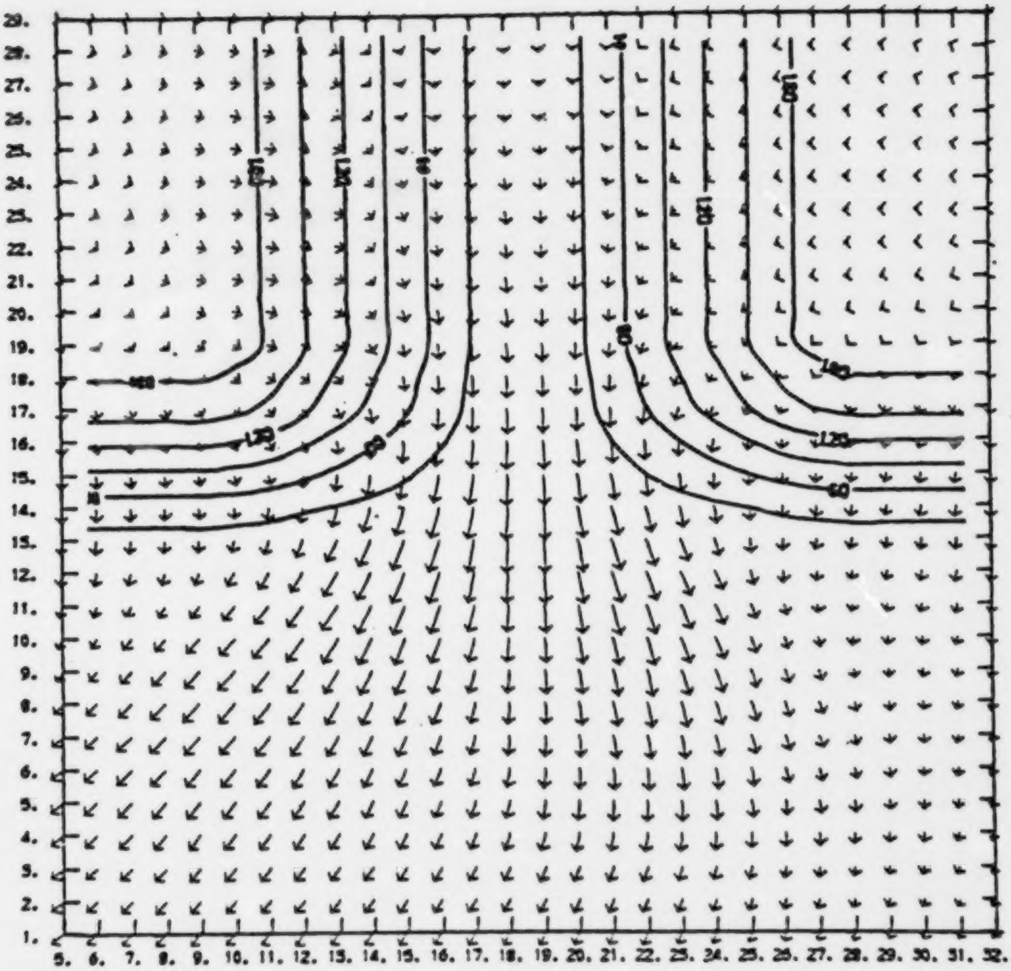
180
120
60
1. 2. 3. 4. 5. 6. 7. 8. 9. 10. 11. 12. 13. 14. 15. 16. 17. 18. 19. 20. 21. 22. 23. 24. 25. 26. 27. 28. 29.
5. 6. 7. 8. 9. 10. 11. 12. 13. 14. 15. 16. 17. 18. 19. 20. 21. 22. 23. 24. 25. 26. 27. 28. 29. 30. 31. 32.

B

VII-5 gives a three-dimensional representation of the idealized but more realistic topographic configuration utilized in the second case study. The ridge tops are 1250m high and the width of the valley is 11km so that drainage basin is smaller than in Case A.

Slope flows began almost immediately on all slopes after the start of integration. Figure VII-6 gives a plan view of the velocity field at two levels and the 8m level shows the sharp convergence zone over the center of the valley and the divergence zone over the ridge breaks. The potential temperature and mountain flow along a cross-section normal to the valley at 2330 LST for the case are given in Figure VII-7. The side wall down slope components behaved similarly to those in the other cases (see Figure VII-8) with an initial downslope acceleration with a slight overshoot (at the lower level) to the eventual nearly steady flow.

The mountain wind component (see also Figure VII-8) again lagged the development of the downslope component. The magnitude of the mountain component is less than in Case A with the decrease due to the reduced elevated area available to provide the source of the cold air which drives the mountain flow.

Figure VII-5 Three-dimensional perspective of the topographic configuration used in Case B. Ridge height is 1.25 km; valley width is 11 km.

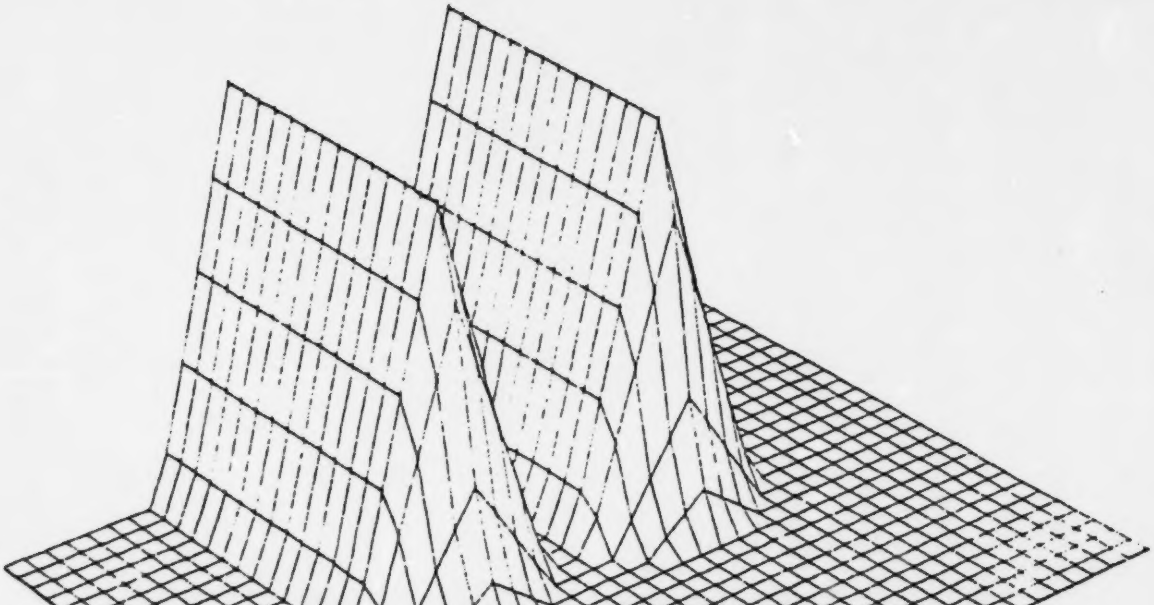

Figure VII-6 Plan view of velocity field for Case B at 2330 LST. a) at $z^*$ level of 8 meters. b) at $z^*$ level of 100 meters.

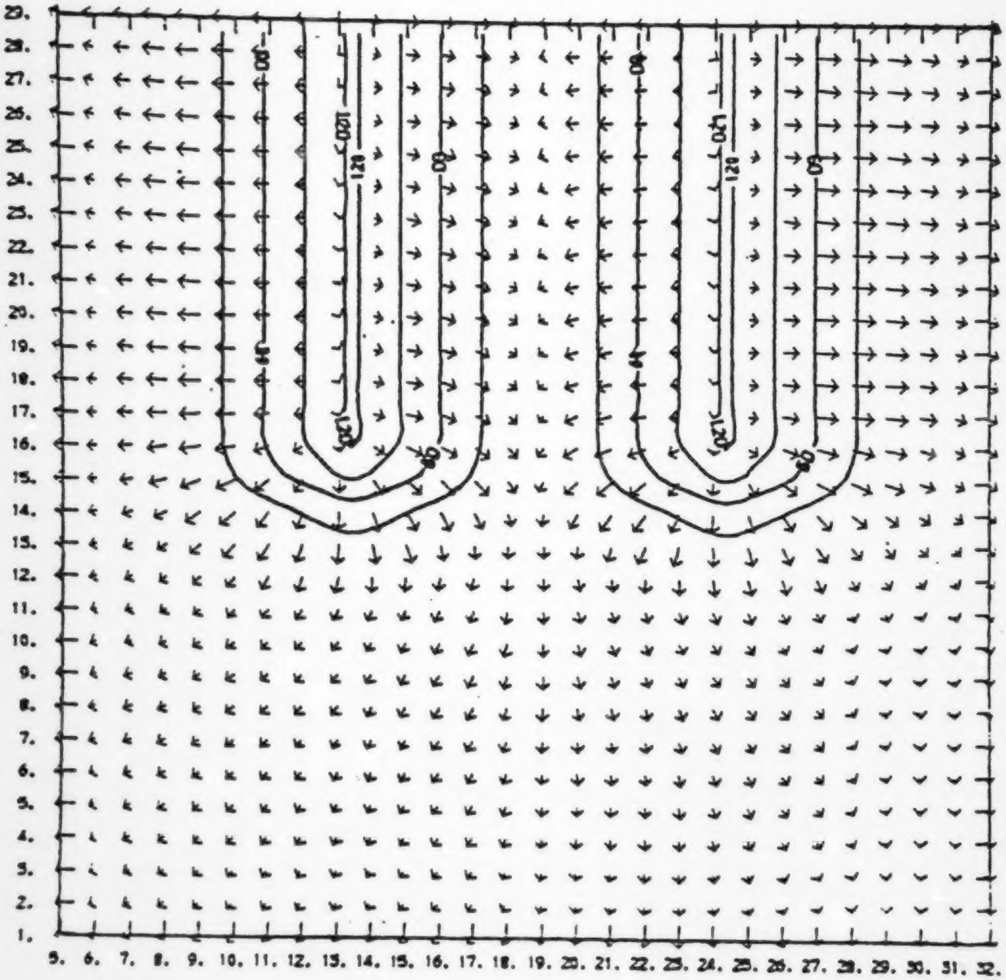
120
120
80
40
120
120
80
40
80
80
1. 2. 3. 4. 5. 6. 7. 8. 9. 10. 11. 12. 13. 14. 15. 16. 17. 18. 19. 20. 21. 22. 23. 24. 25. 26. 27. 28. 29.
5. 6. 7. 8. 9. 10. 11. 12. 13. 14. 15. 16. 17. 18. 19. 20. 21. 22. 23. 24. 25. 26. 27. 28. 29. 30. 31. 32.

A

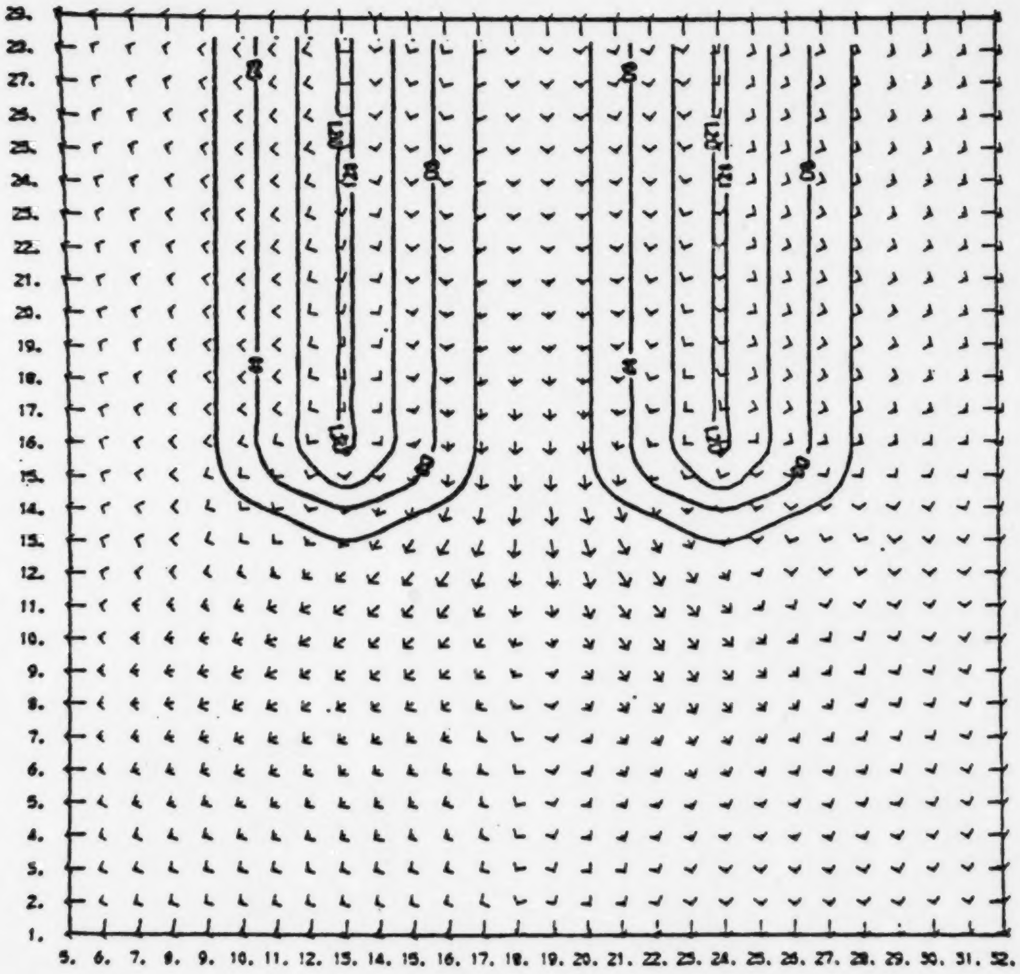
29.
28.
27.
26.
25.
24.
23.
22.
21.
20.
19.
18.
17.
16.
15.
14.
13.
12.
11.
10.
9.
8.
7.
6.
5.
4.
3.
2.
1.
5. 6. 7. 8. 9. 10. 11. 12. 13. 14. 15. 16. 17. 18. 19. 20. 21. 22. 23. 24. 25. 26. 27. 28. 29. 30. 31. 32.

B

Figure VII-7 a) Contours of potential temperature at 2330 LST ($y = 23$) for Case B. Contour interval is $1^{\circ}K$. b) Contours of mountain component (v-component) for the same time and location. Contour interval is 1 m/s.

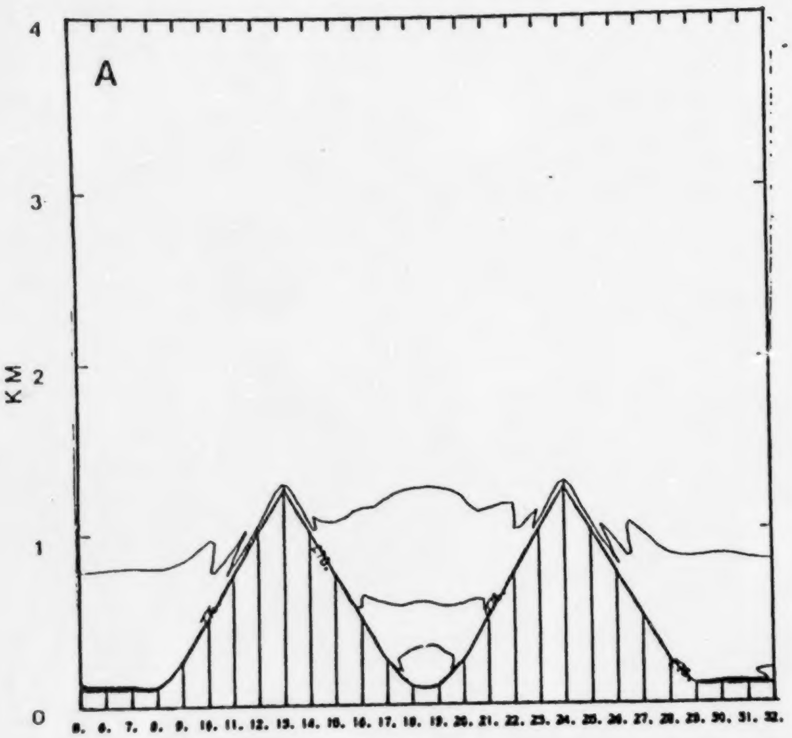
A
KM
0
1
2
3
4
5. 6. 7. 8. 9. 10. 11. 12. 13. 14. 15. 16. 17. 18. 19. 20. 21. 22. 23. 24. 25. 26. 27. 28. 29. 30. 31. 32.

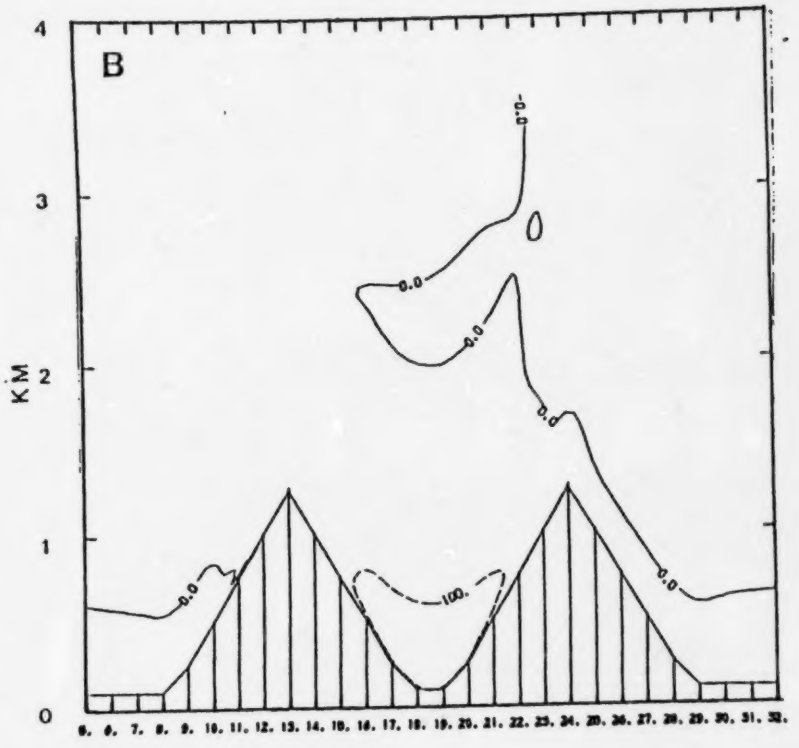
B
KM
0
1
2
3
4
-0.0
0.0
0.0
0.0
0.0
0.0
100.
5. 6. 7. 8. 9. 10. 11. 12. 13. 14. 15. 16. 17. 18. 19. 20. 21. 22. 23. 24. 25. 26. 27. 28. 29. 30. 31. 32.

Figure VII-8 a) Time series of u-component at 2 meters and 50 meters over the middle of the east facing western sidewall (x = 15, y = 23). b) Time series of v-component at 2 meters and 50 meters at the center of the valley (y = 18, y = 23).

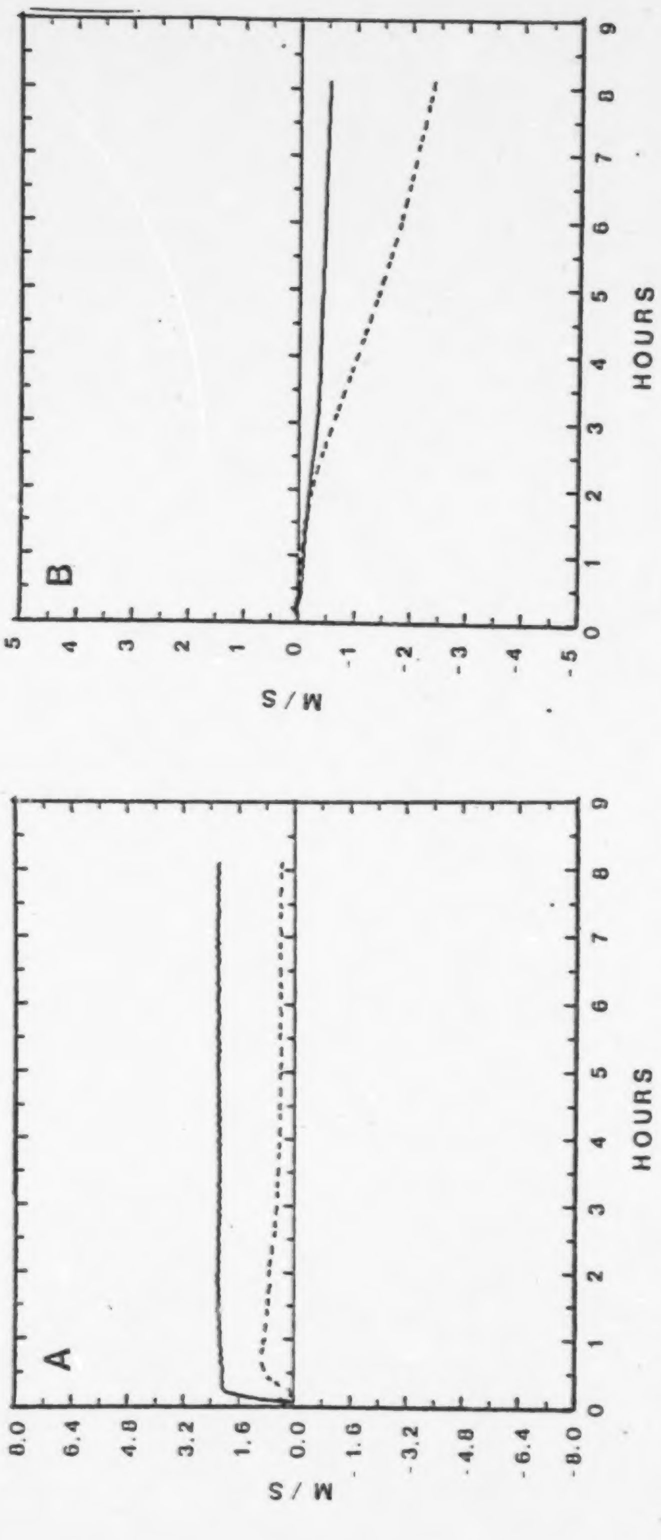
A
M / S
8.0
6.4
4.8
3.2
1.6
0.0
-1.6
-3.2
-4.8
-6.4
-8.0
HOURS
0
1
2
3
4
5
6
7
8
9
B
M / S
5
4
3
2
1
0
-1
-2
-3
-4
-5
HOURS
0
1
2
3
4
5
6
7
8
9

## VIII. Pollutant Transport

As mentioned in Chapter I coastal zones and large flat-floored valleys have been and will continue to be preferred areas for urban growth, industrial development and power production because of land suitability, water resources and transportation advantages. Unfortunately, to date, objective techniques are lacking to evaluate pollutant transport in these situations.

The first step in the analysis of pollutant transport and behavior in these complex flow situations is the construction of a representative three-dimensional velocity field. Recent investigations in the literature have pointed out some of the alternative methods available for attacking the problem. Keen (1976) in a Lake Michigan study took a kinematical diagnostic approach by deducing the velocity field from a series of pibal and tetroon trajectories during an intensive observational program. Mass consistent diagnostic models such as that of Dickerson (1978) or Sherman (1978) construct the velocity field by solving the incompressible continuity equation using observed wind measurements and terrain as constraints. The mass consistent models have some drawbacks in that for most applications the (observed) surface level wind data are sparse and in complex flow situations these may be contaminated by "local circulations" not resolved in the terrain of geographic grid. The kinematical analysis of Keen does offer a robust vertical description of the wind field which is lacking in the mass consistent models; however, observational programs needed to specify the wind field, especially in very complex terrain, would be very expensive. A third alternative, which is pursued in the present investigation, employs the three-dimensional hydrostatic, primitive equation model described previously to predict the velocity field from a prescribed set of initial conditions.

## Lagrangian Particle Model

Mean pollutant direction is often the most important factor in pollution exposures. Using the velocity field predicted by the mesoscale model, pollutant trajectories and streaklines can be determined by advecting individual tracer particles in a Lagrangian manner. For ease of computation, particle positions are converted into the terrain following coordinate system given in Chapter II. Computationally, source release points for the particles to be tracked are first converted into the terrain follfowing system. Particle positions in the $z^*$ system at time t + 1 are then computed from their initial positions, $x^t$, $y^t$, $z^{*t}$ by

$$\begin{aligned} x^{t+1} &= x^t + u^t \,\Delta t \\ y^{t+1} &= y^t + v^t \,\Delta t \\ z^{*t+1} &= z^{*t} + w^{*t} \,\Delta t \end{aligned} \qquad \text{VIII-1}$$

where u, v are velocity components in the x and y directions (in the $z^*$ system), respectively, and

$$w^* = \frac{dz^*}{dt},$$

is the vertical velocity component in the $z^*$ system. The velocity components, u, v, $w^*$ applied to the particles are interpolated from the dynamic model grid points using a volume weighted interpolation scheme described by Tuescher and Houser (1974).

The u and v particle velocities below the first model grid point are computed from similarity theory using the profile functions mentioned previously while $w^*$ is assumed to progress linearly to zero within the surface layer. Particles passing through the lateral and top boundaries of the model are ignored in subsequent calculations. At the bottom boundary, deposition processes are neglected and particles are assumed reflected from the ground surface. For display purposes, particle positions are backtransformed into the standard z system.

The particle model was designed to allow particle releases at multiple horizontal and vertical positions in the model domain. As an example of the particle transport model, test runs were made using a mesoscale model flow field for the South Florida Peninsula. Figure VIII-1a shows a plan view of streak lines of particles released at various positions over the South Florida Peninsula from a release height of 50 meters. Particles were released at ten-minute intervals starting at sunrise. Figure VIII-1b gives a corresponding vertical view of the particle streaklines when viewed looking northward along the peninsula. Figures VIII-2a and VIII-2b give the same depiction of particle motion except particles were released from a height of 300m. As can be seen, the complex mesoscale circulations produce transport behavior much different from the usual Gaussian model asssumption of straight line transport. For a complete description of these transport experiments see McNider and Pielke (1978).

The transport model formulated and tested in this section will be applied to slope and mountain flows in Chapter X.

Figure VIII-1 Particle streaklines at 1900 EST from 50 meter release heights. (A) Plan view showing x - y distributions of particles. (B) Vertical view, looking northward, showing x - z distributions of particles. Particles were released at 10-minute intervals beginning at sunrise.

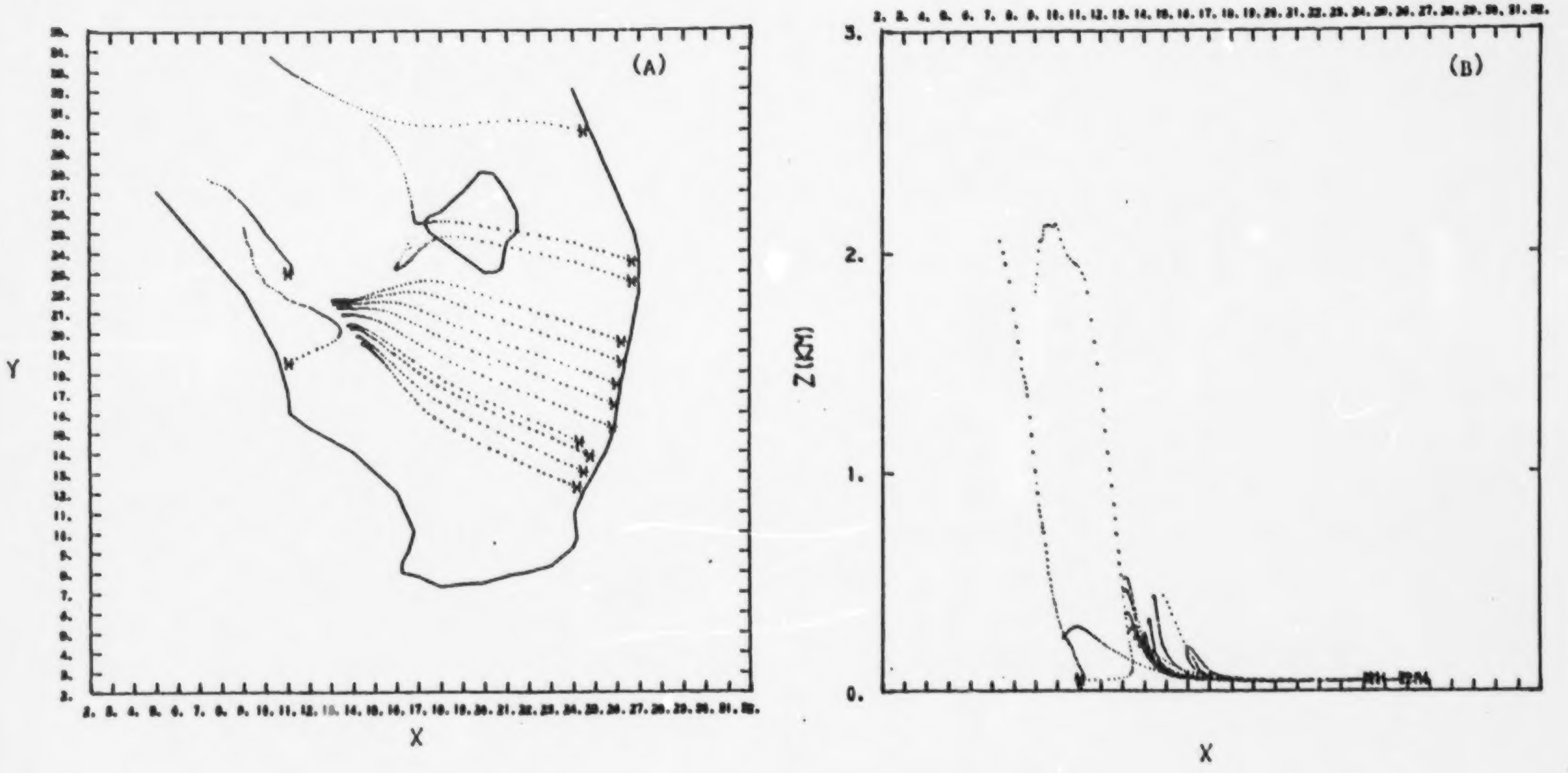
(A)
Y
X
(B)
3.
2.
1.
0.
Z (KM)
X

Figure VIII-2  Same as Figure VIII-1 except for 300 meter release height.

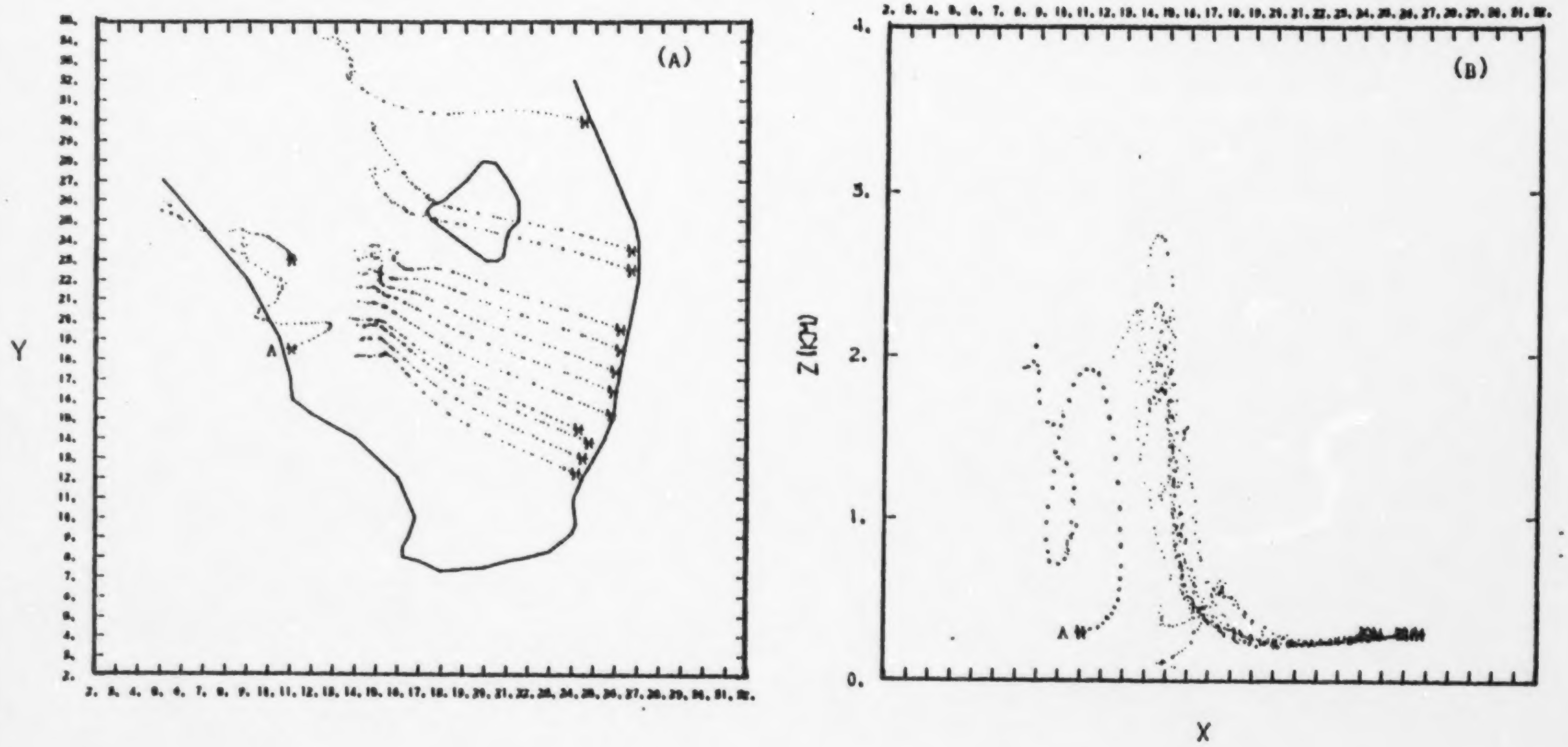
(A)
(B)
Y
X
Z (KM)
0.
1.
2.
3.
4.
A

## IX. SUB-GRID SCALE PLUME DISPERSION

Although mesoscale models of mountain-valley circulations can provide physically consistent descriptions of the complex three-dimensional flow fields, their application to transport and diffusion from point sources, which are of practical interest to regulatory officials is inhibited by the mismatching of scales between the point source plumes and the coarse grid resolution in the mesoscale model. In the past mesoscale modelers have generally attempted to address transport and diffusion using the advection-diffusion equation (K - theory) and have employed numerical difference schemes to solve the equation. While this approach can easily incorporate non-uniform flow fields and variable exchange coefficients, artificial diffusion due to the numerical scheme can rapidly deteriorate the accuracy of the solution. Recent advances in numerical advection techniques such as the quasi-Lagrangian spline and finite element approaches, as well as moment conservation methods (see Long and Pepper (1976) for a review) have greatly increased accuracy in the representation of advection; however, even the best numerical grid schemes deteriorate rapidly as the wavelength of the phenomena approaches the grid resolution. Newly released point source puffs or plumes have wavelengths much less than the coarse grid scale available in mesoscale models, thus standard numerical techniques can only be applied after the plume has grown to a resolvable scale in the mesoscale model grid.

In addition to the numerical problems involved in representing the advection is the proper handling of the turbulent dispersion. As with advection, use of gradient transfer theory and standard numerical difference schemes require extremely fine grid resolution to properly define concentration gradients from point sources and this resolution is not available in the mesoscale model. Even if the grid resolution were available, there is the problem of the theoretical inaccuracy of K-theory for plumes whose scale is small compared to the dominant turbulent scales. Application of K-theory to the plume dispersion requires that the effective K be a function of plume travel time as opposed to the fixed grid point K available from the mesoscale model.

To solve the grid scale problem as well as the K-theory inaccuracy, there is the option of parameterizing the sub-grid scale processes using analytical approaches such as Gaussian dispersion schemes. However, analytical parameterizations can not be done properly with present mathematical methods in the highly sheared environments of sea-breeze and mountain-valley ciruclations where mean wind shear can substantially affect dispersion rates.

In the following we present a Lagrangian particle scheme which utilizes turbulent statistics extracted from a coarse grid mesoscale model boundary layer in order to represent diffusion. Although still in an experimental stage the Lagrangian particle model avoids the grid scale problems mentioned above, is simple to apply in sheared environments, and is more theoretically accurate than K-theory for plumes whose scale is small compared to the turbulent scales. The particle scheme is first tested using the mesoscale model simulation of Day 33 of the Wangara experiment given in Chapter III and the results compared to the more complex dispersion experiments carried out by Willis and Deardorff (1978), and Lamb (1978).

## Lagrangian Particle Model

The Lagrangian particle model is based upon a Markov process (Smith (1968)) in which the Lagrangian turbulent fluctuation of a parcel is linearly related to the turbulent fluctuation at an earlier time. The fluctuation in the u-component, for example, is given by the recursive relation,

$$u'(t) = u'(t - \tau)\, R(\tau) + u''(t - \tau). \qquad \text{IX-1}$$

$R(\tau)$ is the autocorrelation coefficient at time interval $\tau$, and $u''(t)$ is a random turbulent component which is assumed to be independent of $u'(t)$. The random component is taken to be Gaussian and to have a standard deviation

$$\sigma_{u''} = \sigma_u \, (1 - R^2(\tau)\,)^{\frac{1}{2}} \qquad \text{IX-2}$$

where u is the local turbulent standard deviation. Recently, using field measurements, Hanna (1979) verified to a good degree of confidence the validity of the linearity assumption and independence of the random component and performed simple dispersion expeiments using IX-1. Reid (1979) has also examined dispersion in neutral surface layers using this method which can be referred to as a conditioned particle scheme.

In the present investigation we employ the conditioned particle scheme to examine particle dispersion in the convective boundary layer as a test case utilizing a simplified coarse grid boundary layer model to deduce the turbulent characteristics, $\sigma_u$ and $R(\tau)$, needed to close the conditioned particle scheme. Because the ultimate intent of the scheme is for mountain-valley and sea-breeze flows, the Lagrangian particle scheme has been generalized to operate in a non-uniform grid and terrain following coordinate system consistent with the mesoscale model. The vertical coordinate $z^*$, is defined by the transformation

$$z^* = \bar{s}\,\frac{z - z_G}{s - z_G} \qquad \text{IX-3}$$

where $\bar{s}$ is the height of the top of the model, z the vertical coordinate in the Cartesian system, and $z_G$ is the height of the topography. Source release points for the particles to be transported and dispersed in the model domain are first converted into the $z^*$ system using IX-3. Particle positions are then computed in a Lagrangian manner from

$$\begin{aligned} x^{t + \Delta t} &= x^{t} + (u(t) + u'(t))\,\Delta t \\ y^{t + \Delta t} &= y^{t} + (v(t) + v'(t))\,\Delta t \\ z^{*t + \Delta t} &= z^{*t} + (w^{*}(t) + w^{*\prime}(t))\,\Delta t, \end{aligned} \tag{IX-4}$$

where u'(t) is obtained from IX-1 with v'(t) and w*'(t) calculated from analogous expressions corresponding to IX-1. In IX-4 u(t) and v(t) are mesoscale velocity components in the transformed coordinate system, while

$$w^{*} = \frac{dz^{*}}{dt}$$

is the corresponding vertical component. For display purposes and calculations of dispersion statistics, particle positions are back transformed into the standard Cartesian system. Also for computational efficiency in relating mesoscale grid parameters to the particle positions, the particle positions are defined in terms of fractions of cardinal grid points rather than absolute coordinates.

The u(t) and v(t) particle velocities below the first model grid point are computed from similarity theory using the profile functions in the boundary layer model while w*(t) is assumed to progress linearly to zero within the surface layer. The turbulent component w*'(t) is not taken to zero, however, and particles are assumed to reflect perfectly from the ground surface.

## Turbulent Statistics from the Mesoscale Model

Since the Langrangian particle model is to be ultimately used in conjunction with the complex sea breeze and mountain-valley flow fields predicted by the mesoscale model, the turbulent statistics needed to utilize the conditioned particle scheme must be deduced consistently from the dynamically evolving mesoscale boundary layer. This is accomplished for the vertical component in the convective boundary layer using the relationship suggested by Hanna (1968)

$$K_m = A\sigma_w\lambda_m \qquad \text{IX-5}$$

where $K_m$ is the momentum exchange coefficient, $\lambda_m$ is the peak wavelength in the vertical velocity spectra and A is a proportionality factor. Although $K_m$ is available from the mesoscale model boundary layer, the length scale $\lambda_m$ must be determined from observations. Fortunately, recent technical advances and field experiments have provided fairly good estimates of $\lambda_m$ throughout the boundary layer. Estimates given by Kaimal et al. (1976) as a function of the planetary boundary layer depth $z_i$ and z/L were utilized as follows:

$$\lambda_m = \begin{cases} z\,/\,(.55 - .38\, z/L\,) & 0 \le z \le L \\ 5.9z & L \le z \le .1\, z_i \\ 1.8\, z_i\,(1 - \exp\,(-4z/z_i) & \\ \quad -.0003\, \exp\,(8z/z_i)) & .1\, z_i < z < z_i \end{cases} \qquad \text{IX-6}$$

The last expression contains a modification suggested by S. J. Caughey and S. G. Palmer (unpublished) reflecting additional observations near the top of the boundary layer showing a contraction in $\lambda_m$ near $z_i$. Note that $z_i$ and L can be taken from the mesoscale model so that there is internal consistency in the expression relating the length scale, $\lambda_m$, and $K_m$.

In the initial tests using IX-5 and the most recent estimates of A = .17 it was found that the near surface ratio $\sigma_w/u^*$ did not converge to the expected value of approximately 1.3 even though the model surface layer obeyed similarity laws. Further pursuit of this contradiction using well known expressions from similarity forms of $K_m$ in the surface layer and formulations of $\sigma_w$ and $\lambda_m$ in the surface layer indicated that A is not constant, but a function of stability. For example near the surface using $\lambda_m$ from IX-6, $\sigma_w/u^* = 1.3$ and $K_m = kzu^*/\phi m$ in IX-5, A was found to vary from .18 for near neutral conditions to .05 for unstable conditions. Figure IX-1 shows estimates of A as a function of z/L.

Using A(z/L) in eq. IX-5 and $K_m$ from the model boundary layer in the Wangara simulation produced $\sigma w/u^*$ profiles consistent with observations in the surface layer as shown in Figure IX-2. In the extended convective boundary layer the model produced $\sigma_w$ profiles which were also reasonably consistent with observations (Figure IX-3). The $\sigma_w$ values drop off more rapidly near $z_i$ than the observations due to the shape of the cubic polynomial used to represent the exchange coefficients above the surface layer which could probably be corrected by different constraints on the interpolation procedure.

In the stable boundary layer, rather than use IX-5 to deduce $\sigma_w$ a direct relationship between the local gradient Richardson Number and $\sigma_w$ was developed from the graphical representation given by Blackadar (1978). A suitable fit was found to be

$$\sigma_w = 1.2 \frac{(Ri_c - Ri)}{Ri} sl \qquad \text{IX-7}$$

where s is the magnitude of the local shear and l is the mixing length. Figure IX-4 shows the deduced $\sigma_w/u^*$ ratio from the Wangara simulation compared to the observations by Caughey et al. (1979) in the evolving stable layer. Although there are differences, the model predictions are probably within the observational scatter in stable conditions. Also, the model under prediction of the $\sigma_w$ may be due to a slight slope at the site where the observations were taken.

Figure IX-1 Plot of $A = K_m/\sigma_W{}_m$ as a function of Z/L as computed from standard formulas for $K_m$, $\sigma_W$ and $\lambda_m$ in the atmospheric surface layer.

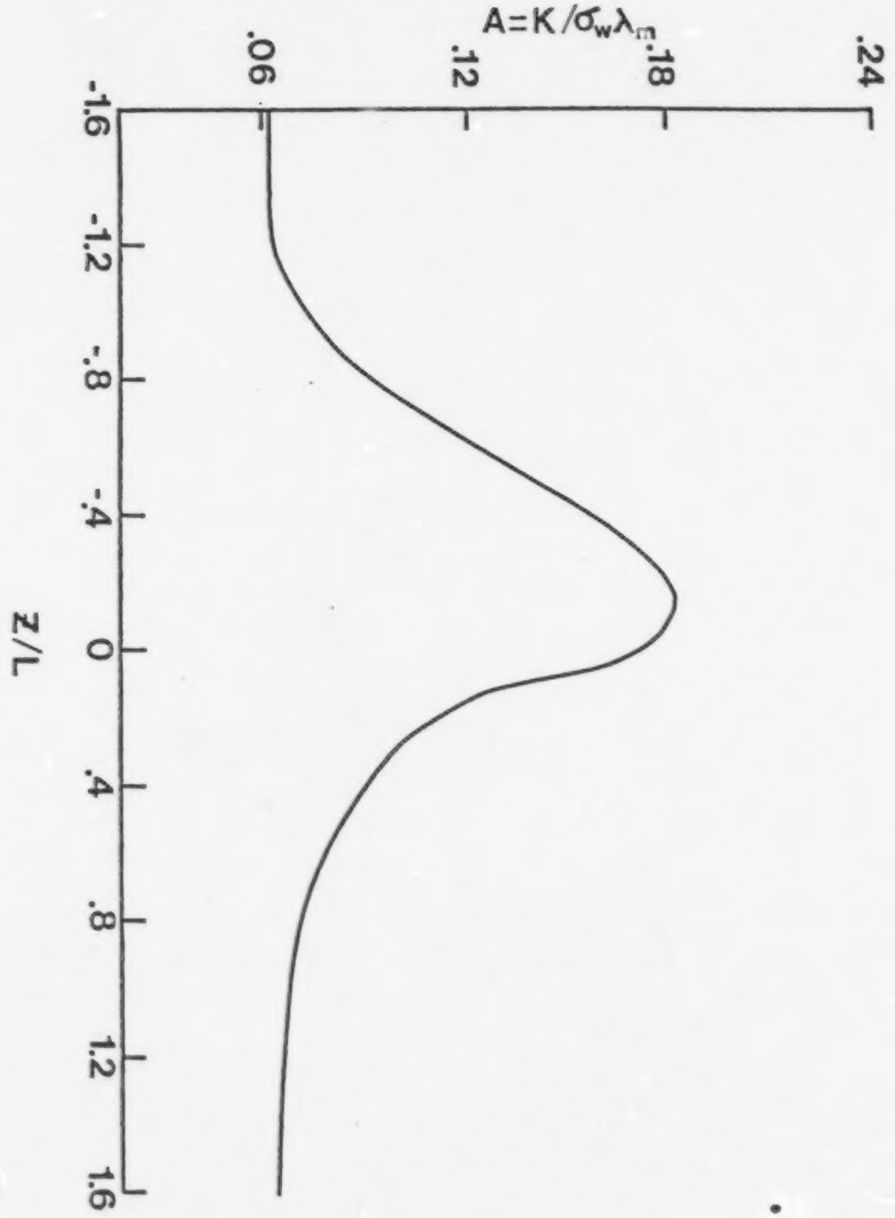
A=K/σ_wλ_m
.06
.12
.18
.24
-1.6
-1.2
-.8
-.4
0
.4
.8
1.2
1.6
Z/L

Figure IX-2 Plot of $\sigma_w/u^*$ extracted from the mesoscale model compared to the observational best fit by Panofsky et al. (1977).

Model Simulation Wangara Day 33
Unstable Boundary Layer

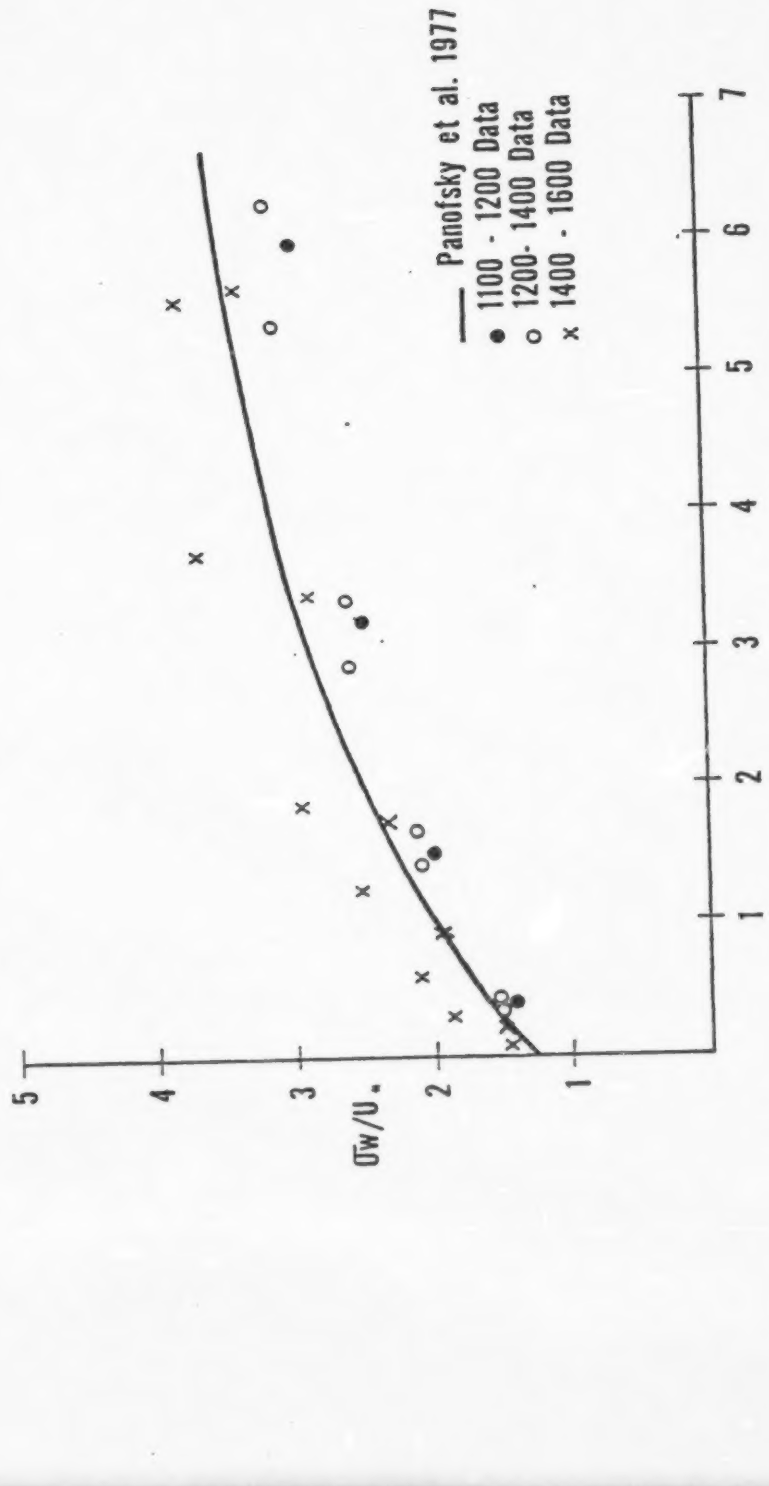

Figure IX-3 Plot of model extracted scaled $_w$ in the planetary boundary layer compared to observational composites and the numerical study by Deardorff (1974b). The dashed line was extracted from an unpublished study by F. B. Smith of the British Meteorological Service. ($w_*$ is the convective velocity scale given by $w_* = u_* \, (-h/kL)^{1/3}$ )

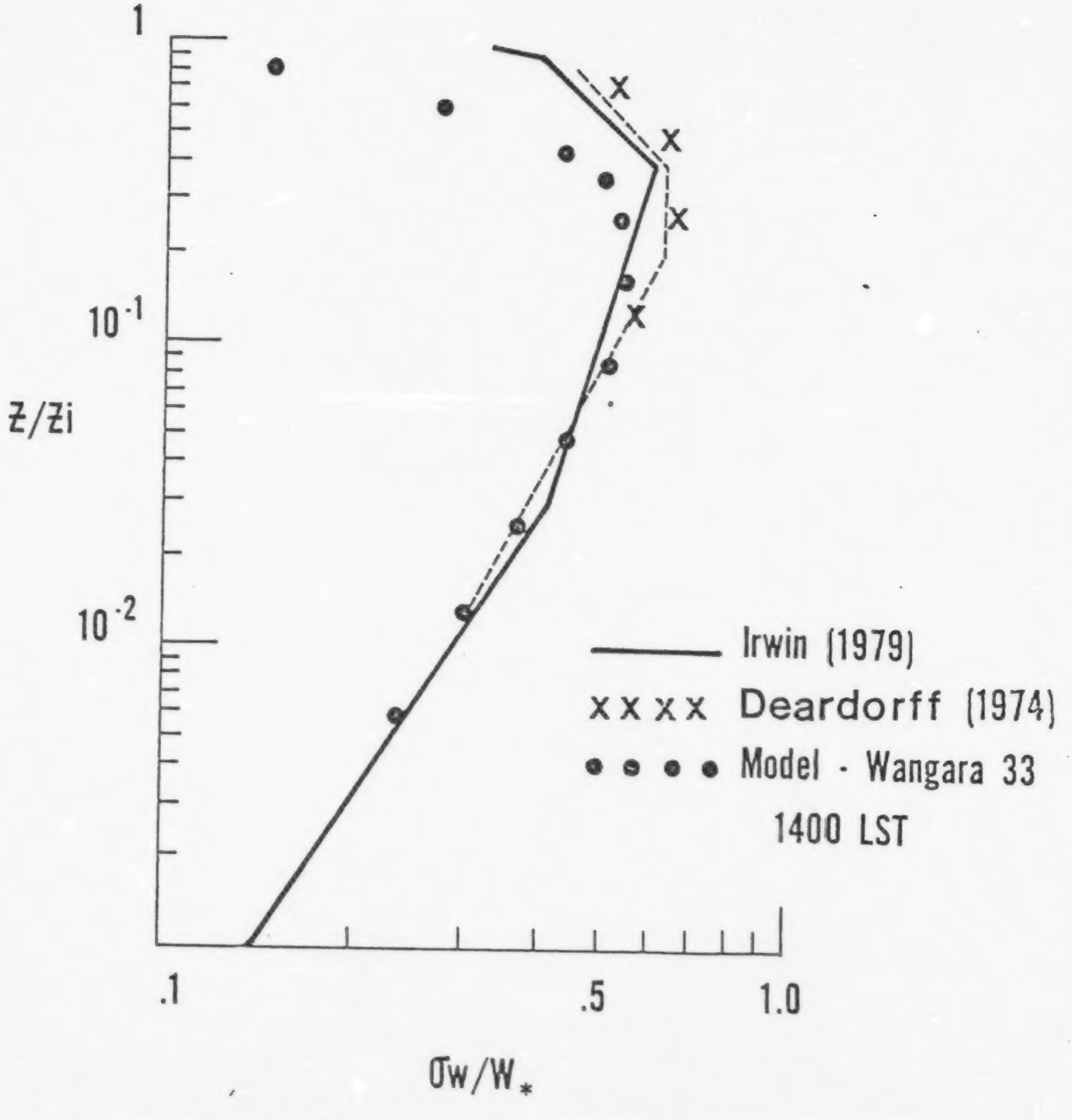
1
10⁻¹
10⁻²
Z/Zi
.1
.5
1.0
σw/W*
Irwin (1979)
xxxx Deardorff (1974)
● ● ● ● Model - Wangara 33
1400 LST

Figure IX-4 Plot of $\sigma_w/u^*$ in the stable boundary layer. (H is estimated height of the nocturnal boundary layer, defined as the height to which turbulence is evident.)

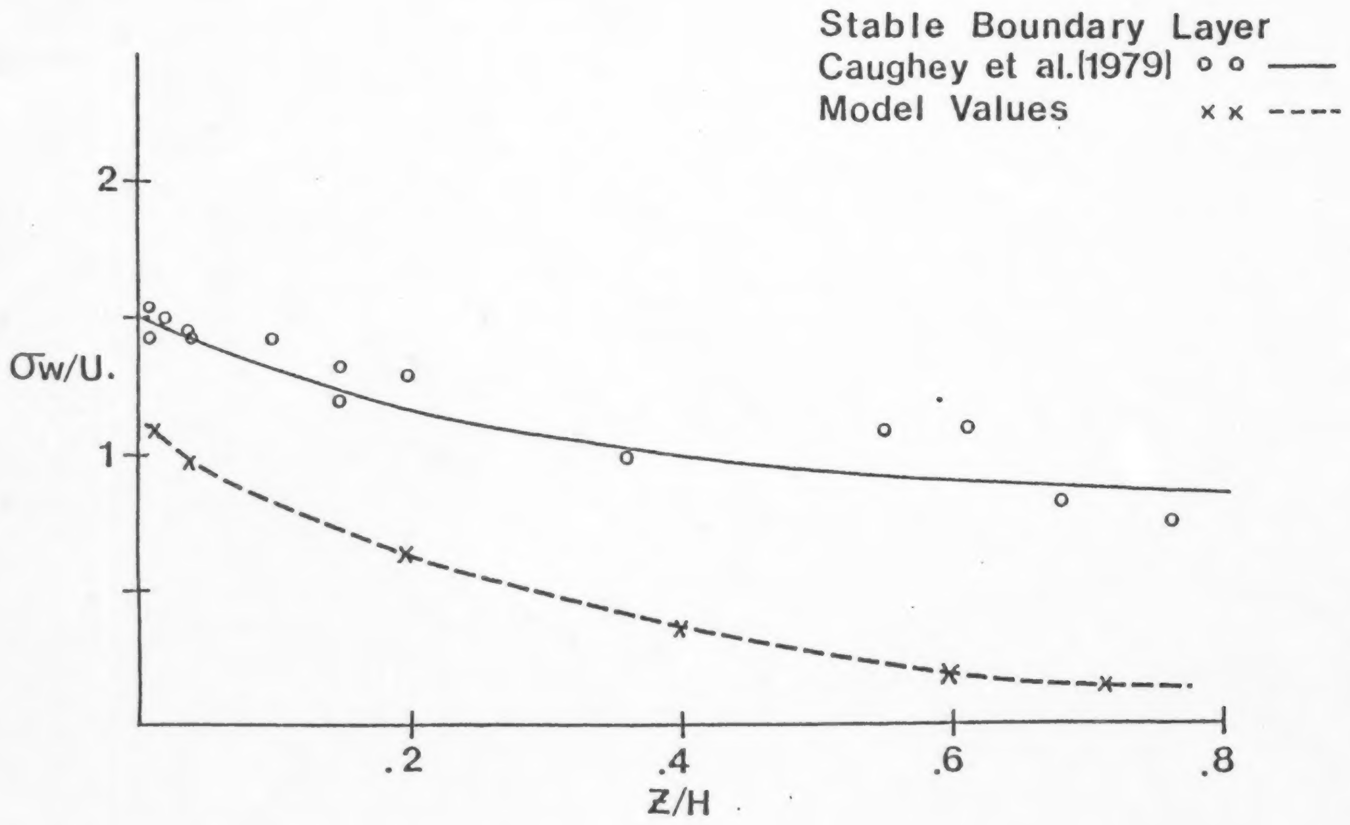
Stable Boundary Layer
Caughey et al.[1979] ○ ○ ——
Model Values × × ----
σw/U.
2
1
.2
.4
.6
.8
Z/H

For the horizontal components in the convective boundary layer the formula proposed by Panofsky et al. (1977) was utilized, i.e.

$$\sigma_u = \sigma_v = u_* (12 + .5 z_i / - L)^{1/3} \qquad L < 0 \qquad \text{IX-8}$$

and for neutral and stable conditions:

$$\sigma_u = \sigma_v = 2.3 u^*. \qquad L \geq 0 \qquad \text{IX-9}$$

The length scales $\lambda_{m,u}$ in the convective boundary layer were again taken from the work of Kaimal et al. (1976) with

$$\lambda_{m,u} = \lambda_{m,v} = 1.5 z_i \qquad \text{IX-10}$$

Standard methods (Pasquill (1974)) were used to relate the length scales $\lambda_{m,w}$, $\lambda_{m,v}$ and $\lambda_{m,u}$ to $R_u(\tau)$ $R_v(\tau)$ and $R_w(\tau)$ needed in IX-1. Specifically, the Eulerian time scale, $T_E$, was computed by

$$T_E = .2 \lambda_m / (u^2 + v^2 + w^2)^{\frac{1}{2}} \qquad \text{IX-11}$$

(where $\lambda_m$ refers to $\lambda_{m,u}$, $\lambda_{m,v}$ or $\lambda_{m,w}$) and the Lagrangian time scale, $T_L$, by

$$T_L = \beta T_E$$

with

$$\beta = .6 \bar{u} / \sigma_w \qquad \text{IX-12}$$

limited by

$$\beta \leq 10. \qquad \text{IX-13}$$

The autocorrelation function $R(\Delta t)$[1] was taken to be exponential so that

$$R(\Delta t) - \exp (- t/T_L). \qquad \text{IX-14}$$

In total the turbulent statistics deduced from the mesoscale model boundary layer appear to agree well with the available observations.

---

[1] In the numerical model $\tau$ is taken to be the time step $\Delta t$.

## SIMPLE DISPERSION EXPERIMENTS

Employing the turbulent statistics extracted from the Wangara boundary layer simulations the Lagrangian particle model was used to examine dispersion from elevated point sources. Lamb (1978) has also examined particle dispersion in a simulated Wangara boundary layer using the higher closure model by Deardorff (1974a). Lamb used the resolvable turbulent components available from Deardorff's fine mesh grid for direct particle transport and parameterized the sub-grid scale turbulent transport using a conditioned particle or Markov-1 process similar to that given in IX-1. Willis and Deardorff (1978) also reported on tank dispersion experiments for the convective boundary layer which agreed well with Lamb's numerical calculations.

In the present investigation, dispersion experiments were designed to emulate the experimental procedures of Lamb (1978), and Willis and Deardorff (1978) (henceforth referred to as LWD) so that a comparison could be made between the dispersion characteristics in the simplified mesoscale boundary presented here and the more complete boundary layer of Deardorff (1974a). Figure IX-5 shows root-mean-square vertical dispersion from a release of 1300 particles at .25 $z_i$. A time step of 10 seconds was used in the simulation although an increase in time step up to 30 seconds did not appreciably alter the dispersion statistics. A suggestion proposed by Reid (1979) to reduce the effective velocity variance to avoid false dispersion for long time steps was incorporated in the particle scheme and given by

$$\sigma_w{}^2 = \frac{2\, T_L{}^2\, (\sigma_w{}^2)_o}{\Delta t^2} \left[\exp - (\Delta t/T_L) + (\Delta t/T_L) - 1\right] \qquad \text{IX-15}$$

where $(\sigma_w{}^2)_o$ is the initial velocity variance.

Figure IX-5 Plot of root-mean-square vertical dispersion as predicted by the current conditioned particle scheme. See Willis and Deardorff (1978) for an explanation of the non-dimensional scaling.

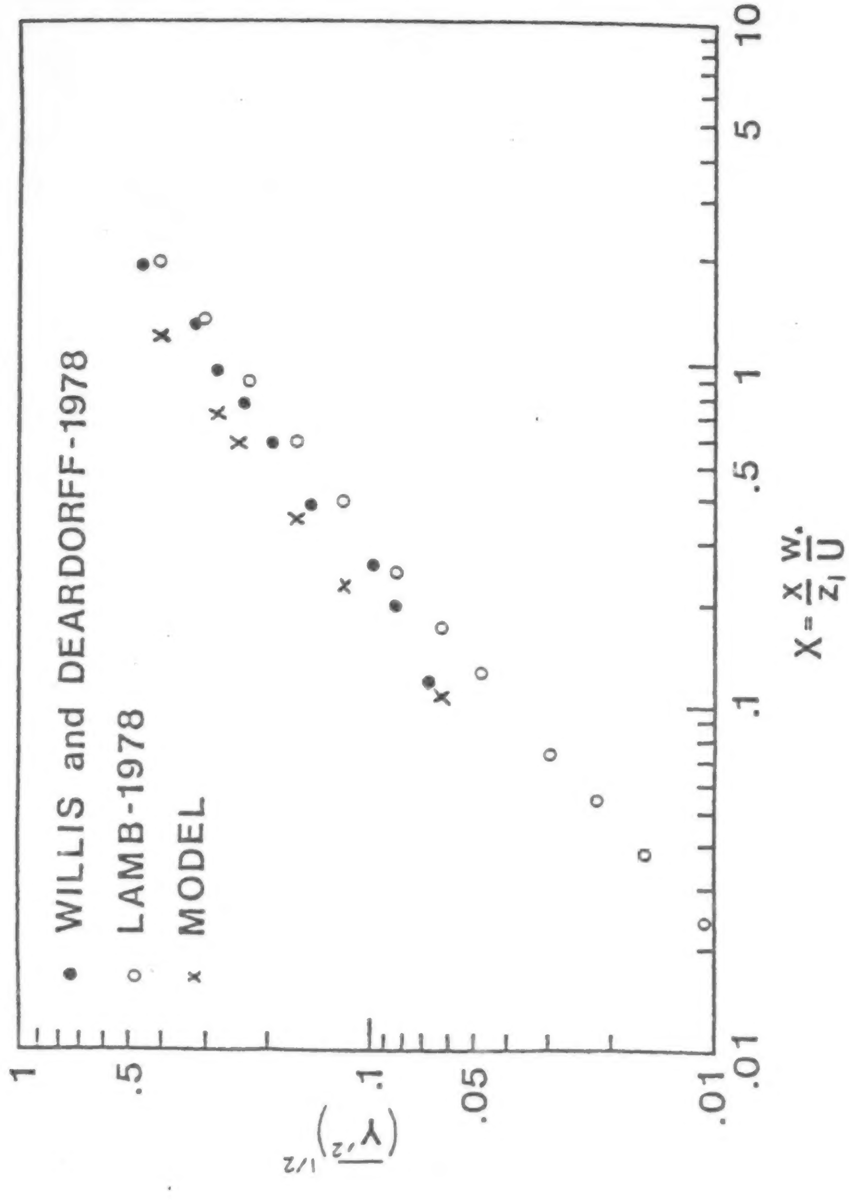

● WILLIS and DEARDORFF-1978
○ LAMB-1978
x MODEL
1
.5
.1
.05
.01
$(\overline{Y'^2})^{1/2}$
.01
.1
.5
1
5
10
$X = \frac{x}{z_i}\frac{w_*}{U}$

As can be seen the agreement between the present model and LWD is reasonably good. Ths slight underprediction of the spread in the present model is due to lower $\sigma_w$ values at the upper levels of boundary layers. (refer back to Figure IX-3). The slowing of the vertical spread in the present model at $.3 < x < .5$ appears to lie between the tank results and Lamb's results and indicates that the Lagrangian integral time scales are comparable.

The root-mean-square lateral spread given in Figure IX-6. also agrees reasonably well with LWD. The overprediction of the lateral spread is a result of the similarity prediction used for $\sigma_v$. Willis and Deardorff indicated that $\sigma_v = .7\ \sigma_w$ at $.25\ z_i$ while the model output yielded $\sigma_v = .85\ \sigma_w$.

Although the above tests indicate that the conditioned particle model using the extracted turbulent statistics from the mesoscale model boundary layer can successfully predict the dispersion statistics, some problems were encountered with particle accumulations. In the convective boundary layer particle accumulations developed near the surface, while in the stable boundary the accumulations were noted at the top of the nocturnal boundary layer. The particle accumulations were evidently due to two factors, 1) the gradient of turbulent energy and 2) the movement of particles in finite time steps in the non-homogeneous turbulent field.

The first problem causes particles to be essentially trapped in zones of low turbulent energy. Since the turbulent characterizations as depicted by $\lambda_m$ and $\sigma_w$ are felt to reflect observations accurately, some other factors must be at work in the real atmosphere to prevent these accumulations.

Figure IX-6 Same as figure IX-5 except for the lateral dispersion.

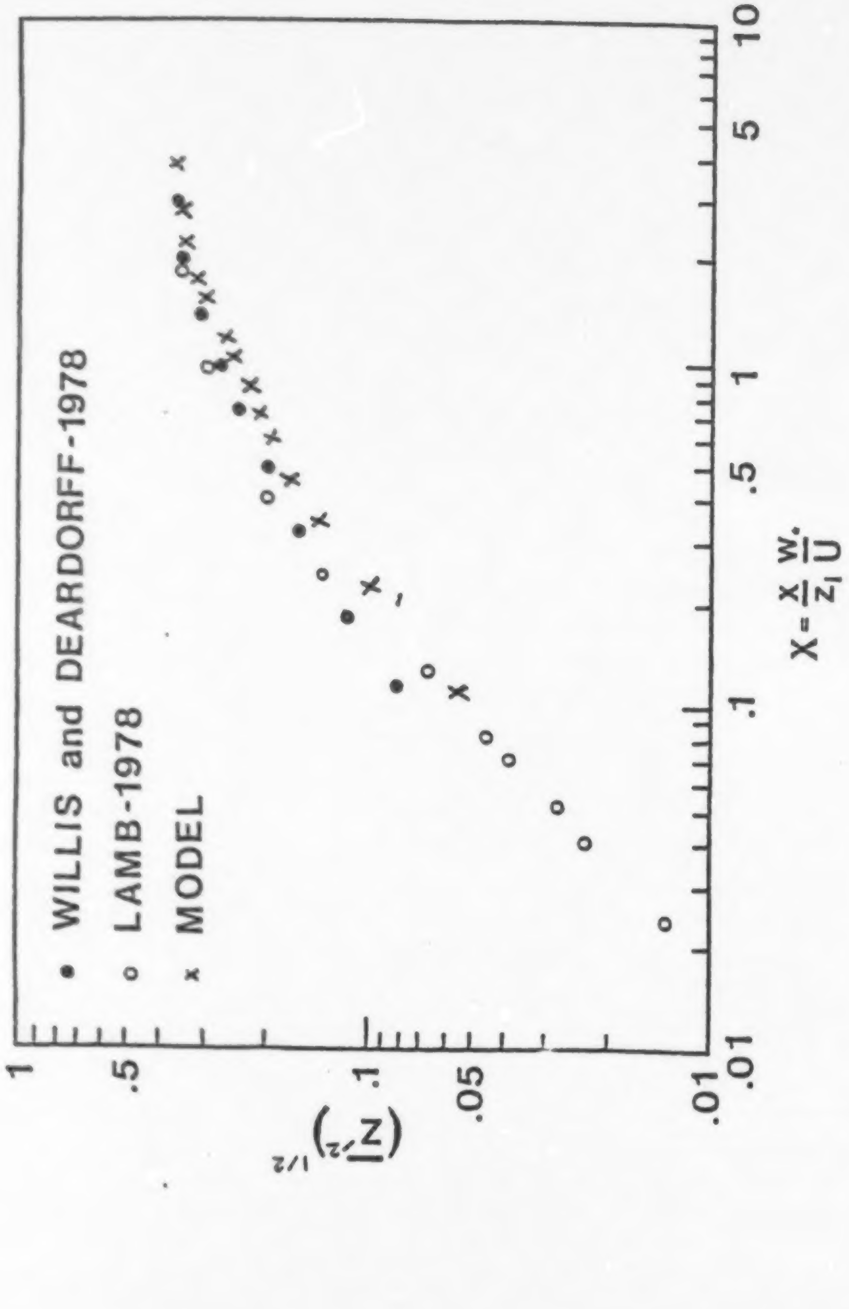
● WILLIS and DEARDORFF-1978
○ LAMB-1978
x MODEL
$(\overline{z'^2})^{1/2}$
1
.5
.1
.05
.01
$X = \frac{x}{z_i}\frac{w_*}{U}$
.01
.1
.5
1
5
10

Observations (Chiba (1978)) indicate that turbulent distributions show some skewed characteristics rather than the zero skew utilized for the random turbulent component w" in IX-1. The skewness as summarized by Chiba indicates a dependence upon stability; positive skewness for unstable conditions and negative skewness for stable conditions. In order to account for this skewness in the present model, the random turbulent w" was taken from a modified Gaussian distribution, i.e.,

$$\begin{aligned} w'' &= F\,G_+ + (1/F)\,G_- - N \qquad && \text{Skew} > 0 \\ w'' &= (1/F)\,G_+ + F\,G_- + N \qquad && \text{Skew} < 0 \end{aligned} \qquad \text{IX-16}$$

where $G_+$ and $G_-$ are positive and negative random components taken from a normal distribution with zero mean and standard deviation given by IX-2. Variable factors F and N, dependent upon the desired skewness, were found (based upon statistical tests[1]) to be

$$F = -.028 + .6\,|S|$$

$$N = .54\,|S|$$

where S is the skewness parameter ($S = \Sigma\, w'^{\,3}/N\,\sigma_w$). The skewness as a function of stability was determined by fit of Chiba's data, i.e.,

$$\begin{aligned} S &= \frac{.6}{.68\,(1 - 15\,z/L)^{-\frac{1}{4}}\,25 - 1.8\,z/L} + .1 \qquad && z/L < 0 \\ S &= -.2\,(z/L)^{0.2} + .1 \qquad && z/L > 0 \end{aligned} \qquad \text{IX-17}$$

The second problem of finite particle increments within gradients of turbulent energy was addressed using a recursive relation to make a first order correction to the turbulent energy dependent upon the movement of the particle, i.e.,

---

[1] Tests indicated that IX-16 gave the desired skewness within 8% and a near zero mean (less than 3% of $\sigma_w$).

$$(\sigma_w)_N = \frac{\partial \sigma_w}{\partial z} \quad w^{*\prime} \Delta t + (\sigma_w)_o \qquad \text{IX-18}$$

where $(\sigma_w)_o$ is the standard deviation of the vertical turbulent velocity at the start of the time step and $(\sigma_w)_N$ is found to be the new value which is actually used to complete the final $w^{*\prime}$.

Both of the techniques described above reduced the problem of particle accumulations, however, further work needs to be done to properly specify the skewed distributions, and to better determine the role of skewness in affecting particle dispersion. Appendix B gives a step-by-step description of the methods used in the particle dispersion scheme.

## Summary and Conclusions of Dispersion Parameterization

A Lagrangian conditioned particle scheme which is easy to apply in non-uniform mesoscale flow fields was combined with a coarse grid mesoscale model boundary layer to make simple dispersion calculations. Turbulent statistics needed to utilize the conditioned particle scheme were extracted from the simplified boundary layer model, and agreed reasonably well with observations. Dispersion using the mesoscale model boundary layer predictions also agreed very well with the experiments of LWD.

Further work needs to be done on the assessment of the conditioned particle scheme near the surface, especially the proper treatment of particles in areas of sharp gradients of $T_L$ and $\sigma_w$. Examination of individual particle motions near the surface in tank experiments such as Willis and Deardorff (1978) may be one of the most efficient ways to answer these questions. The solution may require different distributions of $w'$ near the surface to decrease the resident times of particles effectively trapped by the small $\sigma_w$ and $T_L$. If the boundary problems can be adequately solved, use of the conditioned particle scheme in conjunction with a mesoscale model could be a powerful tool to examine transport and diffusion in complex flow fields.

# X. TRANSPORT AND DISPERSION IN THE MODELED SLOPE AND MOUNTAIN FLOWS

Using the flow fields and turbulent characteristics of modeled mountain flows in Chapter VII, mean transport and dispersion characteristics are examined using the Lagrangian techniques described in Chapters VIII and IX. Velocity components and other necessary information from the model runs were saved on tape files for the transport and dispersion experiments which follow.

## Streaklines and Trajectories

Figure X-1 provides a time series of snapshots of particle streaklines in the flow field of Case A from Chapter XII. Particles were released every 100 seconds beginning at sunset from a height of eight meters above the western sidewall. As can be seen, the particles first move down the sidewall in the slope flow, then, move upward vertically over the center of the valley. As the particles move upward, they are then carried a slight distance up the valley. Finally as the mountain flow develops, both those particles carried up the valley and newly emitted particles began to move down the valley. In the vertical depiction it can be seen that the older particles also descend as they move out of the valley.

Figure X-2 gives another representation of the transport in the form of trajectories of selected particles from the releases depicted in the previous figure. Particles tracked were released at the indicated times in the figure legends. The early particles have more complex trajectories while the later particles move more directly down the valley in the established mountain wind.

## Particle Dispersion

Using the conditioned particle model described in Chapter IX dispersion statistics are examined for the spread of a puff in the turbulent and

Figure X-1 Time series of snapshots of streaklines for particles emitted into the mountain flow of Case A Chapter VII. Figures top to bottom give snapshots respectively at 1, 3, and 5 hours after sunset. Vertical depictions are on the left; horizontal depictions on the right. Terrain is not illustrated since it would mask the particle locations.

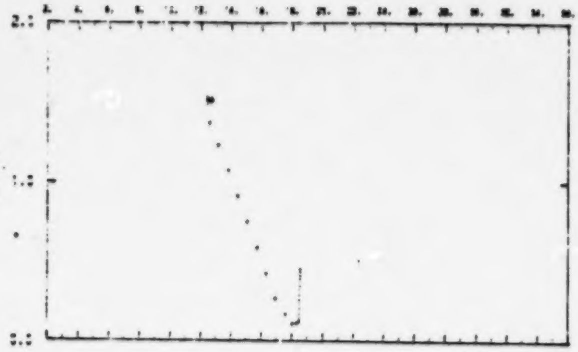
2.0
1.0
0.0
Z(KM)

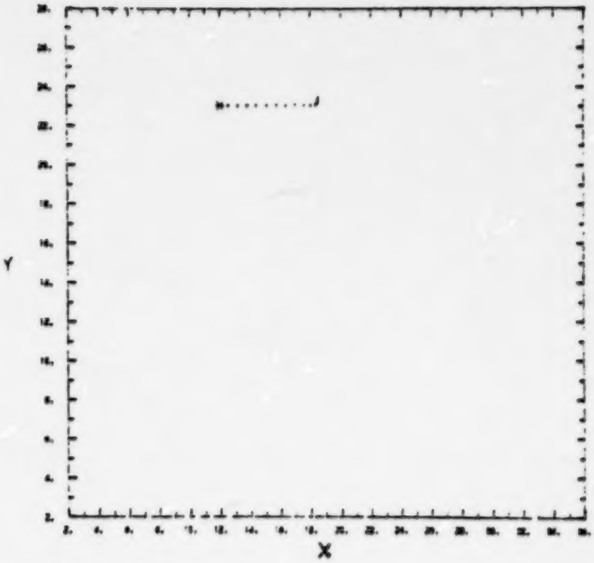
Y
X

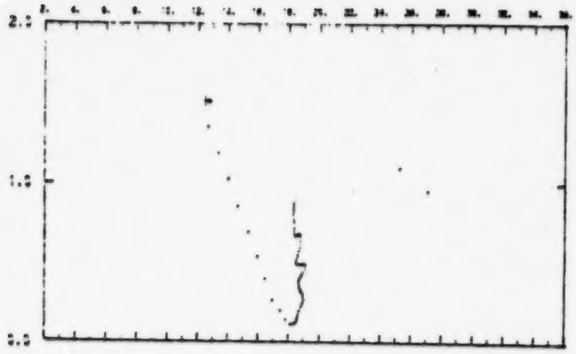
2.0
1.0
0.0
Z(KM)

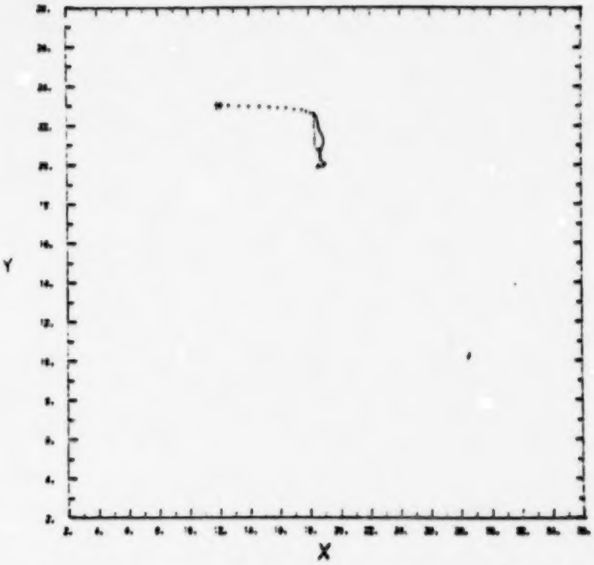
Y
X

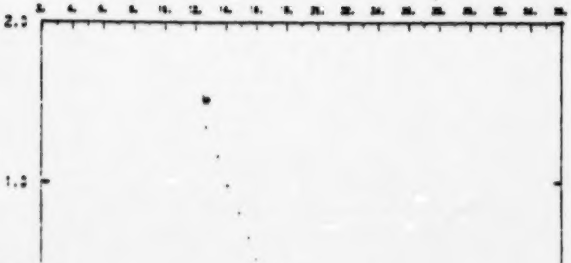
2.0
1.0
0.0
Z(KM)

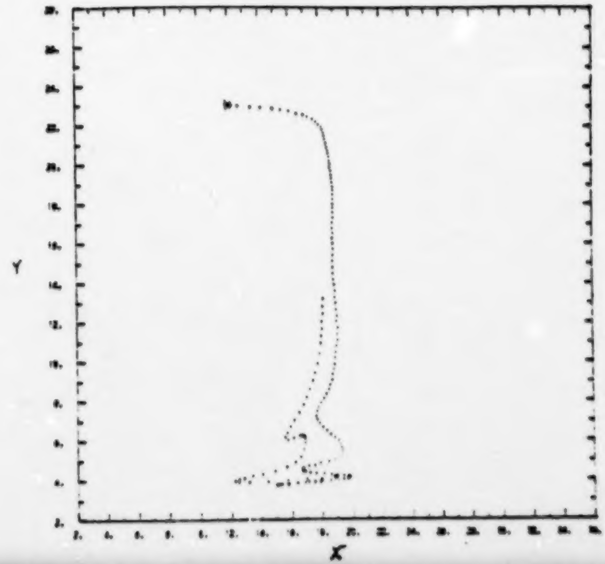
Y
X

Figure X-2 Trajectories of particles released an hour apart from a height of 2 meters. Final heights in kilometers are given to the side of the end of the trajectory.

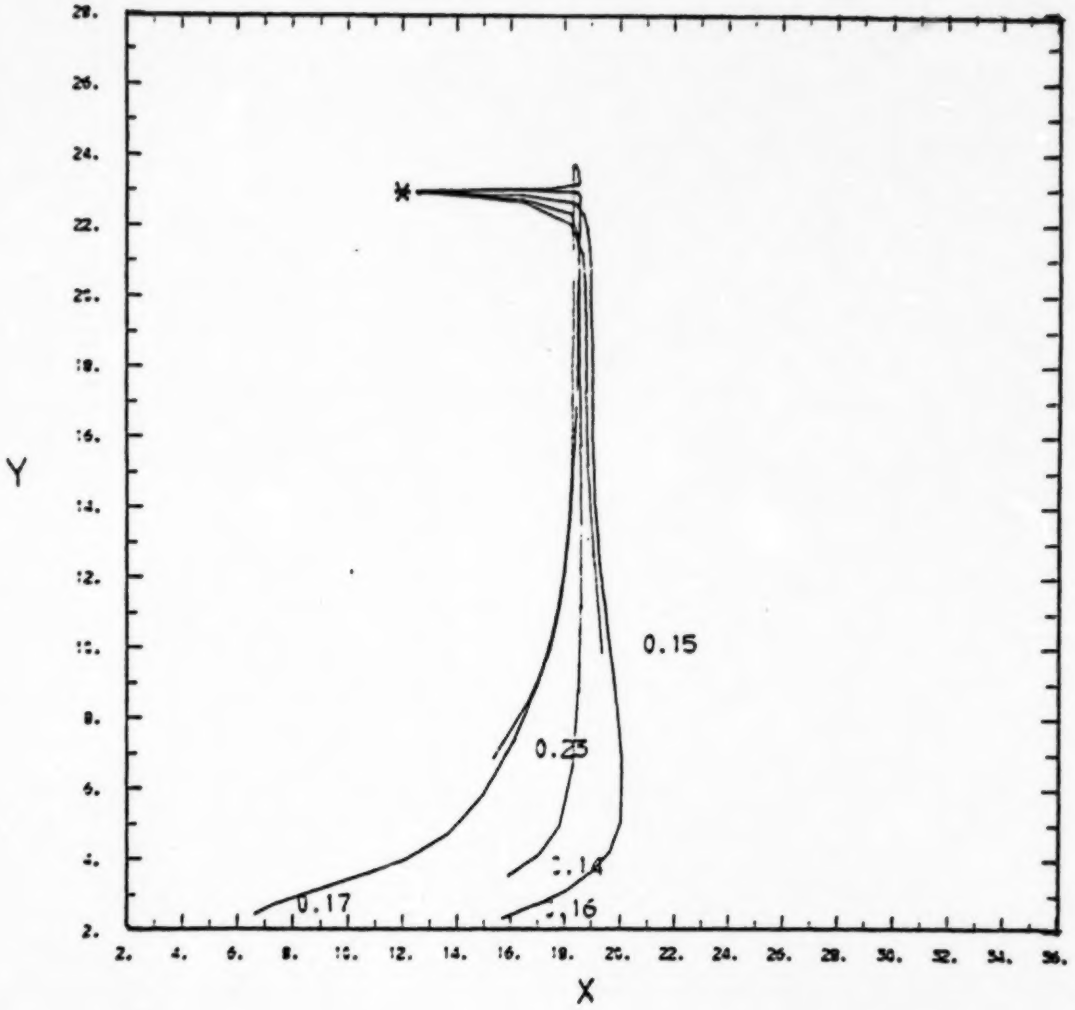
Y
X
2.
4.
6.
8.
10.
12.
14.
16.
18.
20.
22.
24.
26.
28.
30.
32.
34.
36.
0.15
0.25
0.14
0.16
0.17

velocity fields of the three-dimensional simulations. In order to isolate the effect of the slope and mountain flows a control experiment was conducted over a flat, slightly stable boundary layer. The control experiment was similar to the Wangara boundary layer experiments described in Chapter III except that a roughness length of 7 cm was used along with an imposed geostrophic wind of 12 m/s. The surface was cooled producing a stable temperature profile; but, with the strong wind, boundary layer parameters (using Golder's (1972) nomogram) indicated a Pasquill-Gifford classification near Class 4. In the first test, particles (1300 particles) were released within the boundary layer from a height of eight meters and allowed to disperse without transport by a mean wind so that shear induced dispersion would not be a factor. Figure X-3 gives scaled root-mean-square vertical spread as a function of dimensionless distance for the experiment. Dimensionless distance is proportional to time and is not related to actual distance since transport was not used. Lateral spread is also given in Figure X-4 while Figure X-5 gives the along-the-wind axis spread.

Similar experiments were undertaken for the Case A Chapter VIII mountain flow. Particles were released from a height of eight meters over the western sidewall after the slope flows had been established. Again, the first experiment was conducted without transport by the mean wind so that spread was only due to the turbulent field. Figures X-3 through X-5 give the root-mean-square spreads for the case of no wind and show the enhanced dispersion due to the turbulence field generated in the slope flow as compared to the case over the flat boundary.

Figures X-3 through X-5 also give the dispersion statistics for the slope case in which a mean wind was included. For the slope case with no mean wind, the upward curvature is due to the sharp increase of $\sigma_w$ near the

Figure X-3 Vertical dispersion for the three cases described in the text. Root-mean-square spread is scaled by the boundary layer height. 0 - Flat boundary no wind. ● - Slope case no wind. X - Slope case with wind.

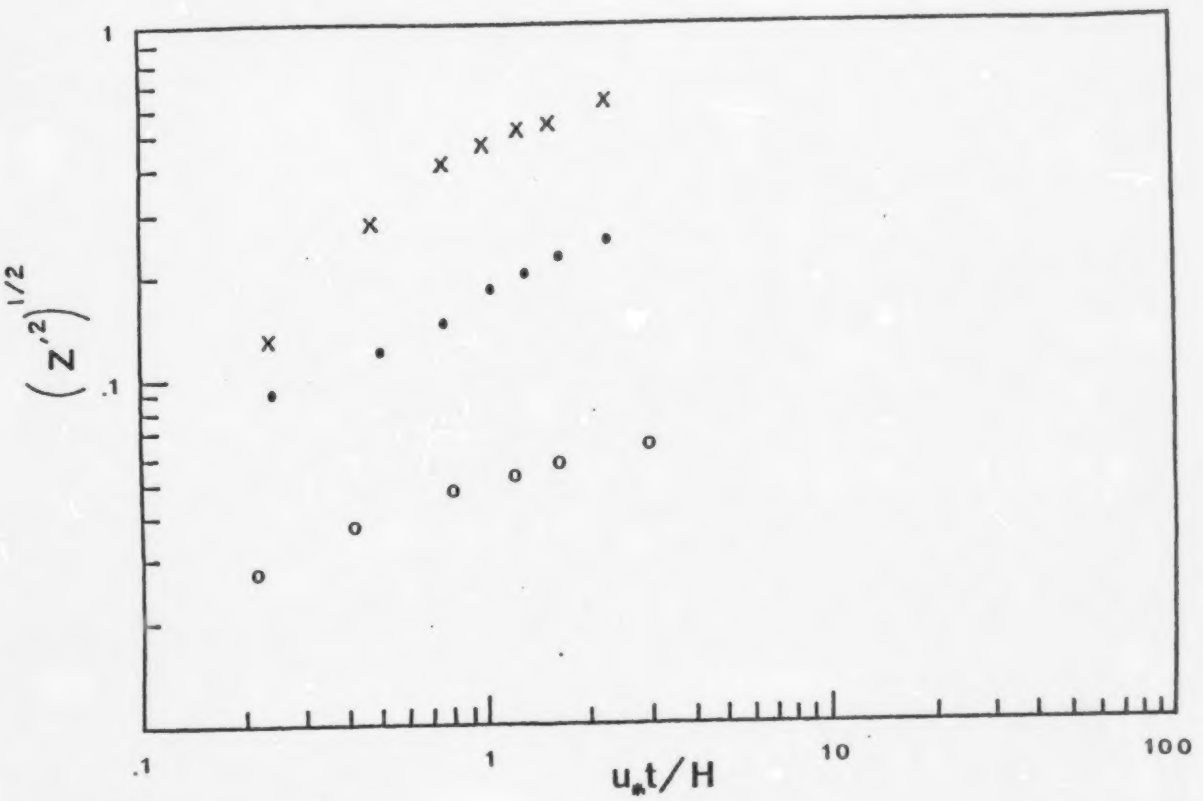
$\left(\overline{z'^2}\right)^{1/2}$
1
.1
.1
1
10
100
$u_*t/H$

Figure X-4 Lateral (Y) dispersion for the three cases described in the text. 0 - Flat boundary no wind. ● - Slope case no wind. X - Slope case with wind.

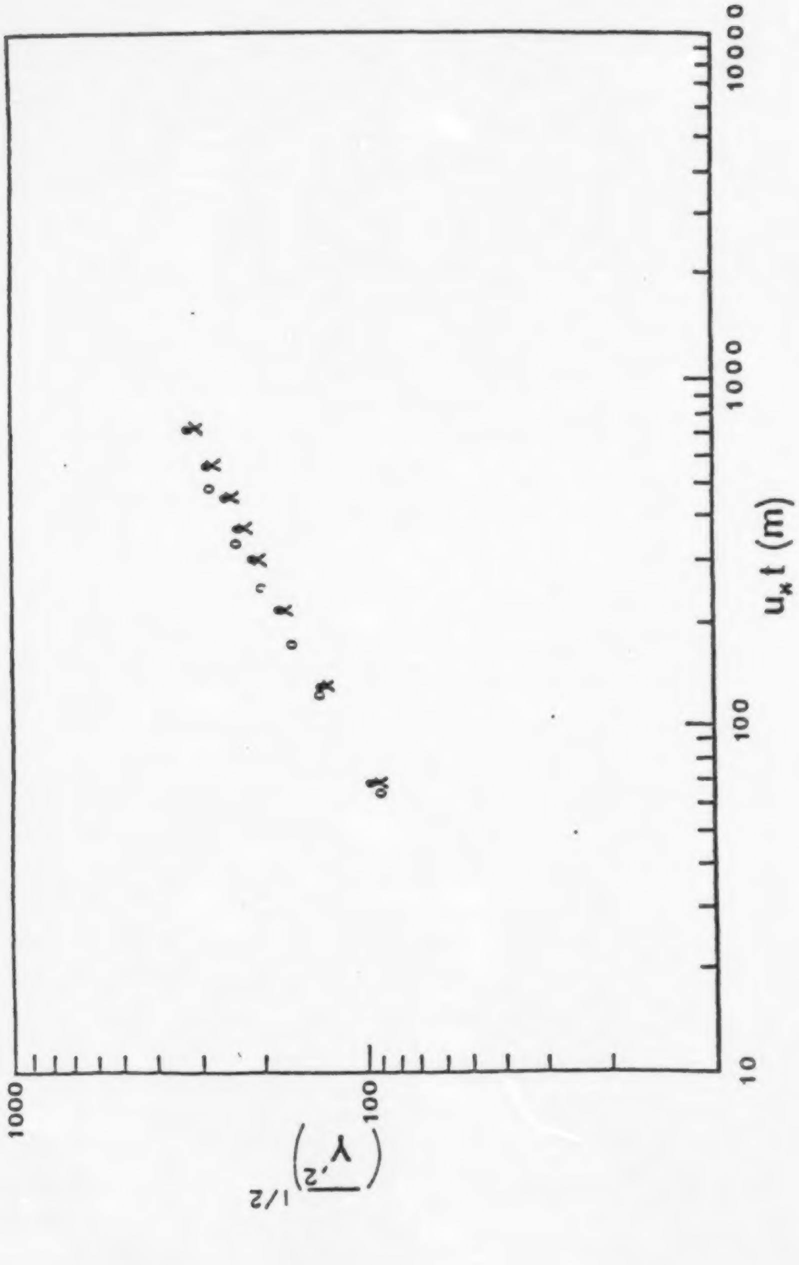

1000
100
$\left(\overline{Y'^2}\right)^{1/2}$
10
100
1000
10000
$u_* t$ (m)

Figure X-5 Along-the-wind (X) dispersion for the three cases described in the text. 0 - Flat boundary no wind. ● - Slope case no wind. X - Slope case with wind.

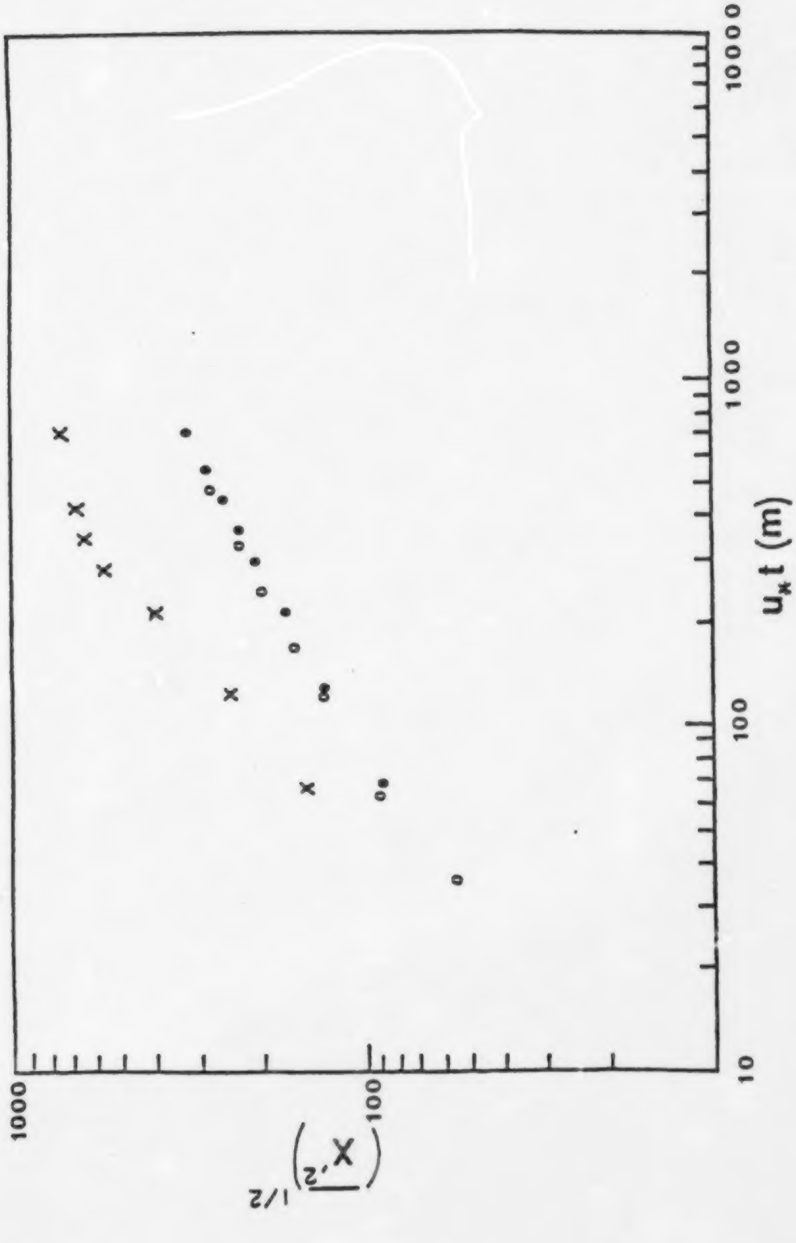
$\left(\overline{X'^2}\right)^{1/2}$
1000
100
10
100
1000
10000
$u_* t$ (m)

top of the slope flow (refer to Figure VI-7). As the puff grows vertically the particles encounter higher turbulent energy and thus the vertical growth is accelerated. For the slope case with wind, the enhanced vertical dispersion is primarily due to the fact that the puff is being transported by the mean wind into areas further down the slope where the turbulent boundary layer is deeper and turbulent energies more intense.

The horizontal dispersion curves indicate that u*t is an appropriate scale length in a stable boundary layer since for the no wind situation both the flat case and sloping case dispersion curves coincide. This is to be expected since $\sigma_u = \sigma_v$ are proportional to u*. The failure of the vertical dispersion curves to coincide, which is to say they are not a function of u* alone, points out that the surface stress is not a good indication of turbulent energy in the slope flows. This was also pointed out and explained in Chapter VI in that shear and destablization aloft in the slope flows produces local turbulence not connected with surface parameters.

Figure X-6 gives a more visual depiction of the particle spread through a time series snapshots of the actual particle puff over the sloping boundary for the case of no mean wind. Figure X-7 gives a similar time series of snapshots for the case with wind shear.

The examples presented in this chapter show the profound influence the slope and mountain flows have on transport direction. The increased turbulence fields and shear in the slope flows were also shown to greatly enhance the dispersion of particle puffs.

Figure X-6 Snapshots of particle spread over the sloping boundary with no wind. Each figure is 4 km in cross-section. Top figure gives dispersion 400 seconds after release; middle figure 800 seconds after release; bottom figure 2400 seconds after release.

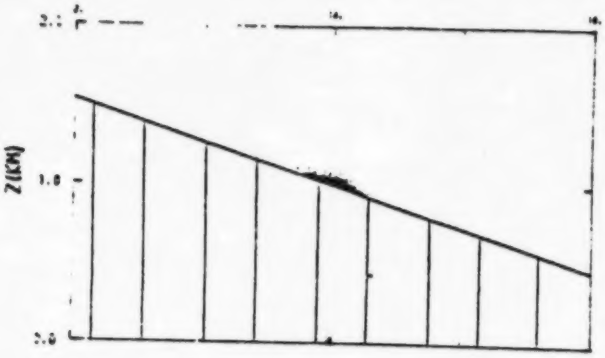

2.0
14.
16.
Z(KM)
1.0
0.0

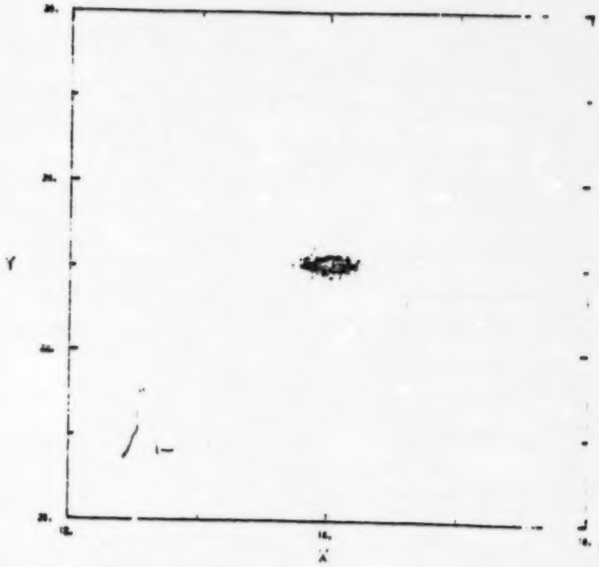

Y
12.
14.
16.
X

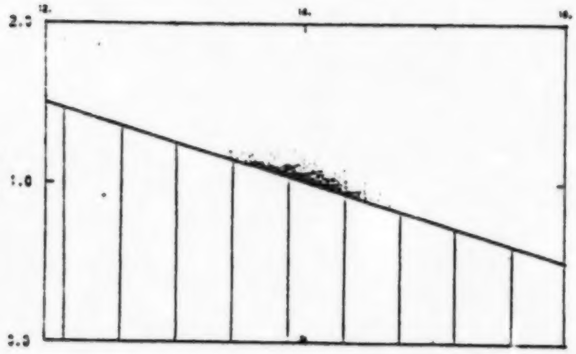

12.
14.
16.
2.0
Z(KM)
1.0
0.0

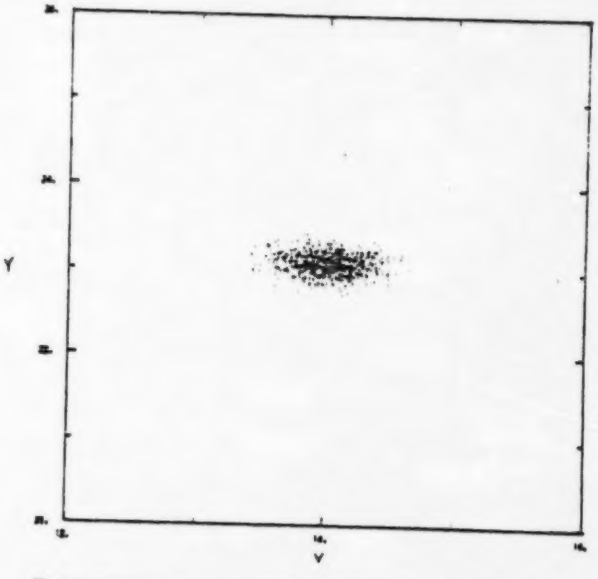

24.
Y
22.
12.
14.
16.
X

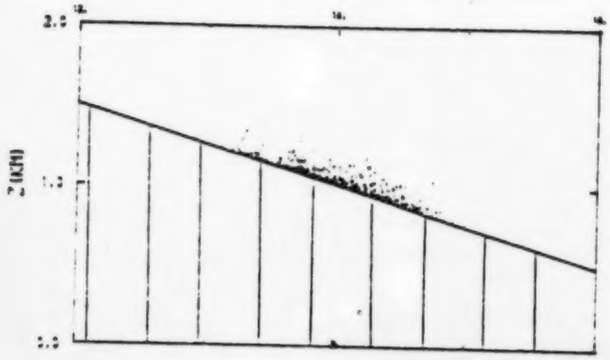

12.
14.
16.
2.0
Z(KM)
1.0
0.0

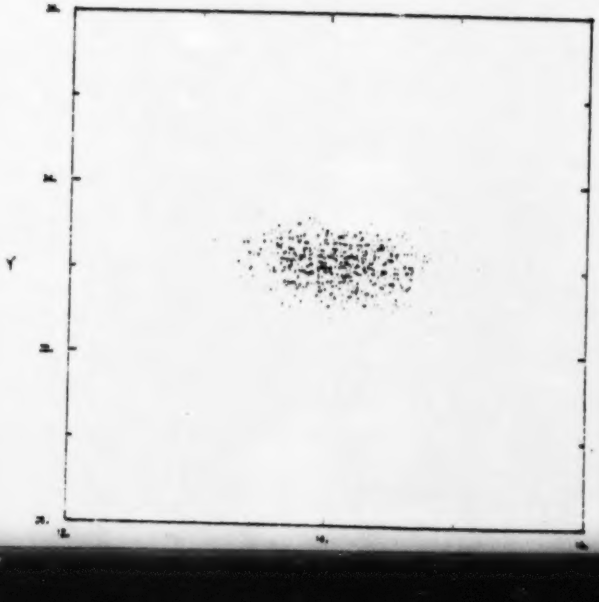

24.
Y
22.
12.
14.
16.

Figure X-7 Snapshots of particle spread over the sloping boundary with wind. Figure 8 km is cross-section. Top figure gives dispersion after 200 seconds; middle figure after 600 seconds; bottom figure after 1000 seconds.

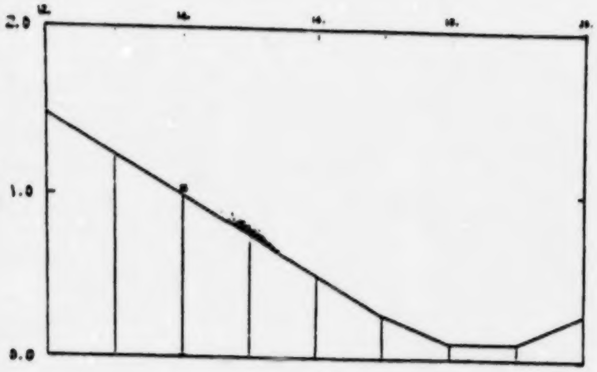
12.
14.
16.
18.
20.
2.0
1.0
0.0
Z(KM)

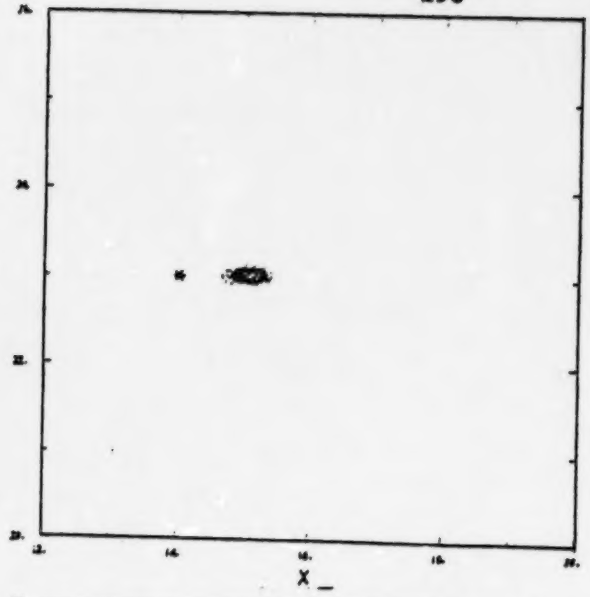
Y
X
12.
14.
16.
18.
20.

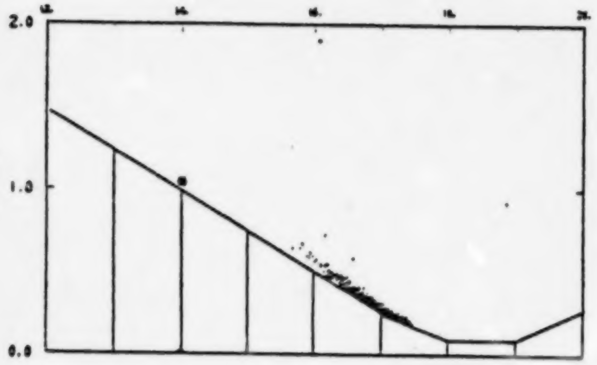
12.
14.
16.
18.
20.
2.0
1.0
0.0
Z(KM)

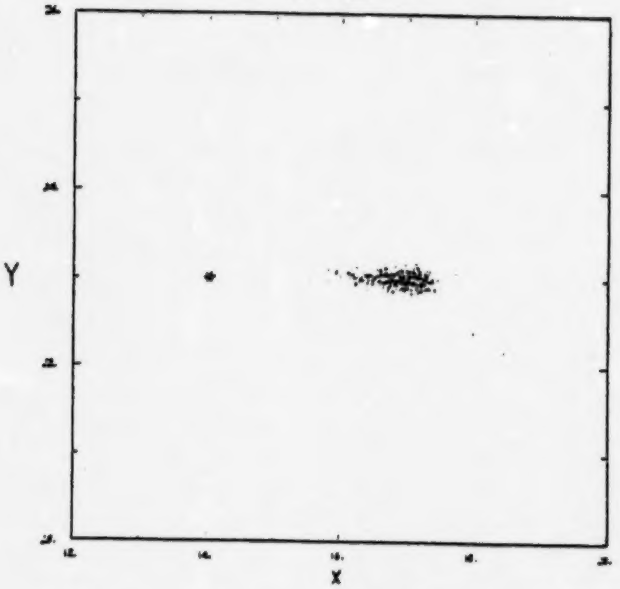
Y
X
12.
14.
16.
18.
20.

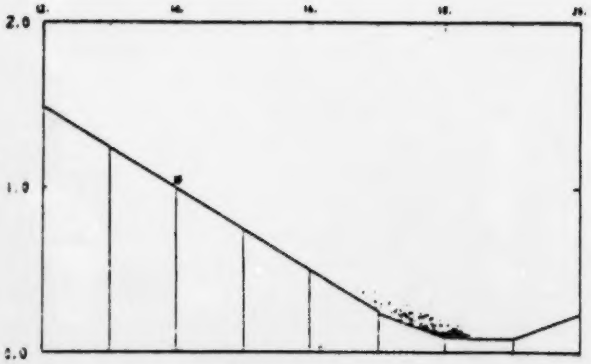
12.
14.
16.
18.
20.
2.0
1.0
0.0
Z(KM)

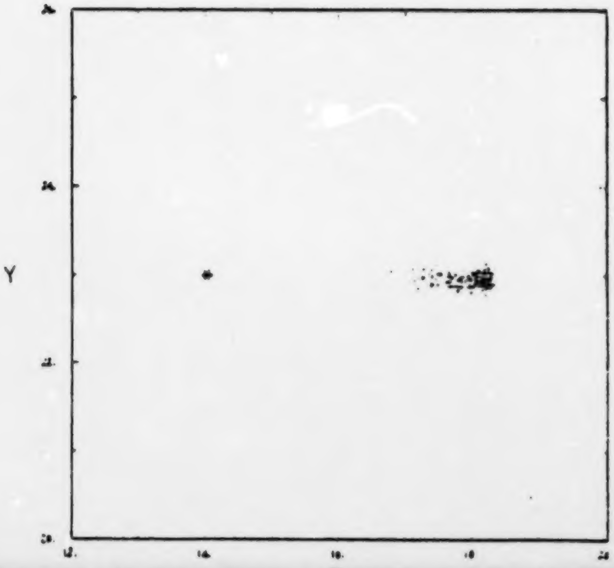
Y
X
12.
14.
16.
18.
20.

# XI. CONCLUSIONS

## Review and Conclusions

The major result in this study is that a numerical model can reproduce the essential features of the classic mountain-plain circulation including the deep mountain flow out of the valley. The success of the numerical experiment in producing the mountain flow could not have been readily expected since, unlike direct sea breeze circulations or slope flows, the mountain flow is a secondary circulation and a true three-dimensional feature. Part of the success in the simulations has to be attributed to the turbulent parameterization scheme incorporated into the model which avoids physically and numerically troublesome superadiabatic layers aloft as the cool air pools in the valley. Because the turbulence scheme is critical to the slope-mountain simulations and because boundary layer observations are not available over steeply sloping terrain, the scheme was tested against the Wangara and Great Plains data. The success of these tests lends credence to the applicability of the parameterization method to the slope-mountain simulations.

The second major result or conclusion of this study is that Lagrangian particle methods, coupled with the numerical mesoscale model, can directly examine pollutant transport in the complex flow field and provide a robust method for explicitly incorporating parameters characterizing the turbulent dispersion. The techniques described in this investigation allow these turbulence parameters to be computed directly from the mesoscale model so that they are consistent with the dynamic solution.

A number of other results were presented in the study. It was shown that joint consideration of sloping terrain and boundary layer processes produced low level jets in essential agreement with those over the Great Plains without resort to other mechanisms. Thus, this study provides support for the hypothesis that the Great Plains low level jets are due to topography. This is not to say that boundary layer processes and sloping terrain are the only mechanisms operating to produce the jets. Uccellini and Johnson (1979) offer an alternative explanation for the jets due to special synoptic conditions. It is perhaps during these special synoptic conditions that the low level jets are the strongest and most significant for severe weather.

The analytical solutions of the slope flows demonstrated clearly the role of stratification as a braking mechanism in the slope flows. The solutions also clarified the limited parameter space for oscillatory behavior in the slope flows and support the conclusion that surges observed in slope flows are not due to katabatic overshoot.

Examination of the dynamic mechanisms associated with the turbulent structure in the numerically simulated slope flows provided an hypothesis that convective instability due to differential temperature advection could produce high levels of turbulence near the top of the slope flows. This was quite unexpected and should be examined in observational studies.

Finally, detailed evaluation of the modeled cooling in the idealized valley of this study points to the conclusion that the cooling pattern through the entire depth of the valley as observed by Whitemand and McKee (1977) in deep valleys of the Rocky Mountains, is predominately an advective phenomenon.

Although the results of the study indicated the numerical model could qualitatively reproduce the slope and mountain flows, a detailed case study against actual data should be undertaken. Data bases from the ASCOT program and that of Whiteman and McKee (1977) now becoming available are likely candidates for case studies. Prior to the actual case studies, additional work needs to be done on the model to better pose the lateral boundary conditions. The present investigation essentially avoided the problem of non-homogeneous boundaries by employing zero gradient topography consistent with the zero gradient boundary conditions used in the model. This would not be an acceptable technique for application of the model to actual topography unless the boundaries are placed great distances from the area of interest and this procedure is computationally expensive. Nested model grids may be the only answer to the problem.

Preliminary results from the ASCOT program indicate that vegetation effects may also be important in the development of the slope flows. This may require parameterization in the model of both the form drag effect of trees and the radiative properties of trees.

Additional observational work needs to be undertaken to better characterize the slope and mountain flows. Specifically, turbulence measurements in the slope flows to determine turbulent intensity and length scales would be extremely useful to validate or improve the turbulent parameterization schemes utilized in models.

The Lagrangian particle model should be tested against tracer experiments in complex terrain. The recent field experiments conducted by the U.S. Environmental Protection Agency on an isolated hill may provide the data for specific validation of the techniques presented in this investigation.

# REFERENCES

Andre , J.C., G. DeMoor, P. Lacarrere, G. Therry and R. du Vachat, 1978: Modeling the 24-hour evolution of the mean and turbulent structures of the planetary boundary layer. J. Atmos. Sci., 35, 1862-1883.

Anthes, R.A., and T. Warner, 1978: Development of hydrodynamic models for air pollution and other mesometeorological studies, Mon. Wea. Rev., 105, 1045-1078.

Blackadar, A.K., 1957: Boundary layer wind maxima and their significance for the growth of nocturnal inversions. Bull. Amer. Met. Soc., 38, 283-290.

Blackadar, A.K., 1979: High resolution models of the planetary boundary layer. Advances in Environmental and Scientific Engineering, Vol. 1, Gordon and Breach. pp. 50-81.

Boas, M.L., 1966: Mathematical Methods in the Physical Sciences. John Wiley and Sons, New York.

Bonner, W.D., 1968: Climatology of the low level jet. Mon. Wea. Rev., 96, 833-850.

Bonner, W. D. and Jan Paegle, 1970: Diurnal variations in boundary layer winds over the south central United States in summer. Mon. Wea. Rev., 98, 735-744.

Briggs, G.A., 1979: Entrainment coefficient versus Ri for drainage flows and compatibility with turbulence scaling assumptions. Unpublished manuscript. NOAA, ATDL, Oakridge Tennessee.

Brost, R. A. and J.C. Wyngaard, 1978: A model study of the stably stratified planetary boundary layer. J. Atmos. Sci., 35, 1427-1440.

Businger, J.A., 1973: Turbulent transfer in the atmospheric surface layer. Workshop on Micrometeorology, Amer. Meteor. Soc., Chapter 2.

Caughey, S.J., J.C. Wyngaard, J.C. Kaimal, 1979: Turbulence in the evolving stable boundary layer. J. Atmos. Sci., 36, 1041-1052.

Chang, S.W., 1979: An efficient parameterization of convective and nonconvective planetary boundary layers for use in numerical models. J. Appl. Met., 18, 1205-1215.

Chiba, Osamu, 1978: Stability dependence of the vertical wind velocity skewness in the atmospheric surface layer. J. Meteor. Soc. of Japan, 56, 140-142.

Clark, R. H., A. J. Dyer, R. R. Brook, D. G. Reid and A. J. Troup, 1971: The Wangara experiment: Boundary layer data. Tech. Paper 19, Div. Meteor. Pys. (CSIRO, Australia).

Davidson, B. and P.K. Rao, 1963: Experimental studies of the valley-plain wind. Int. J. Air Wat. Pol., 7, 907-923.

Deardorff, J., 1974: Three-dimensional numerical study of the height and mean structure of the planetary boundary layer. Bound.-layer Meteor., 15, 1241-1251.

Defant, F., 1951: Local Winds in Compendium of Meteorology, Boston, Amer. Meteor. Soc., T. J. Malone ed. pp 655-675.

Delage, Y., 1974: A numerical study of the nocturnal atmospheric boundary layer. Quart. J. Roy, Meteor. Soc., V. 100, 351-364.

Dickerson, M.H., 1978: MASCON, A mass consistent atmospheric flux model for regions with complex terrain. J. Appl. Meteor., 17, 241-253.

Dickerson, M.H. and P. H. Gudiksen, 1980: The Department of Energy's Atmospheric Studies in Complex Terran. Second Joint Conference on Air Pollution Meteorology, New Orleans, LA. Amer. Meteor. Soc.

Fleagle, R.G., 1950: A theory of air drainage. J. of Meteor., 7, 227-232

Golder, D., 1972: Relations among stability parameters in the surface layer. Bound. Layer Meteor., 3, 47-58.

Hanna, S.R., 1968: A method of estimating vertical eddy transport in the planetary boundary layer using characteristics of the vertical velocity spectrum. J. Atmos. Sci., 25, 1026-1033.

Hanna, S.R., 1979: Some statistics of Lagrangian and Eulerian wind fluctuations, J. Appl. Meteor., 18, 518-531

Hoecker, W. H., 1963: Three southerly low level jet systems delineated by the Weather Bureau special pibal network. Mon. Wea. Rev., 91, 573-582.

Hoecker, W. H., 1965: Comparative physical behavior of southerly boundary layer wind jets. Mon. Wea. Rev., 91, 573-582.

Holton, J.R., 1967: The diurnal boundary layer wind oscillation above sloping terrain. Tellus, 19, 199-205.

Holzworth, G.C., 1980: The EPA program for dispersion model development for sources in complex terrain, Second Joint Conference on Applications of Air Pollution Meteorology, New Orleans, LA. Amer. Meteor. Soc.

Hosker, R.P. and K.S. Rao and G.A. Briggs, 1980: Experimental methods and preliminary analyses of drainage flow observations during the first ascot field study. Second Joint Conference on Applications of Air Pollution Meteorology, New Orleans, LA. Amer. Meteor. Soc.

Kaimal, J.C., J.C. Wyngaard, D.A. Haugen, O.R. Cote, Y. Izumi, S.J. Caughey, and C.J. Readings, 1976: Turbulence structure in the convective boundary layer. J. Atmos. Sci., 33, 2152-2168.

Kaimal, J.C. and Y. Izumi, 1965: Vertical velocity fluctuations in a nocturnal low-level jet. J. Appl. Met., 4, 576-584.

Keen, C.S., 1976: Trajectory Analyses of Mesoscale Air Pollution Transport in the Lake Michigan Shoreline Environment. Special Report No. 29 Center for Great Lake Studies University of Wisconsin - Milwaukee, Milwaukee, Wisconsin, 53201

Lamb, R.G., 1978: A numerical simulation of dispersion from an elevated point source in the convective boundary layer. Atmos. Environ., 12, 1297-1304.

Lettau, H. and B. Davidson, 1957: Exploring the Atmosphere's First Mile, Vols. 1 and 2. New York, Pergamon press 577 pp

Long, P.E. and D.W. Pepper, 1976: A comparison of six numerical schemes for calculating the advection of atmospheric pollution. Proc. Third Symposium on Atmospheric Turbulence, Diffusion and Air Quality. Amer. Meteor. Soc.

Lykosov, V.N. and L.N. Gutman, 1972: Turbulent boundary layer above a sloping underlying surface. Izv. Atmos. Oceanic Phys., 8, 462-467.

Manins, P.C. and B.L. Sawford, 1979a: A model for Katabatic winds. J. Atmos. Sci., 36, 619-630.

Manins, P.C. and B.L. Sawford, 1979b: Kalabatic winds: A field case study. Quart. J. Roy. Meteor. Soc., 105, 1011-1025.

Mahrer, Y. and R.A. Pielke, 1977: A numerical study of airflow over irregular terrain. Beitrage Zur Physik der Atmosphere, 50, 98-113.

Mahrer, Y. and R.A. Pielke, 1978: Test of an upstream spline interpolation technique for the advective terms in a numerical mesoscale model. Mon. Wea. Rev., 106, 818-830.

McCumber, M.C., 1980: A numerical simulation of the influence of heat and moisture fluxes upon mesoscale ciruclations, Ph.d Dissertation, Univeristy of Virginia, UVA - ENV SCI - MESO - 1980 - 2, p. 255

McNider, R.T. and R.A. Pielke, 1979: Application of the University of Virginia mesoscale model to air pollution transport. Proceedings of Fourth Symposium on Turbulence, Diffusion and Air Pollution. Amer. Met. Soc., Reno. Nev.

O'Brien, J.J., 1970: A note on the vertical structure of the eddy exchange coefficient in the planetary boundary layer. J. Atmos. Sci., 31, 1213-1215.

Paegle, J., 1978: A linearized analysis of diurnal boundary layer convergence over the topography of the U.S., Mon. Wea. Rev., 106, 492-502.

Paegle, J. and G. Rasch, 1973: Three dimensional characteristics of diurnally varying boundary-layer flows. Mon. Wea. Rev., 101, 746-756.

Paegle, J., W.G. Zdunkowski and R.M. Welch, 1976: Implicit differencing of predictive equations for the boundary layer. Mon. Wea. Rev., 104, 1321-1324.

Panofsky, H.A., A.K. Blackadar and G.E. McVehil, 1960: The diabatic wind profile. Quart. J. Roy. Meteor. Soc., v. 86, 390-398.

Panofsky, H.A., D.H. Lenschaw and J.C. Wyngaard, 1977: The characteristics of turbulent velocity components in the surface layer under convective conditions. Bound. Layer Meteor., 11, 355-361.

Pasquill, F., 1974: Atmospheric Diffusion, John Wiley and Sons.

Peterson, R.L., J.E. Cermak, and R.E. Nelson, 1980: Simulation of pollutant dispersion in the mountain wind. Second Joint Conference on Applications for Air Pollution Meteorology. Amer. Meteor. Soc., New Orleans, LA.

Petkovsek, Z. and A. Hocevar, 1971: Night Drainage Winds. Arch Met. Geoph. Boikl., 20, 353-360.

Pielke, R.A., 1974: A three-dimensional numerical model of the sea breezes over South Florida. Mon. Wea. Rev., 102, 115-139.

Pielke, R.A. and C.L. Martin, 1981: Consistent derivation of a terrain-following coordinate system for use in a hydrostatic model, submitted to J. Atmos. Sci.

Pielke, R.A. and Y. Mahrer, 1975: Representation of the heated planetary boundary layer in mesoscale models with coarse vertical resolution. J. Atmos. Sci., 32, 2288-2308.

Prandtl, L., 1942: Fuhrer durch die Stromungslehre, Vieweg & Sohn, Brunschweig, 373-375 (See Sutton (1953)).

Rao, K.S. and H.F. Snodgrass, 1979: Some parameterizations of the nocturnal boundary layer. Bound. Layer Meteor., 17, 15-28.

Rao, K.S. and H.F. Snodgrass, 1979: Modeling the nocturnal drainage flows. ASCOT Report No. 80/5.

Reid, J.D., 1979: Markov chain simulations of vertical dispersion in the neutral surface layer for surface and elevated releases. Boundary Layer Meteorology, 16, 3-22.

Sasamori, T., 1968: The radiative cooling calculation for application to general circulation experiments. J. Appl. Meteor., 7, 721-729.

Sasamori, T., 1972: A linear harmonic analysis of atmospheric motion with radiative dissipation. J. Meteor. Soc. Japan, 50, 505-518.

Sherman, C.A., 1978: A mass-consistent model for wind fields over complex terrain. J. Appl. Meteor., 17, 312-319.

Shir, C.C. and R.D. Bornstein, 1977: Eddy exchange coefficients in numerical model of the planetary boundary layer. Bound. Layer Meteor., 11, 171-185.

Shubert, J.F. and D. Pepper, 1976: Investigation of the bursting process in an atmospheric boundary layer using accustic methods. Third Symposium on Atmospheric Turbulence Diffusion and Air Quality. Amer. Meteor. Soc., Raleigh, N.C.

Smith, F.B., 1968: Conditioned particle motion in a homogeneous turbulent field. Atmos. Environment, 2, 491-508.

Sutton, O.G., 1953: Micrometeorology, McGraw-Hill, New York.

Teuscher, L.H. and L.E. Hauser, 1974: Development of Modeling Techniques for Photochemical Air Pollution, EPA-650/4-74-003, pp. 91.

Thyer, N.H., 1962: On valley and mountain winds, Ph.d Dissertation, University of Washington.

Thyer, N.H., 1966: A theoretical explanation of mountain and valley winds by a numerical method. Arch. Meteor. Geophys. Bioklim., 15, 318-348.

Tyson, P.D., 1966: Examples of local air circulations over Cato Ridge. S. African Geo. Jou., 48, pp 13-31.

Tyson, P.D., 1967: Velocity fluctuations in the mountain wind. J. Atmos. Sci., 25, pp 381-384.

Tyson, P.D. and R.A. Preston-Whyte, 1972: Observations of regional topographically induced wind systems in Natal. J. Appl. Meteor., 11, 643-650.

Uccellini, L.W. and D.R. Johnson, 1979: The coupling of upper and lower tropospheric jet streaks and implications for the development of severe convective storms. Mon. Wea. Review., 107, 682-703.

Wagner, A., 1938: Theorie and Beobactung der periodischen Gegirgswinde. GBH Band 52, p 408-449 (cited by Defant).

Wexler, H. 1961: A boundary layer interpretation of the low-level jet. Tellus, 13, 368-378.

Whiteman, C.D. and T.B. McKee, 1977: Observations of vertical atmospheric structure in a deep mountain valley. Arch. Met. Geoph. Biokl., 26, 39-50.

Willis, G.E. and J.W. Deardorff, 1978: A laboratory study of dispersion from an elevated source within a modeled convective boundary layer. Atmos. Environ., 12, 1305-1311.

Wipperman, F., 1973: Numerical study on the effects controlling the low level jet. Beitrage Zur Physik der Atmosphere, 46, pp 137-154.

Yamada, T. and G. Mellor, 1975: A simulation of the Wangara atmospheric boundary layer data. J. Atmos. Sci., 32, 2309-2329.

Yu, T., 1978: Determining the height of the nocturnal boundary layer, J. Appl. Met., 17, 28-33.

# Appendix A: Derivation of the Pressure Terms in the Model Equations

Using the Exner function,

$$\pi = c_p \left( \frac{p}{p_{oo}} \right)^{R/c_p} \qquad 1A)$$

the u-component equation of motion can be written as,

$$\frac{du}{dt} = - \theta \frac{\partial \pi}{\partial x} + fv \ . \qquad 2A)$$

We can then partition variables such that the total quantity A is defined by,

$$A = A_o + \hat{A}' + \tilde{A}' + A'$$

Where:

$A_o$ is a baseline value and A f (x,y)

$\hat{A}'$ is a synoptic scale perturbation

$\tilde{A}'$ is a mesoscale perturbation

$A'$ is a turbulent (or subgrid scale) perturbation

Using the total velocity u and the fact that

$$\frac{\partial A_o}{\partial x} = 0$$

we obtain

$$\frac{\partial u}{\partial t} = -u \frac{\partial u}{\partial x} - v \frac{\partial u}{\partial y} - w \frac{\partial u}{\partial z} + fv - (\theta_o + \hat{\theta}' + \tilde{\theta}') \frac{\partial \hat{\pi}'}{\partial x} \qquad 3A)$$

$$- (\theta_o + \hat{\theta}' + \tilde{\theta}') \frac{\partial \tilde{\pi}'}{\partial x} + \text{turbulent terms}$$

In the fourth term on the RHS assume that $\tilde{\theta}' \ll \theta_o + \hat{\theta}'$ and in the fifth term that $\hat{\theta}' \ll \theta_o + \tilde{\theta}'$ then,

$$\frac{\partial u}{\partial t} = fv - (\theta_o + \hat{\theta}') \frac{\partial \hat{\pi}'}{\partial x} - (\theta_o + \tilde{\theta}') \frac{\partial \tilde{\pi}'}{\partial x} + \text{other terms} \qquad 4A)$$

The first term on the RHS in 4A) is now totally a large scale term and the second term is totally a mesoscale term. The error in the assumptions leading to 4A) should be less than 5%.

We now make the assumption that the synoptic scale flow is in geostrophic balance so that the synoptic pressure gradient term can be represented by an equivalent velocity, i.e.

$$(\theta_o + \hat{\theta}')\frac{\partial\hat{\pi}'}{\partial x} = f\ Vg\ . \qquad 5A)$$

If we define $\tilde{\pi} = \pi_o + \tilde{\pi}'$ to be the total pressure minus the synoptic pertubation and use the fact that $\partial\pi_o/\partial x = 0$ then $\partial\tilde{\pi}/\partial x = \partial\tilde{\pi}'/\partial x$. Using this and the definition of geostrophic velocity in 4A) produces

$$\frac{\partial u}{\partial t} = fv - f\ Vg - (\theta_o + \tilde{\theta}')\frac{\partial\tilde{\pi}}{\partial x} + \text{other terms} \qquad 6A)$$

The corresponding Exner function for $\tilde{\pi}$ is then

$$\tilde{\pi} = c_p\left(\frac{Po + P'}{P_{oo}}\right)^{R/c_p} \qquad 7A)$$

remembering that $Po + \tilde{P}'$ is not the total pressure but is the total pressure minus the synoptic perturbation.

The consistent diagnostic equation for $\tilde{\pi}$ needed in 6A) is provided by the hydrostatic equation in the form

$$\frac{\partial\tilde{\pi}}{\partial z} = -\frac{g}{(\theta_o + \hat{\theta}')} \qquad 8A)$$

Note that the temperature utilized in this hydrostatic equation does not include the synoptic temperature perturbation since it has already been included in the large scale pressure gradient through Vg and is therefore not counted twice.

Defining $\tilde{\theta} = \theta_o + \tilde{\theta}'$ in 8A) and 6A) give the form of the u-component equation given in the text. The v-component equation is similarly derived.

# Appendix B: Computation Steps for Turbulent Dispersion in Chapter IX.

## Vertical Component Turbulent Statistics

1. For the unstable boundry layer compute the length scale $\lambda_m$ from IX-6 dependent on the vertical position of particle. For the stable case use $\lambda_m = z/(.55 + .8\ z/L)$ from the work of Kaimal (1972).
2. Determine A needed in IX-5 from Figure IX-1 as a function of stability.
3. For the unstable boundary compute $\sigma_w$ from IX-5 using A and $\lambda_{m,w}$. For the stable boundary layer compute $\sigma_w$ from IX-7.
4. Adjust $\sigma_w$ using IX-18.

## Horizontal Component Turbulent Statistics

5. Compute $\sigma_u$ and $\sigma_v$ from IX-8 or IX-9 for unstable and stable conditions, respectively.
6. Compute $\lambda_{m,u}$ and $\lambda_{m,v}$ from IX-10.

## Random Turbulent Fluctuation

7. Compute autocorrelation coefficient from IX-14.
8. Compute standard deviation for the random component from IX-2.
9. Determine skewness for the vertical component from IX-17.
10. Pick the random component from the skewed or normal distribution having distribution as found in Step 8.

## Turbulent Component

Compute turbulent component from IX-1 using the turbulent component from the previous time step and the random fluctuation computed above.